

Johanna Tranell

Seakeeping capabilities of sailing cruise and passenger vessels

Master's thesis in Marine Technology

Supervisor: Professor Sverre Steen

Co-supervisor: Jarle V. Kramer and Olav Rognebakke (DNV)

June 2021



Norwegian University of
Science and Technology

Johanna Tranell

Seakeeping capabilities of sailing cruise and passenger vessels

Master's thesis in Marine Technology
Supervisor: Professor Sverre Steen
Co-supervisor: Jarle V. Kramer and Olav Rognebakke (DNV)
June 2021

Norwegian University of Science and Technology
Faculty of Engineering
Department of Marine Technology



Kunnskap for en bedre verden



NTNU Trondheim
Norwegian University of Science and Technology
Department of Marine Technology

MASTER THESIS IN MARINE TECHNOLOGY

SPRING 2021

FOR

Elsa Johanna Margrethe Evensen Tranell

Seakeeping capabilities of sailing cruise and passenger vessels

Increasing environmental concerns among customers as well as tightening regulations by IMO and local authorities have resulted in a strong interest in development of zero- or low-emission cruise and passenger vessels. One of the most promising alternative propulsion technologies are then to use the wind. A number of different devices might be used – rigid or soft sails, Flettner rotors, kites, or wind turbines. The different devices have different benefits and drawbacks – and they influence the seakeeping of the ship in different ways. Also, the size of the wind propulsion device, measured in it's relative part of the required thrust, is presumed to be an important parameter, and it's influence on the seakeeping is therefore of interest.

The objective of the master thesis is to provide an understanding of how the sail systems influence the seakeeping capabilities of cruise and passenger vessels. The influence of the main types of sail systems shall be investigated through suitably selected case studies. The influence might for instance be quantified by the operability, where operability criteria are related to passenger comfort and sea sickness. Furthermore, practical methods for how the sail systems influence on seakeeping can be taken into account in practical work shall be described, and it is expected that at least one method shall be demonstrated through the case studies.

In the thesis the candidate shall present his personal contribution to the resolution of problem within the scope of the thesis work.

Theories and conclusions shall be based on mathematical derivations and/or logic reasoning identifying the various steps in the deduction.

The thesis work shall be based on the current state of knowledge in the field of study. The current state of knowledge shall be established through a thorough literature study, the results of this study shall be written into the thesis. The candidate should utilize the existing possibilities for obtaining relevant literature.

The thesis shall be organized in a rational manner to give a clear exposition of results, assessments, and conclusions. The text should be brief and to the point, with a clear language. Telegraphic language should be avoided.

The thesis shall contain the following elements: A text defining the scope, preface, list of contents, summary, main body of thesis, conclusions with recommendations for further work, list of symbols and acronyms, reference and (optional) appendices. All figures, tables and equations shall be numerated.



NTNU Trondheim
Norwegian University of Science and Technology
Department of Marine Technology

The supervisor may require that the candidate, in an early stage of the work, present a written plan for the completion of the work. The plan shall include a budget for the use of laboratory or other resources that will be charged to the department. Overruns shall be reported to the supervisor.

The original contribution of the candidate and material taken from other sources shall be clearly defined. Work from other sources shall be properly referenced using an acknowledged referencing system.

The thesis shall be submitted electronically (pdf) in Inpera:

- Signed by the candidate
- The text defining the scope (this text) (signed by the supervisor) included

Supervisor : Professor Sverre Steen
Advisors : Olav Rognebakke (DNV-GL), Jarle V. Kramer
Start : 15.01.2021
Deadline : 10.06.2021

Trondheim, 13.01.2021

Sverre Steen
Supervisor

Summary

In 2018, the International Maritime Organization announced a goal to reduce greenhouse gas emissions by at least 50% from 2008 to 2050. To achieve this objective, it is imperative that the industry adapts to greener propulsion systems. While most of the published research is related to the potential of fuel savings, this thesis aims to study the seakeeping capabilities of a wind assisted ship. By including the dynamic effects of ship motion on the sail system, the purpose is to provide an understanding of how a ship's seakeeping is affected by the introduction of sails.

This work includes two sail systems, the Flettner rotor and rigid wingsail. An aerodynamic sail damping model is created in Python, which assumes linear damping and two degrees of freedom. By including the roll and pitch rigid body motions, the dynamic wind conditions affecting the sails are captured. The Flettner rotor is modelled using empirical expressions from full scale measurements onboard a ship with a single Flettner rotor. The wingsail model assumes linear foil theory and uses a lifting line approach to calculate forces and resulting damping. Dynamic lift effects due to oscillatory motion are disregarded in this preliminary study. Although the aerodynamic model may overestimate or underestimate damping, depending on the degree of freedom, it is verified to provide reliable results across a selected range of true wind angles.

Assuming independent sail and vessel systems, the aerodynamic damping model is superposed with the hydrodynamic system of a ship hull, to obtain a wind assisted ship model. The ship model studied in this work is a 190 m long bulk carrier. Interaction effects between the hull and sail and between several sails are disregarded. Applying linear wave theory and strip theory, the vessel response with sails is calculated using ShipX Veres. The calculation tool assumes a symmetric flow, such that the ship drift angle is neglected. To limit the number of variables in the study, it is assumed that the the wind and incident waves are aligned, that the ship velocity is 12.5 kn, and the wind velocity is 10 m/s. Furthermore, the ship drift angle is assumed constant and equal to 5° in the aerodynamic damping model. The relevance of the sails in the context of propulsion is estimated using the ratio of sail thrust force to total ship resistance, including added resistance due to waves and ship drift.

The results of the wind assisted ship model with Flettner rotors indicates that a single degree of freedom model in roll would be sufficient. The hydrodynamic coefficients dominate in pitch, and the vessel pitch motion is small enough that the coupling term in roll can be neglected. Thus, the pitch motion effects of the sails are negligible, even though four Flettner rotors at a spin ratio of 4 are estimated to provide sufficient thrust for the ship to be entirely wind driven. Furthermore, it is thought that the linear damping model is a reasonable approximation within linear wave theory and ship motion. Best compatibility is observed in head wind or small apparent wind angles, where the damping is most pronounced. The linear damping model is invalidated if the wingsails stall, generating non-harmonic sail forces.

In general, sail damping is caused by variations in both wind velocity and wind angle. The dominant damping mechanism of each sail system is identified. As significant results were only observed in roll motion, it is concluded that exploitable wingsail damping is mainly caused by lift, although drag contributes in beam wind conditions. The exploitable Flettner rotor damping is mainly caused by drag, although lift contributes during close hauled sailing. Furthermore, the damping generation of wingsails is relatively insensitive to the angle of attack, while the Flettner rotor damping is highly dependent on the spin ratio. Although it is only investigated in the isolated aerodynamic sail system, there are indications that voluntary speed loss may be beneficial in certain conditions, to obtain higher aerodynamic damping.

Comparing the wind assisted vessel with the original mechanically propelled ship, the largest roll reduction is observed in close hauled sailing. However, significant roll reduction is observed in beam wind and waves, especially for the ship fitted with Flettner rotors. This suggests that the introduction of sails might remove the need for other roll reducing devices commonly used today. To further enhance the damping benefits, wingsails should be constructed with high-lift devices that delay stalling.

Due to the assumption of a small constant drift angle, the results of this work should not be applied to sailing conditions with large drift angles, without further investigation into the effects of drift angle on ship motions. Dynamic lift is thought to be of significance and should be included in future research. Finally, extending the analysis to consider interaction effects between the sails is of interest given the potential of damping enhancement by optimising the sail configuration. This requires more advanced and accurate calculation methods than the ones applied in this work.

Sammendrag

I 2018 annonserte FNs Sjøfartsorganisasjon et mål om å redusere utslipp av drivhusgasser med minst 50% fra 2008 til 2050. For å oppnå dette, er det avgjørende at industrien tar i bruk grønnere propulsjonssystemer. Mens det meste av dagens publiserte forskning er relatert til potensialet for å redusere drivstofforbruk, fokuserer denne avhandlingen på sjøegenskapene til et vindassistert skip. Målet er å gi en forståelse av hvordan sjøegenskapene til et skip påvirkes av seil, ved å inkludere dynamiske effekter fra skipsbevegelser på seilsystemet.

Dette arbeidet inkluderer to ulike seilsystemer, nemlig Flettner rotor og stivt vingeseil. En aerodynamisk seildempingsmodell er laget i Python ved å anta lineær demping og to frihetsgrader. De dynamiske vindforholdene som påvirker seilene fanges ved å inkludere skipets rull- og stampbevegelser i modellen. Flettner rotoren er modellert ved å benytte empiriske formler fra fullskala målinger ombord på et skip med én rotor. Vingeseilmodellen antar lineær foilteori og benytter en løftlinjetilnærming for å beregne krefter og resulterende demping. Dynamiske løfteffekter som følge av oscillerende bevegelse er sett bort fra i denne innledende studien. Selv om det er antydning at den aerodynamiske modellen kan over- eller underestimere dempingen, er den verifisert til å gi pålitelige resultater med hensyn på en varierende innfallsvinkel av sann vind.

Ved å anta uavhengige seil- og skipssystemer, kan den aerodynamiske dempingsmodellen superponeres med det hydrodynamiske systemet til et skipsskrog for å oppnå en vindassistert skipsmodell. Skipsmodellen som er brukt i dette arbeidet er et 190 m langt bulkskip. Interaksjonseffekter er sett bort fra, både mellom skip og seil, samt mellom flere seil. Beregningene av skipsbevegelsene med seil er utført ved hjelp av ShipX Veres, som antar lineær bølgeteori og stripeteori. Videre antar programmet et symmetrisk strømningsbilde, slik at skipets avdriftsvinkel er neglisjert. For å begrense antall variabler i studien antas det at vind- og bølgeretning er sammenfallende, skipets hastighet er 12,5 kn og vindhastigheten er 10 m/s. Videre er avdriftsvinkelen antatt konstant lik 5° i den aerodynamiske dempingsmodellen. Seilenes betydning i et propulsjonsperspektiv er estimert ved forholdet mellom seilenes fremdriftskraft og skipets totale motstand, inkludert tilleggsstanden som følge av bølger og avdriftsvinkel.

Resultatet av den vindassisterte skipsmodellen med Flettner rotor er indikerer at å inkludere kun én frihetsgrad ville vært tilstrekkelig. De hydrodynamiske koeffisientene dominerer i stamp og skipets stampebevegelse er tilstrekkelig liten til at koblingsleddet i rull kan neglisjeres. Stampeffektene fra seilene er derfor neglisjerbare, selv om fire Flettner rotor er med et rotasjonsforhold (eng: spin ratio) på 4 estimeres til å gi nok fremdrift til at skipet er fullstendig vinddrevet. Videre er det anslått at den lineære dempingsmodellen er en rimelig antakelse i lineær bølgeteori og skipsbevegelse. Best kompatibilitet er observert i motvind eller med kurs høyt mot vinden, hvor seildempingen er mest fremtredende. Den lineære dempingsmodellen er ikke aktuell dersom vingeseilene steiler, slik at seilkraften er ikke-harmonisk.

Generelt sett skapes seildempingen av variasjoner i både vindhastighet og innfallsvinkel. Den dominerende dempingsmekanismen for hvert seilsystem er identifisert. Ettersom betydelige resultater kun ble observert i rull, kan en konkludere med at den utnyttbare vingeseildempingen hovedsakelig kommer av løft, selv om drag bidrar i sidevind. Den utnyttbare Flettner rotor dempingen skapes hovedsakelig av drag, selv om løft bidrar når skipet seiler med kurs høyt mot vinden. Videre er vingeseildemping relativt lite sensitiv mot angrepsvinkelen, mens dempingen fra en Flettner rotor er høyst avhengig av rotasjonsforholdet. Resultatene viser indikasjoner på at såkalt frivillig fartstap kan være fordelaktig i visse situasjoner for å øke dempingen. Dette er dog bare undersøkt i det isolerte aerodynamiske seilsystemet.

Ved å sammenligne det vindassisterte skipet med det originalt kun mekanisk drevne skipet er den største rullreduksjonen observert ved vind med små innfallsvinkler. Signifikant rullreduksjon er likevel observert i sidevind og sidebølger, spesielt for skipet med Flettner rotor. Dette antyder at behovet for andre klassiske rullreducerende innretninger kan elimineres dersom skipet utstyres med seil. For å øke dempingsfordelene bør vingeseil konstrueres med løftpromoterende innretninger som forsinker steiling.

På grunn av antakelsen om en konstant og liten avdriftsvinkel, bør resultatene av dette arbeidet ikke overføres til situasjoner med en stor avdriftsvinkel uten først å undersøke vinkelens effekt på skipsbevegelser. Dynamisk løft er anslått å være av betydning og bør inkluderes i fremtidige studier. Avslutningsvis er det av interesse å utvide analysen til å inkludere interaksjonseffekter mellom seil, for å studere potensialet for å øke dempingen ved å optimalisere seilkonfigurasjonen. Dette krever imidlertid mer avanserte og nøyaktige beregningsmetoder enn hva som er benyttet i dette arbeidet.

Preface

This thesis completes my Master of Science in Marine Technology with a specialisation in Marine Hydrodynamics. The work is carried out during the spring semester of 2021, at the Norwegian University of Science and Technology (NTNU) in Trondheim.

Firstly, I would like to thank my supervisor Professor Sverre Steen at the Department of of Marine Technology (IMT). I have truly enjoyed working with you, and I am grateful for the continuous support whenever I asked for it. During this final year, I have gained a profounder knowledge within marine hydrodynamics thanks to your guidance, while simultaneously pushing me to become an independent engineer.

I am also thankful for the continuous help from my advisor Jarle Kramer. Your patience and ability to always make time for my theoretical questions is greatly appreciated. I look forward to reading your PhD thesis in the future. Please send it to me when you complete it.

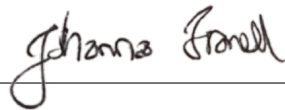
Furthermore, I greatly appreciate the help of Senior Research Scientist Jan Roger Hoff at SINTEF Ocean, who extended the programme NewMotions so that I could use it in my work. I did not expect the support and patience, but it is safe to say I would not have been able to get the calculations running without your help. I am happy to have discovered and experienced this support from several experts in the field of marine technology. Senior Project Manager Rogier Eggers at MARIN contributed to that by showing interest in my thesis and giving me valuable input in the initial state of the work.

Last but not least; my friends.

Thank you Nora, for spending a day proofreading this thesis, and for reaching out to me and including me into the group when I was new to Tyholt.

Thank you Karina, my dear friend in Perth, not only for reading almost every chapter of this thesis helping me improve the English, but also for always sending me greetings from my beloved Perth. Mate, I cannot wait until covid is history and I am allowed back!

And finally, my NTNU adventure started in a different department than IMT. Even though my brain belongs to marine hydrodynamics, my heart is with the amazing group of people from Berg. My dear friends from Geotechnology and Petroleum Engineering, thank you for making this time unforgettable. We had quite some years, and thankfully, the fun only continues from here!



Johanna Tranell
Trondheim, 10.06.2021

Nomenclature

Abbreviations

AoA	Angle of attack
AR	Aspect ratio
AWA	Apparent wind angle, measured from the flow-fixed X-axis
awa	Local apparent wind angle
AWS	Apparent wind speed
aws	Local apparent wind speed
CFD	Computational fluid dynamics
DoF	Degree of freedom
IMO	International Maritime Organization
JONSWAP	Joint North Sea Wave Project
PM	Pierson-Moskowitz
RAO	Response amplitude operator
SOBC-1	SINTEF Ocean Bulk Carrier 1
SR	Spin ratio
TWA	True wind angle
TWS	True wind speed
WA	Wind assistance
WAPS	Wind assisted propulsion systems

Symbols

α	Angle of attack
β	Drift angle
β_w	Wave heading, relative to the ship-fixed x-axis
$\delta\alpha$	Variation in angle of attack due to unsteady wind angle
ΔC_F	Hull roughness resistance coefficient
δ	Trim angle of wingsail, relative to the flow-fixed X-axis
δ_k	Phase angle of the response in mode k
ϵ_j	Random phase angle of irregular wave component j
η_1, η_2, η_3	Translatory displacements in surge, sway and heave, respectively

Nomenclature

η_4, η_5, η_6	Rotational displacements in roll, pitch and yaw, respectively
η_s	Significant response amplitude
γ	Peak shape parameter in the JONSWAP spectrum
ν	Viscosity of water
Ω	Angular velocity of the Flettner rotor
ω_0	Incident wave frequency
ω_e	Encounter frequency
ω_p	Peak angular frequency
Φ	Factor in SINTEF Ocean's formula of the hull form factor
ρ_w, ρ_a	Density of water and air, respectively
σ^2, σ_r^2	Variance of the wave spectrum and response spectrum, respectively
AWA_S, AWA_U	Steady and unsteady apparent wind angle, respectively
ζ_a	Wave amplitude of regular wave
A_j	Wave amplitude of irregular wave component j
A_p	Transverse projected area
A_R	Rudder area
b_{jk}	Damping derivative in mode j due to a forced motion in mode k
C_A	Correlation resistance coefficient
C_B	Block coefficient
C_D	Drag coefficient
C_F	Frictional resistance coefficient
C_L	Lift coefficient
C_R	Residual coefficient
C_V	Viscous resistance coefficient
C_W	Wave resistance coefficient
C_{APP}	Appendage resistance coefficient
$C_{T,CW}$	Total calm water resistance coefficient
C_{AA}	Air resistance coefficient
C_{BD}	(Base drag) Transom stern resistance coefficient
$C_{D\nu}$	Viscous drag coefficient in linear foil theory
$C_{Di,1}$	Linear component of drag coefficient
$C_{Di,2}$	Non-linear component of drag coefficient from cross-flow drag
C_{Di}	Induced drag coefficient in linear foil theory
$C_{L,1}$	Linear component of lift coefficient from low aspect ratio wing theory
$C_{L,2}$	Non-linear component of lift coefficient from cross-flow drag
d_e	Diameter of Flettner rotor end disk
$H(\omega, \beta_w)$	Transfer function of the rigid body motion
H_S	Significant wave height

k_j	Wave number of irregular wave component j
k_s	Average height of roughness in SINTEF Ocean's formula of ΔC_F
L_{OS}	Length over surface
L_{PP}	Length between perpendiculars
L_{WL}	Length on waterline
$m_n, m_{\eta,n}$	n 'th moment of the wave spectrum and response spectrum, respectively
P_{rotor}	Input power to the Flettner rotor
R_{AD}	Added resistance due to drift
R_{AW}	Added resistance in waves
R_{CW}	Calm water resistance
$S(\omega)$	Wave spectrum
s_1, s_2	Motion of a point on a rigid body in surge and sway, respectively
S_B	Wetted surface area of the transom stern
T_p	Peak period
V_A	Apparent wind velocity
V_P	Relative horizontal wind velocity due to ship pitch velocity
V_R	Relative horizontal wind velocity due to ship roll velocity
V_S	Ship velocity
V_T	True wind velocity
$V_{air,r}$	Relative wind velocity in ship resistance due to air and wind
$V_{A,S}, V_{A,U}$	Steady and unsteady apparent wind velocity, respectively
V_{wS}	Relative wind velocity due to ship velocity
AWA^*	Apparent wind angle, measured from the ship-fixed x-axis
B	Breadth moulded
c	Chord length of wingsail
$C(k)$	The Theodorsen function
D	Drag force
d	Diameter
f	Ship freeboard
$F(k)$	Real part of the Theodorsen function
g	Gravitational acceleration
H	Height of sail
h	Height of a section in the discretised sail
k	Hull form factor (in ship hydrodynamics) or reduced frequency (in foil theory)
k'	Cross-flow drag coefficient
L	Lift force
S	Hull wetted surface area
T	Draught

Contents

Summary	iii
Sammendrag	v
Preface	vii
Nomenclature	ix
1 Introduction	1
1.1 Background and motivation	1
1.2 Previous work	2
1.2.1 Seakeeping literature	2
1.2.2 Power performance literature	7
1.3 Objectives	8
1.4 Structure of the thesis	9
2 Ship hydrodynamics	11
2.1 Short-term statistical description of waves	11
2.2 Linear wave induced ship motion	13
2.2.1 Response in regular waves	13
2.2.2 Short term statistics of the response	14
2.3 Hull resistance	15
2.3.1 Calm water resistance	15
2.3.2 Added resistance in waves	18
2.3.3 Increased resistance due to drift	19
3 Aerodynamics and modelling of sail systems	23
3.1 Flettner rotor	24
3.1.1 Viscous effects and three-dimensional flow	25
3.1.2 Experimental data	25
3.2 Rigid wingsail	26
3.2.1 Linear foil theory	27
3.2.2 Viscous effects and three-dimensional flow	27
3.2.3 Unsteady lift	28
3.3 Interaction effects between multiple sails	30
4 The aerodynamic sail model	31
4.1 Coordinate system definitions	31

4.2	Assumptions and governing equations	32
4.3	Wind model	35
4.4	Flettner rotor model	37
4.5	Wingsail model	39
4.5.1	Sail trim and local angle of attack	40
4.6	Code algorithm	42
4.7	Convergence of sail discretisation	43
5	Sail model verification	45
5.1	Sail force generation	45
5.2	Damping derivatives	47
6	The wind assisted ship model	50
6.1	Assumptions of the model	50
6.1.1	Representative ship and sea states	51
6.2	Calculation tool: ShipX	52
6.2.1	Compatibility of coordinate systems	53
6.3	Quasi-steady sailing model	54
6.4	Wind assistance fraction	56
7	Results	58
7.1	Dominant damping mechanism	59
7.1.1	Flettner rotor	60
7.1.2	Wingsail	62
7.2	Thrust and damping conflict	65
7.2.1	Flettner rotor	65
7.2.2	Wingsail	66
7.3	Roll and pitch amplitude reduction	68
7.3.1	Flettner rotor	72
7.3.2	Wingsail	74
7.3.3	Wingsail of higher AR	75
7.4	One versus two degrees of freedom model	76
7.5	Percentage of wind assistance	77
8	Discussion	79
8.1	Validity of major simplifications	82
9	Conclusions	83
9.1	Recommendations for future work	84
	Bibliography	85
	Appendices	88
A	Python code	89
B	ShipX reports of SOBC-1	99
B.1	Hydrostatics report	99
B.2	Ship resistance coefficients report	100
C	Flettner rotor induced roll and pitch moments	101
D	Wingsail induced roll and pitch moments	105

List of Figures

- 1.1 Roll induced velocity and force changes on a wingsail (Satchwell, 1986). 3
- 1.2 Roll reduction due to lift effects from a marine aerofoil (Satchwell, 1986). 4
- 1.3 Comparison of roll damping coefficients for different wind propulsion devices (Sinclair, 1994). 6

- 2.1 The JONSWAP spectrum for $H_S = 4.0$ m, $T_p = 8.0$ s and different values of γ (DNVGL-CG-0130, 2018). 12
- 2.2 Coordinate system definition with rigid body motion modes (Faltinsen, 1993). . . 13
- 2.3 Typical wavelength dependency of added resistance of a ship in waves (Faltinsen, 1993). 18
- 2.4 The coordinate system of Yasukawa and Yoshimura (2015). 20

- 3.1 Idea sketch of the sail systems (Clayton, 1987) 23
- 3.2 The Buckau photographed in 1924. 24
- 3.3 The Magnus effect (Marchaj, 2000). 25
- 3.4 The Oceanbird concept (Wallenius Marine, 2020). 26
- 3.5 Potential flow around a foil (Newman, 2018) 27
- 3.6 2D lift and drag coefficients of NACA 0012 foil. 29
- 3.7 Lift and circulation development in time due to a sudden change in angle of attack (Marchaj, 2000). 29
- 3.8 The Theodorsen function, Equation (3.18). The figure is from Bishop et al. (1972) in Newman (2018). 30

- 4.1 Defined coordinate systems. 31
- 4.2 The steady and dynamic wind velocity triangles. 35
- 4.3 Definition of positive SR and lift force in the Flettner rotor model. The blue area marks the area of positive lift, i.e. towards the positive X-direction 37
- 4.4 Empirical lift, drag and power coefficients of Tillig (2020) and their modifications used in the Flettner rotor model. 38
- 4.5 Variation of angle of attack in roll mode 41
- 4.6 Wingsail trim for positive values of AWA 41
- 4.7 Wingsail trim in the two cases of negative AWA. 42
- 4.8 Sail discretisation convergence check, Flettner rotor. 44

- 5.1 Comparison of calculated thrust coefficient with external reference (Kramer et al., 2016a) 46
- 5.2 Comparison of induced damping derivatives 49

- 6.1 The global coordinate system and sign convention used in Veres. 54

7.1	Aerodynamic roll and pitch moments from Flettner rotor, case 3: TWA = 110° . .	61
7.2	Change of Flettner rotor lift force during an oscillation.	61
7.3	Aerodynamic roll and pitch moments from wingsail, case 4: TWA = 130°	63
7.4	Aerodynamic roll and pitch moments from wingsail, stall and trim effects.	64
7.5	Flettner rotor damping and thrust as functions of spin ratio.	66
7.6	Wingsail damping and thrust as functions of angle of attack. Stall not included. .	67
7.7	Wingsail damping and thrust as functions of angle of attack. Stall included. . . .	68
7.8	RAO in roll of the original hull without sails.	69
7.9	Roll RAO at resonance in each sea state.	72
7.10	Significant roll amplitudes from iteration 0	72
7.11	Roll amplitude reduction at resonance, for the ship fitted with Flettner rotor. . .	73
7.12	Roll amplitude reduction at resonance, for the ship fitted with wingsail.	74
7.13	Roll reduction of a Flettner and wingsail of equal AR. The limitation on TWA and β_w with respect to model validity is posed by the AR 6 wingsail.	75
7.14	Roll RAO at resonance computed by 1 DoF model (roll) and 2 DoF model (roll and pitch).	76
C.1	Flettner rotor damping mechanism evaluation: induced aerodynamic moments . .	101
D.1	Wingsail damping mechanism evaluation: induced aerodynamic moments	105

List of Tables

5.1	3D lift coefficient [-] and lift force per unit projected sail area [N/m ²].	46
6.1	Principal hull data of the SOBC-1.	51
6.2	Sample sea states.	52
7.1	Standard case data.	58
7.2	Wind angle cases in evaluation of damping mechanism.	59
7.3	Dominating damping mechanisms of a Flettner rotor.	60
7.4	Dominating damping mechanisms of a wingsail.	62
7.5	Case summary, including required iterations (iter) for converged solutions.	71
7.6	WA [%] of ship with Flettner rotors. Sea state 1.	77
7.7	WA [%] of ship with Flettner rotors. Sea state 2.	77
7.8	WA [%] of ship with Flettner rotors. Sea state 3.	77
7.9	WA [%] of ship with wingsails. Sea state 1.	78
7.10	WA [%] of ship with wingsails. Sea state 2.	78
7.11	WA [%] of ship with wingsails. Sea state 3.	78



Chapter 1

Introduction

1.1 Background and motivation

Utilising the wind for propulsion is an ancient technology and until the nineteenth century, seaborne trade was mostly the domain of large sailing ships. With the industrial revolution, the opening of the Suez Canal and the introduction of the diesel engine in the late nineteenth to the early twentieth century came the dominance of mechanically driven ships (Bordogna, 2020). However, throughout the years, the interest in wind assisted propulsion has continued, linked to the price of marine fuel. The modern implementation of wind assistance arose in the oil price shock of the 1970s. In the early 80s, the Japanese ships *Shin Aitoku Maru* and *Usuki Pioneer* demonstrated the potential of wind assistance using wingsails (Satchwell, 1986). Other sail technologies were also explored, but interest fell as oil prices decreased in the 80s.

With growing environmental concern, wind assisted propulsion is once again a technology gaining a lot of focus and attention. Technological development is motivated by strategies like the 2018 goal of the International Maritime Organization (IMO) (IMO, 2018), which aims to reduce greenhouse gas emissions by at least 50% by 2050 compared to the levels of 2008, while simultaneously pursuing efforts to phase them out entirely during this century. Given that the world fleet continues to grow, it is imperative to introduce alternative propulsion systems that decrease or entirely prevent emissions. In 2020, the fourth IMO greenhouse gas study (Faber et al., 2020) concluded that greenhouse gas emissions from global shipping are expected to increase by up to 50% between 2018 and 2050. This equals up to 130% of the 2008 level.

Several sail technologies exist and are being further developed and used today. These include conventional soft sails, soft or rigid wingsails, Flettner rotors, kites and turbosails. All of these technologies are commercially available today and offer solutions for wind assistance. Furthermore, the Dutch company Dykstra Naval Architects have contributed to the revival of the DynaRig for use on cargo ships through the proposed WASP Ecoliner (Dykstra Naval Architects, 2020). Other ongoing projects aim to create zero-emission ships, perhaps the most recent and noteworthy being the Swedish project wind Powered Car Carrier (wPCC), a collaboration between Wallenius Marine, KTH and SSPA (Wallenius Marine, 2020).

With the world's current focus on decarbonisation, most of the published research about wind assisted propulsion systems (WAPS) is related to assessing the performance in terms of power and fuel savings. While these considerations are important for evaluating the benefits and possibilities

of WAPS, there seems to have been little focus so far on how the seakeeping of a ship is affected by introducing WAPS. It is of great technical and commercial interest in the context of low- and zero-emission ships to study the seakeeping performance of wind assisted ships in greater detail. The comfort of crew and passengers is an important factor. Predicting or establishing the degree of roll reduction could lead to the elimination of other roll reduction devices that consume cargo space. Improvements in ship motion might also reduce ship resistance, indirectly leading to improved propulsive effects, such that the sails contribute propulsion benefits beyond the direct aerodynamic thrust force.

To summarise, it is necessary to quantify the relative importance of the thrust and damping characteristics of a given sail system. In this investigation of the sail devices' influence on the seakeeping capabilities, two factors are assumed to be important. These are the specific sail device and the size of it, measured in its relative part of the required thrust.

1.2 Previous work

As previously mentioned, much of the published work of WAPS today focuses on the performance in terms of power and fuel savings. A much wider research base and effort can be found for sailing yachts, perhaps motivated by the attention, competitive drive and money involved in yacht races like the America's Cup. Given the scope of this thesis, this literature review centres on works related to wave induced dynamic effects for wind assisted ships, but a shorter review of the performance literature is also included.

Thus, the following literature review is divided into two parts. The first one is related to the seakeeping, and the second is related the performance prediction of ships with WAPS. The division is based on the difference that the former includes the effect of ship motion on the sails, while the latter does not.

1.2.1 Seakeeping literature

To this author's knowledge, the motion damping benefits of sail devices have not been explored since some initial work was published in the 1980s and 90s, like the preliminary investigation of Satchwell (1986) and later, more detailed work of Sinclair (1991) and several associated papers. At that time, operational experience of the Japanese wind assisted ships *Shin Aitoku Maru* and *Usuki Pioneer* had been published, showing fuel savings and unforeseen propulsive advantages from motion damping effects. This led to the idea that wingsails (Satchwell (1986) called them marine aerofoils) in the future could be thought of as roll dampers instead of propulsive devices and that installing such foils could be motivated by a range of benefits, not solely fuel savings.

In the preliminary work of Satchwell (1986), the following assumptions were made. The ship was subject to sinusoidal beam waves of small amplitude, the wingsail was free of stall and only the effects of lift on the ship motion were included in the model. The wind and foil chord length were assumed invariant of height. Firstly, in the assessment of roll damping mechanisms, the effect of roll motion on the roll damping coefficient was divided into two components. The roll induced velocity, $\dot{\eta}_{AZ}$, caused a change in both apparent wind incidence δAWA^* and apparent wind speed δV_A , see Figure 1.1. Here, AWA^* denotes the apparent wind angle measured from the ship centreline. Furthermore, Satchwell (1986) derived simplified expressions of the two corresponding roll damping coefficient components due to lift, δL , only. These indicated that the damping due to incidence change will follow the sign and magnitude of the lift force. It will be positive for unstalled aerofoils, negative for stalled foils and zero for foils without a fixed

Kutta point, such as Flettner rotors. The damping component from the roll induced air velocity change was proportional to $C_L(z) \sin(\text{AWA}^*) \cos(\text{AWA}^*)$. This indicated a conflict between damping and wind propulsion for apparent wind angles above 90° . If damping is to be achieved ($\cos(\text{AWA}^*) < 0$ and $C_L(z) < 0$), it would be at the expense of wind propulsion.

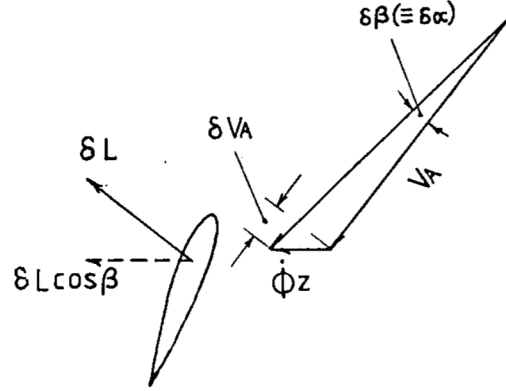


Figure 1.1: Roll induced velocity and force changes on a wingsail (Satchwell, 1986). Two symbols deviate from the notation of this thesis. β is AWA^* , ϕ is roll angular displacement η_4 .

Secondly, Satchwell (1986) assessed the aerodynamic loads using lifting line theory. The simplified approach was justified by the fact that a number of other uncertainties existed, like the nature of the hull superstructure vortex shedding, atmospheric turbulence and sea surface effects, making a more refined technique of limited merit.

Thirdly, the roll reduction due to a wingsail was estimated as a fractional value. This was done by using the concept of hydrodynamic linearised equivalent damping coefficient, ν_{η_4} , in a linear roll equation of motion. The maximum roll amplitude of a ship without aerofoils, $\eta_{4a,\max}$, was proportional to the wave slope and $1/\nu_{\eta_4}$. Similarly, the maximum roll amplitude of a ship with wingsails was noted to be inversely proportional to the sum of the hydrodynamic and aerodynamic ($\nu_{\eta_4}^A$) linearised equivalent damping coefficients, Equation (1.1). The fractional reduction in resonant roll amplitude could then be quantified according to Equation (1.2).

$$\eta_{4a,\max}^A = \frac{1}{\nu_{\eta_4} + \nu_{\eta_4}^A} \quad (1.1)$$

$$\frac{\eta_{4a,\max} - \eta_{4a,\max}^A}{\eta_{4a,\max}} = \frac{\nu_{\eta_4}^A}{\nu_{\eta_4} + \nu_{\eta_4}^A} \quad (1.2)$$

Satchwell (1986) presented results of roll reduction using representative inputs for a sample vessel. Figure 1.2a shows the roll reduction when the lift coefficient is chosen to maximise the wind propulsion, while Figure 1.2b is based on a lift coefficient to maximise roll damping. One sees a high negative damping for strong beam winds when the lift is maximised for propulsion. While the two results show differences, the overall trend of good damping for true wind angles less than 90° and problems for angles above 90° is observed in both. The shift was explained by the fact that with beam apparent wind, the damping is zero due to the lift having no lateral component.

To summarise the work of Satchwell (1986), it introduced the question of aerofoil incidence control, which governs the lift coefficient and therefore also the roll damping. A suggested compromising objective was to maximise propulsion, but progressively reduce it in strong beam

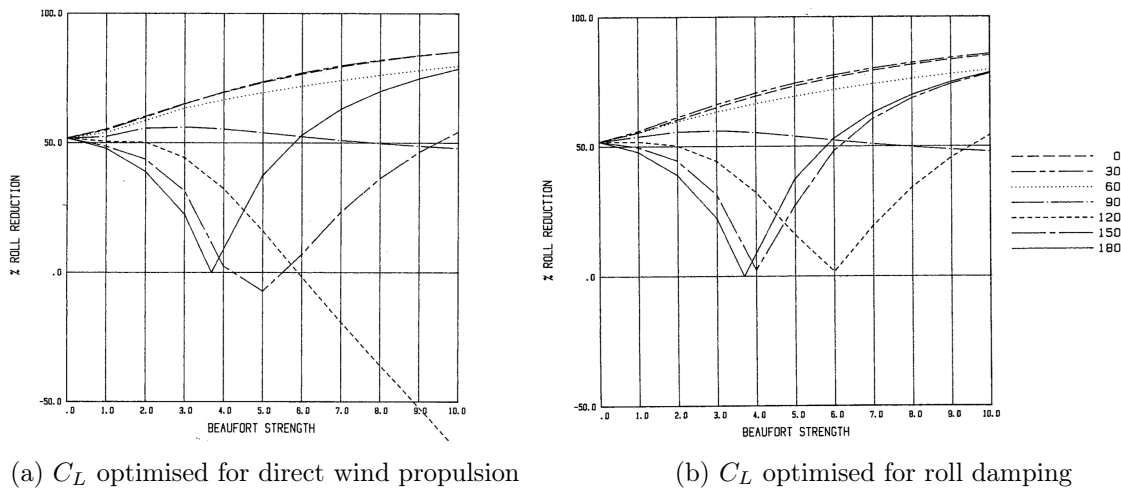


Figure 1.2: Roll reduction due to lift effects from a marine aerofoil (Satchwell, 1986). The legend shows true wind angle.

winds to avoid negative roll damping. Furthermore, control systems could be modified to directly enhance damping by targeting for example the incidence derived roll damping. The issue of knowing the exact point of stalling is introduced due to the dynamical approach and hysteresis phenomena after stalling. This implies that there should be a margin between the operating lift coefficient and the estimate of the maximum. The margin should be adjusted in relation to the incidence change due to rolling, and possibly the increased incidence changes from a potential control system.

Although the matter only seemed to be documented and not researched, fitting wingsails to a vessel was thought to also reduce the ship resistance (Satchwell, 1986). This way, it contributes to additional improved propeller efficiency and fuel savings, on top of the direct propulsion thrust. The first wind assisted Japanese vessels in the early 80s indicated a reduction in all types of motions after sail retrofit, improved course keeping ability and reduced rudder resistance. Unexplained power savings when sailing windward with furled sails were also reported. Possible processes responsible for the power savings were brought forward. Firstly, a reduction in roll motion leads to reduced coupled sway and yawing motions. These two motions combine to produce leeway, so when the leeway is reduced, the induced ship resistance is also decreased. Secondly, direct resistance due to rolling associated with separation and vortex shedding might be reduced. Thirdly, aerodynamic pitch damping will be present and reduce the pitching moment. However, the contribution might be small compared to the hydrodynamic pitch damping and Satchwell (1986) believed the sail effect on pitch to be small.

Clayton and Sinclair (1988) derived analytical expressions of the damping terms from rigid body motion. The forces and moments were expressed as the sum of a steady term and a term proportional to the rigid body velocity, leading to the damping derivative. The paper discussed the trade-off between efficient thrust production and good motion damping from rigid wingsails, as previous works had been mostly focused on the first objective. The analytical analysis took surge, sway, roll, pitch and yaw motions damping induced by surge, sway, roll and pitch motions into account, assuming the heave motion damping component to be negligible. Calculations were carried out using quasi-static lifting surface theory and linearising to the first order in the rigid body velocities. The moments and damping due to yawing were not considered due to their non-symmetry. The wingsail was assessed with an aspect ratio of 2 and rectangular planform.

Firstly, the roll induced effects were assessed. The analytical expressions showed that the condition of maximum thrust, corresponding to a large angle of attack (α), gave a large positive roll motion damping for $AWA^* < 90^\circ$ and a low positive damping for $AWA^* > 90^\circ$. Like earlier, AWA^* defines the apparent wind angle measured from the ship centreline. Smaller or negative angles of attack, corresponding to a lower thrust, showed the opposite trend; small positive damping for $AWA^* < 90^\circ$ and large positive damping for $AWA^* > 90^\circ$. Negative damping occurred at $(AWA^*) = \frac{180^\circ + \alpha}{2}$. Further on, maximum thrust was required to ensure positive pitch moment damping due to roll motion for all AWA^* . This means that for angles above 90° , maximum roll damping corresponded to minimum pitch damping.

Secondly, the pitch induced effects were evaluated. This required a negative angle of attack to ensure positive roll damping for all apparent wind angles. The general behaviour of the pitch induced roll damping coefficient was the reverse of the roll induced pitch damping coefficient. In other words, the conditions for large positive roll damping due to pitching was the opposite of those for pitch damping due to rolling. Furthermore, the pitch damping coefficient due to pitch motion was naturally equivalent to the roll induced roll damping, only shifted 90° along the AWA^* axis. Negative damping always occurred near apparent wind angles of $\alpha/2$ and $180^\circ - \alpha/2$.

The overall finding of Clayton and Sinclair (1988) was that there was no operational state of the wingsail that resulted in large positive damping for all angles in all motion modes. The requirements for large positive thrust from the rig were inconsistent with large positive damping for all apparent wind angles. In roll mode, the roll, pitch and yaw damping had small values around 90° where maximum thrust occur. However, the pitch damping due to pitch motion was effective in this state. The roll damping due to roll motion was at its maximum for angles close to 0° or 180° , corresponding to minimal thrust. An evaluation of the effect of wingsail aspect ratio indicated that an increasing aspect ratio increased the damping coefficient in all modes but yaw. The roll and pitch induced yaw damping showed the interesting result that for an infinitely large aspect ratio, the damping was zero. Its maximum occurred at a ratio of 3. Introducing a taper ratio less than 1 (where 1 corresponds to a rectangular wing) decreased the damping magnitude in all modes but yaw, while the shape as a function of apparent wing angle was kept. The yaw damping, on the contrary, was reversed when introducing a taper ratio. However, the magnitudes were small.

In a later stage, Sinclair and Clayton (1992) obtained experimental measurements of the motion damping coefficients of wingsails for comparison with the previously described theoretical analysis of Clayton and Sinclair (1988). Due to the previously reported symmetry and phase shifts between various modes and wind angles, measurements were only conducted for roll motions with apparent wind angles between 0° and 90° . Interesting factors to vary were determined to be the wind angle, roll frequency and sail aspect ratio. In order to scale inertia and viscous forces equally, the ratio of the roll linear velocity to the freestream velocity was kept constant at the top of the aerofoil. The sail model was driven in a simple harmonic motion to simulate the ship's roll motion, while the hull itself and sea surface were not modelled. These were represented by the wind tunnel ground board. The results showed that the experimental and theoretical damping corresponded to a large extent. At least for roll and pitch damping, the trends of the theoretical analysis were confirmed by the experimental results, although the coefficients were slightly different. The roll damping in beam wind was in fact larger than predicted, meaning the wingsail is a better damper than the theoretical prediction. The conclusions drawn from the theoretical analysis for roll and pitch damping were deemed valid.

Sinclair (1991) extended the analysis to include more sail systems, an improved wingsail model,

and to consider both passive and active sail damping. In addition to rigid wingsails, the damping from the vertical axis wind turbine (VAWT), horizontal axis wind turbine (HAWT), Flettner rotor and Cousteau's Turbosail were modelled, Figure 1.3. The analytical derivations were based on linearisation to the first order in roll induced horizontal velocity normalised with the apparent wind speed. The wingsail model was improved compared to the work of Clayton and Sinclair (1988) by including drag and dynamic lift by the Theodorsen function. It supported the conclusion of previous sources, that positive damping is in conflict with positive thrust for apparent wind angles above 90° . Negligible damping will always be provided in beam wind. The HAWT was found to be a beneficial device for roll stabilisation as the damping coefficient is positive for all angles and even at its maximum in beam wind where roll damping is needed the most. Although the damping is always positive, increased thrust comes at the expense of damping for angles above 90° . The VAWT has positive damping coefficients which actually do not vary with wind headings and blade pitch angles, making it an efficient roll stabiliser. The Flettner model assumed that the lift and drag forces follow the fluctuations of the apparent wind without a time lag. This represented a conservative approach as the time lag should in reality increase the damping forces and moments. The damping derivative, varying like a cosine function of the apparent wind angle, showed a conflict between thrust and damping for angles below 90° . For the Turbosail, this conflict appeared for angles above 90° , similar to wingsails. Experimental tests with wingsails concluded that the theoretical results were valid, while tests with HAWT indicated deficiency in the theory.

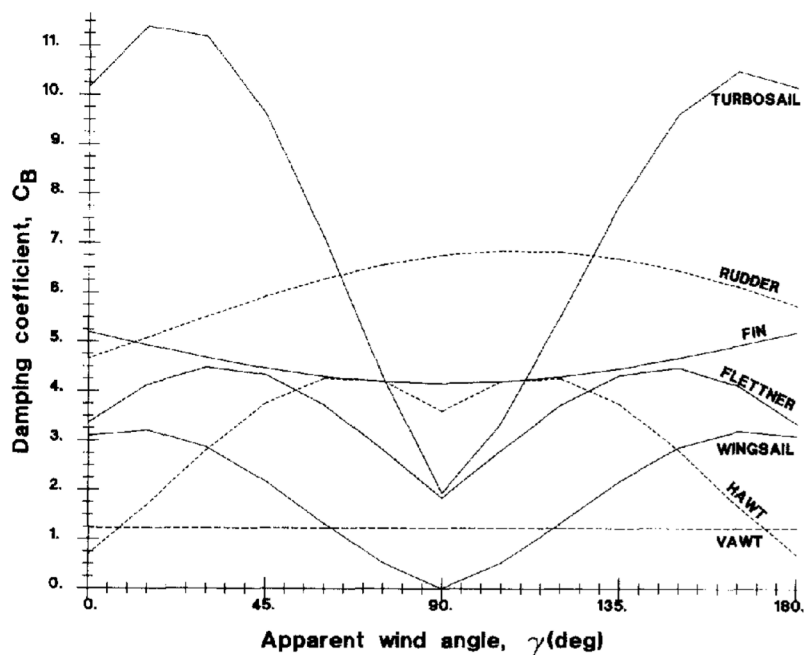


Figure 1.3: Comparison of roll damping coefficients for different wind propulsion devices. The figure is found in Sinclair (1994) but based on the work of Sinclair (1991).

Two newer contributions to the research area deserve mention. The first one is given by Copuroglu and Pesman (2018) who studied the influence of Flettner rotors on the roll motion of a ship in beam waves. The effect of roll motion on rotor performance was neglected, i.e. the apparent wind state was constant. Thus, this work is really in-between the aforementioned division of the literature review. While it does not include the effect of ship motion on the sails, it certainly fits into seakeeping literature.

Copuroglu and Pesman (2018) neglected interaction effects between rotors. With the use of CFD in a virtual wind tunnel, the work indicated that the driving and heeling force performances decrease in roll motion and are not symmetric about zero heel. The driving force seemed to be more sensitive to ship heel away from the wind, and the heeling force to angles towards the wind. Furthermore, the ship roll motion analysis assumed a one degree of freedom nonlinear roll equation of motion which included the heeling moment induced by the Flettner rotors as a function of heeling angle. Although the Flettner rotors affected the maximum roll angles compared to a case without rotors, they did not affect nonlinear characteristics of roll motions. Copuroglu and Pesman (2018) concluded that they almost acted as constant heeling forces for angles between 25° to port and starboard side, implying that the influence of heel angle on heeling moment can be neglected within this range.

The second newer contribution is given by Eggers and Kisjes (2019) who extended the conventional manoeuvring and seakeeping direct free running model tests to include aerodynamics of sails. According to Eggers and Kisjes (2019), the work and observations should be considered as a first scan, requiring wider testing of design and conditions for a generalised conclusion. In a simplified wind tunnel, model tests were performed to investigate the unsteady sailing scenarios for a ship with three DynaRigs and Flettner rotors. These included the classical manoeuvring zig-zag test, speed runs, roll decay tests, and a seakeeping test in regular and irregular stern quartering waves. Thus, an experimental set-up modelling both the aerodynamic and hydrodynamics for a sailing ship was developed.

Eggers and Kisjes (2019) brought forward the need of different manoeuvring requirements for wind assisted vessels compared to the current standard (IMO, 2002), because the sails introduce side forces that lead to non-zero rudder and drift angles in calm water sailing conditions. The roll decay tests with DynaRigs showed that damping increased when the ship was sailing with a forward velocity in no wind, compared to the case of zero ship velocity. Furthermore, it increased significantly when wind was included, observing values otherwise not obtainable for commercial vessels without special roll reducing devices. The vessel with Flettner rotors also showed increased damping, but this was modest compared to the hydrodynamic damping. Seakeeping tests were conducted to observe changes in course keeping as a function of the sail thrust. Increased Flettner rotor thrust, and decreased flow over the rudder, resulted in a higher heading variation, confirming the hypothesis that there might be a challenge in course keeping in stern quartering waves.

1.2.2 Power performance literature

Due to the recent attention in the performance of WAPS, the literature in this area is much more updated than the seakeeping literature. Reche (2020) and Tillig (2020) developed performance prediction programmes for ships utilising WAPS to assess and predict propulsion power and fuel consumption. Lu and Ringsberg (2020) utilised the latter author's programme to study and compare the fuel savings of three different WAPS technologies; the Flettner rotor, a wingsail and the DynaRig. The work also included a parametric study of a Flettner rotor, to investigate the effect of rotor dimensions and operational conditions on fuel savings.

Viola et al. (2015) investigated the required combined thrust from wingsails and propeller to achieve a given ship velocity, while trimming the sails to minimise the propeller thrust. The influence of wingsail aspect ratio was investigated, however interaction effects between several sails were neglected. A range of true wind angles from 15° to 165° were trialled. In literature, 30° of TWA is commonly used as a minimum in analyses of wind assisted ship performance as

useful thrust cannot be generated at angles below this value (Persson et al., 2019; Tillig and Ringsberg, 2020).

In relation to the development of the wPCC project, researchers at SSPA and KTH in Sweden have performed and published work related to various aspects of wind assisted propulsion. Persson et al. (2019) implemented simplified approaches of modelling WAPS as an alternative to using costly 3D computational fluid dynamics (CFD). The proposed methods used a limited number of 2D or 3D CFD simulations, which were extrapolated to represent 3D effects. Interaction effects with ship hull and other WAPS devices were not considered and the solution was demonstrated on a wingsail and a Flettner rotor. Three methods were evaluated for the wingsail; sectional integration with 3D-correction using Prandtl's lifting line theory (SILL), non-linear lifting line algorithm (NL-LL) and a vortex lattice method (VLM) code assuming potential flow.

The SILL method used the results from 2D CFD simulations of the foil to generate a table describing the relation between lift, drag and pitching moment coefficients as a function of angle of attack. The wingsail was discretised along the span to compute the apparent wind, angle of attack and local force and moment coefficients at each section from the interpolated 2D table values. The total sail forces were obtained by vertical integration and corrected for 3D effects by assuming an elliptical lift distribution. The NL-LL method was similar to the SILL method but used an iterative approach to solve the lift distribution, a so-called circulation-coupled iterative algorithm.

For the Flettner rotor, a 3D sectional integration method (3D-SIM) was used. This method was based on performing 3D CFD simulations of the rotor at a range of spin ratios, dividing the rotor into a number of sections in the span-wise direction and extracting the sectional lift and drag coefficients in the coordinate system of the local inflow. Then, at a given ship speed and wind condition, the sectional apparent wind, local spin ratio and forces were calculated, using the extracted coefficients. The total sail forces were obtained by span-wise integration.

Comparing the methods to 3D CFD, the results showed that the SILL method best predicted the lift and drag up to an angle close to stall. Furthermore, the resulting upwind ship speed was well predicted by the SILL method and poorly predicted by the N-LL and VLM. However, all methods were unreliable at stalling angles. As for the Flettner rotor, the 3D-SIM method predicted the rotor forces with less than 4.3% difference and an even smaller error in fuel prediction. Persson et al. (2019) concluded that the 3D-SIM method is a viable tool for route simulations and that the SILL method is usable in combination with 3D CFD simulations in the concept design phase of wingsails at pre-stall angles.

1.3 Objectives

The literature review uncovered scarce research on the seakeeping of a vessel with wind assisted propulsion. A series of papers (Clayton, 1987; Clayton and Sinclair, 1988; Sinclair, 1994; Sinclair and Clayton, 1992; Sinclair, 1991) focused on the isolated aerodynamic system and damping result, while one is yet to combine a mathematical aerodynamic model with hull motion derivatives (Clayton and Sinclair, 1988).

This leads to the main objective of the present thesis, which is to provide an understanding of how a wind assisted propulsion system influences the seakeeping capabilities of a ship. In particular, the focus is directed towards the effect of a ship's rigid body motions on the aerodynamics of a sail system and vice versa. Related questions to the objective are:

- Which mechanisms are dominant in the aerodynamic damping of a vessel?
- In which conditions is aerodynamic damping important for ship motion?

In relation to the first objective, a second, supportive objective can be defined. A linear damping model will be assumed during the analysis, and its applicability to sail damping is to be investigated. The work aims to determine in what situations such an approach may be valid, and whether it is applicable in sailing conditions where the aerodynamic damping plays a significant role in ship motions.

The practical implications of the above objectives are to estimate aerodynamic damping coefficients and assume them to be independent of the hydrodynamic coefficients. These are then combined under the assumption of superposition. Furthermore, the superposed system will be used to estimate the sail's influence on the seakeeping of a ship.

1.4 Structure of the thesis

The present study is divided into nine chapters, including this introduction.

Chapter 2 provides the theoretical foundation on ship hydrodynamics that is required for the work of this thesis. It describes regular and statistical modelling of waves and the ship response in both regular and irregular waves. Furthermore, important hull resistance components for a wind assisted vessel and their modelling are described.

Similarly, *chapter 3* give the theoretical foundation on aerodynamics of two sail systems. These are the Flettner rotor and rigid wingsail.

Chapter 4 describes the implementation of aerodynamic theory in the aerodynamic damping model created in this thesis work. Assumptions of the model are made clear, and a code algorithm is presented.

Chapter 5 verifies the aerodynamic model of chapter 4. The verification is dual. Firstly, the steady sail force generation is compared to results of literature, and secondly, the damping model is verified against an analytical model of previous works.

Chapter 6 describes the model of the wind assisted ship in this thesis, including the example vessel and sea states used in the calculations. The assumptions of the combined aerodynamic and hydrodynamic model, and the methodology of the calculations are described.

Chapter 7 presents the result of the previously described models. Firstly, results of the isolated aerodynamic model are given. Secondly, results of the wind assisted ship model are provided to assess the importance of sails in the larger ship system. The independent results are discussed consecutively as they are presented.

Chapter 8 discusses the previously presented results in a larger context and in relation to each other. Additionally, the validity of two major simplifications in the model are discussed.

Chapter 9 concludes the work and highlights the most important findings. Suggestions for further work are outlined.

Chapter 2

Ship hydrodynamics

This chapter presents hydrodynamic theory, related to waves, wave induced ship motion and ship resistance. The reader is assumed to possess general knowledge on fluid dynamics and regular wave theory. The chapter is intended to provide a theoretical base for the ship model of this work, presented in chapter 6. Parts of the theory is also required for the aerodynamic sail model in chapter 4. Thus, this chapter does not provide a complete theoretical review on ship hydrodynamics, but focuses on relevant subjects for this thesis.

2.1 Short-term statistical description of waves

Statistical estimates of an irregular sea can be simulated by linear theory (Faltinsen, 1993) and a wave spectrum is used to describe the energy distribution of individual wave frequencies. The wave elevation of a long-crested irregular sea is the sum of a large number of regular wave components of different amplitudes, A , frequencies, ω_0 , wave number, k , and phases, ϵ ,

$$\zeta = \sum_{j=1}^N A_j \sin(\omega_{0j}t - k_j x + \epsilon_j), \quad (2.1)$$

where the subscript j refers to the wave component number. The waves propagate in the x -direction. The phases are random and uniformly distributed in the range $[0, \pi]$, to recover the statistical behaviour in time. The amplitude of each component can be expressed by the wave spectrum, $S(\omega)$,

$$\frac{1}{2}A_j^2 = S(\omega_j)\Delta\omega, \quad (2.2)$$

where $\Delta\omega$ is a constant spacing between adjacent frequencies. The application of a wave spectrum implicitly assumes that the sea can be described as a stationary and random process, i.e. it is a short-term description. A large set standardised wave spectra has been suggested. The two most relevant for ships are the Pierson-Moskowitz (PM) and Joint North Sea Wave Project (JONSWAP) spectrums, frequently applied for wind seas (DNV-RP-C25, 2010). Both are single peak, one-dimensional wave spectra, i.e. without wave energy spreading. The PM spectrum, Equation (2.3), is proposed for fully developed sea states, while the JONSWAP, Equation (2.4), include fetch limited seas and thus describe developing seas. The JONSWAP formulation is a modification of the PM spectrum and includes a dimensionless peak shape parameter, γ . Figure 2.1 show the spectrum for different peak shape values. For γ equal to 1, the PM spectrum

is recovered.

$$S_{\text{PM}}(\omega) = \frac{5}{16} H_S^2 \omega_p^4 \omega^{-5} \exp \left\{ -\frac{5}{4} \left(\frac{\omega}{\omega_p} \right)^{-4} \right\} \quad (2.3)$$

$$S_J(\omega) = A_\gamma S_{\text{PM}}(\omega) \cdot \gamma \exp \left\{ -0.5 \left(\frac{\omega - \omega_p}{\sigma_J \omega_p} \right)^2 \right\} \quad (2.4)$$

where

ω_p is the angular spectral peak frequency,

H_S is the significant wave height,

σ_J is the spectral width parameter which takes average values of $\sigma_a = 0.07$ for $\omega \leq \omega_p$ and $\sigma_b = 0.09$ for $\omega > \omega_p$,

$A_\gamma = 1 - 0.287 \ln \gamma$, is a normalising factor.

The JONSWAP spectrum is expected to be a reasonable model for $3.6 < T_p/\sqrt{H_S} < 5$. According to DNV-RP-C25 (2010), the following peak parameter may be applied,

$$\gamma = \begin{cases} 5 & \text{for } T_p/\sqrt{H_S} \leq 3.6 \\ \exp \left(5.75 - 1.15 \frac{T_p}{\sqrt{H_S}} \right) & \text{for } 3.6 < T_p/\sqrt{H_S} < 5. \\ 1 & \text{for } 5 \leq T_p/\sqrt{H_S} \end{cases} \quad (2.5)$$

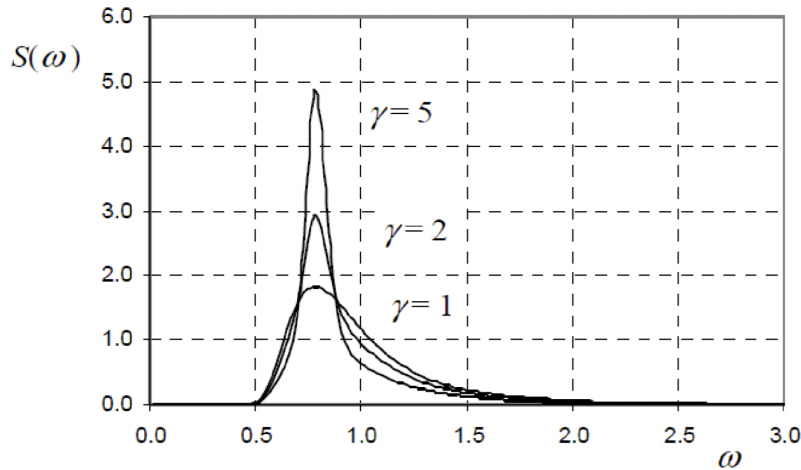


Figure 2.1: The JONSWAP spectrum for $H_S = 4.0$ m, $T_p = 8.0$ s and different values of γ (DNVGL-CG-0130, 2018).

The moments of the spectrum given in terms of order n , Equation (2.6), define the statistical parameters. The variance is the area of the spectrum, i.e. it is simply the zeroth moment, Equation (2.7),

$$m_n = \int_0^\infty \omega^n S(\omega) d\omega \quad n = -1, 0, 1, 2, \dots, \quad (2.6)$$

$$\sigma^2 = m_0 = \int_0^\infty S(\omega) d\omega. \quad (2.7)$$

Within the assumptions of a normally distributed wave elevation and a stationary and ergodic wave process, the significant wave height is

$$H_S = H_{m0} = 4\sqrt{m_0}, \quad (2.8)$$

where the definition of the significant wave height is the average value of the highest one-third part of the wave height in the irregular sea.

2.2 Linear wave induced ship motion

Linear theory implies that the wave induced motion and loads on a ship or structure are linearly proportional to the wave amplitude. It requires that the wave steepness is small, i.e. the waves are far from breaking.

2.2.1 Response in regular waves

A ship or floating structure is defined as a rigid body, free to move in the six degrees of freedom. The translatory displacements surge (η_1), sway (η_2) and heave (η_3) are in the x-, y- and z-direction, respectively. The rotational displacements around these axes are roll (η_4), pitch (η_5) and yaw (η_6), respectively. See Figure 2.2 for reference. The motion of any point in (x, y, z) on the body is written as

$$\vec{s} = (\eta_1 + z\eta_5 - y\eta_6)\vec{i} + (\eta_2 - z\eta_4 + x\eta_6)\vec{j} + (\eta_3 + y\eta_4 - x\eta_5)\vec{k}, \quad (2.9)$$

where \vec{i} , \vec{j} and \vec{k} are unit vectors along the x-, y- and z-axis, respectively.

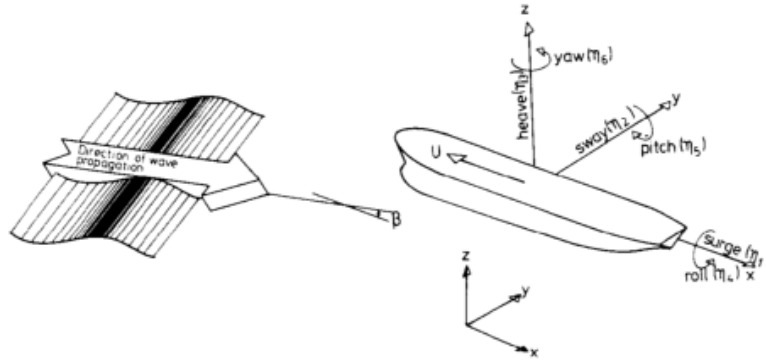


Figure 2.2: Coordinate system definition with rigid body motion modes (Faltinsen, 1993).

As a consequence of linear theory and steady-state conditions, the response in mode k oscillates with the frequency of the disturbance,

$$\eta_k = \eta_{ka} \cos(\omega_e t + \delta_k) \quad k = 1, \dots, 6, \quad (2.10)$$

or, in its complex form,

$$\eta_k = \tilde{\eta}_k e^{-i(\omega_e t + \delta_k)}. \quad (2.11)$$

Here, η_{ka} and $\tilde{\eta}_{ka}$ are the real and complex motion amplitudes, respectively, and δ_k is the phase angle of the response with respect to the excitation load. Due to the ship forward motion, the relevant frequency is the encounter frequency defined by the incident wave frequency ω_0 and the ship velocity V_S ,

$$\omega_e = \omega_0 + \frac{\omega_0^2 V_S}{g} \cdot \cos \beta_w, \quad (2.12)$$

where g is the gravitational acceleration and β_w is the relative wave heading between the vessel and the wave propagation direction.

The responses are found by solving the equations of rigid body motions. For steady-state sinusoidal motions, these can be written as

$$\sum_{k=1}^6 [(M_{jk} + A_{jk})\ddot{\eta}_k + B_{jk}\dot{\eta}_k + C_{jk}\eta_k] = F_j e^{-i\omega_e t} \quad j = 1, \dots, 6, \quad (2.13)$$

where j_k denote the components of the following matrices: M is the generalised mass matrix of the ship, A is the added mass matrix, B is the damping matrix and C is the stiffness matrix. F is the vector of complex excitation force and moment amplitudes. The added mass, damping and excitation force terms are frequency-dependent. Furthermore, a dependency on ship velocity is stated explicitly through the pressure term in the Bernoulli equation and implicitly through the variation in the body boundary conditions of the fluid (Faltinsen, 1993).

The response is commonly expressed through the response amplitude operator (RAO). Equation (2.14) presents the RAO in mode k , which is obtained by using the complex form of the response expressed in Equation (2.11). The RAO is the transfer function of the body motion, i.e. the response amplitude per unit wave amplitude (Newman, 2018),

$$|H_k(\omega_e, \beta_w)| = \left| \frac{\eta_{ka}}{\zeta_a} \right| = \left| \sum_{j=1}^6 \frac{X_j(\omega_e, \beta_w)}{-\omega_e^2(M_{jk} + A_{jk}(\omega_e)) + i\omega_e B_{jk}(\omega_e) + C_{jk}} \right|, \quad (2.14)$$

where ζ_a is the wave amplitude of the regular wave. X_j is the transfer function of the excitation load, i.e. the quantity giving the load amplitude per unit wave amplitude, $|F_j(\omega_e, \beta_w)| = \zeta_a |X_j(\omega_e, \beta_w)|$. Due to linearity, $H_k(\omega_e, \beta_w)$ is independent upon the wave amplitude. Without the absolute value of Equation (2.14), the expression becomes a more general transfer function of the motion, which provides both the motion amplitude per unit wave amplitude and the phase of the motion relative to the incident waves.

2.2.2 Short term statistics of the response

As a result of linear theory, the response in irregular waves can be studied as the sum of the response to regular waves of different amplitudes, wavelengths and propagation directions (Faltinsen, 1993). In practice, it is done by obtaining a response spectrum from the combination of a response transfer function and a wave spectrum. The linear superposition of the response from different long-crested wave components is

$$\sum_{j=1}^N A_j |H(\omega_j)| \sin(\omega_j t + \delta(\omega_j) + \epsilon_j), \quad (2.15)$$

where A_j and ϵ_j were defined in relation to Equation (2.1), and $|H(\omega_j)|$ and $\delta(\omega_j)$ in relation to Equation (2.14) and (2.11), respectively. Similarly as for the statistical description of waves, the n 'th moment of the response spectrum, $m_{\eta,n}$, is given by Equation (2.16). When the number of wave components in Equation (2.15) goes to infinity and $\Delta\omega$ goes to zero, the variance of the response is described in Equation (2.17) (DNVGL-CG-0130, 2018), where the subscript r denotes the response, to separate it from the variance of the wave spectrum.

$$m_{\eta,n} = \int_0^\infty |\omega|^k |H(\omega)|^2 S(\omega) d\omega, \quad (2.16)$$

$$\sigma_r^2 = \int_0^\infty |H(\omega)|^2 S(\omega) d\omega \quad n = 0, 1, 2, \dots \quad (2.17)$$

The statistical properties of the responses are then calculated from the moments of the response spectrum. The standard deviation of the response is

$$\sigma_r = \sqrt{m_{\eta,0}}. \quad (2.18)$$

The significant response amplitude, η_s , defined as the mean amplitude of the highest one-third part of the amplitudes, is found from the standard deviation,

$$\eta_s = 2\sigma_r = 2\sqrt{m_{\eta,0}}. \quad (2.19)$$

2.3 Hull resistance

The total resistance of a ship under a representative sea condition is the sum of the resistance in calm water, the added resistance in wind and the added resistance in waves (ITTC, 2018). These three components are described in the following section. However, the resistance due to wind is added to the section on calm water resistance because it is included by the relative air resistance in this thesis, rather than an independent wind resistance. In addition to the ITTC recommendation, an added resistance due to drift of a sailing vessel is required.

2.3.1 Calm water resistance

The total calm water resistance of a ship at zero drift and without bilge keels can be divided into six components (ITTC, 2017). These are the frictional, hull surface roughness, wave, appendage, wind and correlation resistances. The correlation resistance is included to obtain the best agreement between model test and full scale trials. Different ship model tanks have their own correlation factor because it is highly dependent upon the performance prediction procedure used. At SINTEF Ocean, the standard prognosis method also include a resistance due to the transom stern (D. Fathi et al., 2021). Given in terms of force coefficients, the total calm water resistance is summarised as

$$C_{T,CW} = C_W + C_V + C_{APP} + C_{BD} + C_{AA} + C_A, \quad (2.20)$$

and the coefficients are the result of normalising the resistance by the water density, ρ_w , ship velocity and hull wetted surface, S ,

$$C = \frac{R}{\frac{1}{2}\rho_w V_S^2 S}. \quad (2.21)$$

The subscripts W, V, APP, BD, AA and A denote wave, viscous, appendage, transom stern, air and correlation, respectively. The viscous resistance coefficient is composed of the frictional resistance coefficient, C_F , and the resistance coefficient due to hull roughness, ΔC_F ,

$$C_V = (1 + k)(C_F + \Delta C_F), \quad (2.22)$$

where k is the hull form factor. The frictional resistance may be determined by the ITTC-57 correlation line,

$$C_F = \frac{0.075}{(\log_{10}(\text{Re}) - 2)^2}, \quad (2.23)$$

where Re is the Reynolds number based on the ship velocity and length, and the water viscosity, ν ,

$$\text{Re} = \frac{V_S L}{\nu}. \quad (2.24)$$

A suggested empirical formula for the hull roughness resistance is given by ITTC (2018), but the standard roughness correction applied at SINTEF Ocean is

$$\Delta C_F = [110(k_s \cdot V_S)^{0.21} - 403] \cdot C_F^2, \quad (2.25)$$

where the ship velocity is given in m/s. k_s is the average height of roughness given in μm . This property is usually denoted H by SINTEF Ocean, but is changed in this thesis to avoid confusion with the sail height (see chapter 3). In the design stage of a ship, the value 150 is normally used for k_s as a standard value (Steen and Minsaas, 2014).

There are many methods of determining the form factor. These include low speed towing tests, geosim tests, Prohaska's method or empirical formulae. The empirical expression used at SINTEF Ocean is

$$k = 0.6\phi + 145\phi^{3.5}, \quad \text{where} \quad \phi = \frac{C_B(L_{WL})}{L_{WL}} \sqrt{(T_{AP} + T_{FP}) \cdot B}. \quad (2.26)$$

C_B is the ship block coefficient, L_{WL} is the ship length in the waterline and B is the moulded breadth. T_{AP} and T_{FP} are the draught at aft and fore perpendiculars, respectively.

The wave resistance coefficient is calculated from the total and frictional resistance of the model in a resistance test (ITTC, 2017),

$$C_W = C_{Tm} - C_{Fm}(1 + k), \quad (2.27)$$

where m denotes the model. The residual resistance coefficient, C_R , is commonly used instead of the wave resistance. The concept of the two components are the same, they both arise from the assumption of William Froude that the resistance which is left when the viscous resistance is subtracted from the total resistance, is mainly composed of the wave resistance. The wave resistance is equal in model and full scale when Froude similarity is applied. The Froude number is defined as,

$$\text{Fn} = \frac{V_S}{\sqrt{gL}}. \quad (2.28)$$

The principal is still the fundamental concept of model testing today; to subtract all non-Froude scaled resistance components. However, additional Reynolds dependent terms, like the form drag, air drag and transom stern drag, are subtracted to obtain the residual resistance coefficient (Steen and Minsaas, 2014). Empirical formulae have been developed to determine the residual coefficients, like the Hollenbach's regression line. It is further discussed below.

The base drag and air resistance coefficients are given by Equation (2.29) and (2.30),

$$C_{BD} = \frac{0.029 \left(\frac{S_B}{S}\right)^{3/2}}{\sqrt{C_F}}, \quad (2.29)$$

$$C_{AA} = 0.001 \frac{A_p}{S}, \quad (2.30)$$

where S_B is the wetted surface of the transom stern and A_p is the transverse projected area above the waterline. The ratio of A_p to S in the air resistance coefficient arises from the desire to obtain a coefficient which is normalised by the wetted surface, like in Equation (2.21). When the ship is subject to wind, ITTC (2018) suggest the wind resistance to be added to the calm water resistance. However, an alternative is to calculate the air resistance from the relative wind, Equation (2.31), instead of the ship velocity as presented in Equation (2.21),

$$V_{\text{air,r}} = V_S + \bar{V}_T \cos(\text{TWA}), \quad (2.31)$$

where TWA is the true wind angle and \bar{V}_T is the mean true wind velocity over the area above the waterline. The mean is required due to the atmospheric boundary layer, see chapter 4. Additionally, the direction of the relative wind must be accounted for. If the wind component in the ship velocity direction is larger than the ship velocity, i.e. $V_{\text{air},r}$ in Equation (2.31) is negative, the relative wind is in the ship direction. The force is no longer a resistance and must be subtracted from the other calm water resistance components. However, the negative sign is lost when the velocity is squared in Equation (2.21). Thus, a factor must be multiplied with the wind and air resistance to preserve the sign,

$$\frac{|\cos(\text{TWA})|}{\cos(\text{TWA})}, \quad (2.32)$$

such that the relative air resistance is

$$R_{AA,r} = \frac{1}{2} \frac{|\cos(\text{TWA})|}{\cos(\text{TWA})} \rho_w C_{AA} V_{\text{air},r}^2 S. \quad (2.33)$$

Hollenbach regression

In 1998, Hollenbach published a regression analysis of approximately 430 ships tested in the Vienna Ship Model Basin (Hollenbach, 1998). The basin is one of the oldest ship model tanks in the world, but the regression is based on model tests from 1980 to 1995. The analysis was performed to test the applicability of more traditional methods like Holtrop and Mennen (1982) to the modern hulls at that time. The result of the Hollenbach method is a mean resistance curve. Furthermore, it includes formulae for the lower and upper envelope curves of the statistical data, which is not included in the classical methods. These are the “maximum” and the “minimum” cases and are exceeded in only 5% of the cases. Hollenbach (1998) stated that the “minimum” resistance is an estimate of what can be achieved by excellent lines without severe constraints from the design after considerable computer and model test investigation, while the “maximum” represent the unusual constraints from the overall design.

The regression analysis uses a length parameter called length over surface, L_{OS} and the Froude number is based on a length that is a function of the L_{OS} . Hollenbach used a somewhat different division of the resistance components than the common ITTC practice. The residual coefficient is defined by the ship breadth, B , and draught, T , not wetted surface as in Equation (2.21),

$$C_{R,\text{Hollenbach}} = \frac{R_R}{\frac{1}{2} \rho_w V^2 B T}. \quad (2.34)$$

Due to its length and several new parameters that require detailed definitions, the expression of $C_{R,\text{Hollenbach}}$ is not reproduced in this work, but may be consulted in Hollenbach (1998).

The original work of Hollenbach determined the residual coefficient by assuming a form factor of zero for all ship hulls. This assumption may be too rough for full scale prognosis and a conversion of Hollenbach’s data to include a form factor may improve the situation. In the ShipX Ship Speed and Powering Plug-In, the residual coefficient is recalculated to obtain a coefficient with the same definitions as in the standard SINTEF Ocean model tests (D. Fathi et al., 2021). Thus, it may be applied to the standard scaling method for resistance force. The conversion is done by setting the total resistance from the Hollenbach formulation equal to the total resistance from the ITTC formulation (recall Equation (2.27), but now using the residual coefficient instead of wave resistance coefficient),

$$C_{Fm} + C_{R,\text{Hollenbach}} \frac{B T}{S} = C_{Fm}(1 + k) + C_R, \quad (2.35)$$

where the subscript m denotes the model coefficient, as opposed to the full scale ship coefficient. The model length is assumed to be a standard length of 6.5 m. One then obtains the modified Hollenbach residual coefficient,

$$C_R = C_{R,Hollenbach} \frac{BT}{S} - k \cdot C_{Fm}, \quad (2.36)$$

which can be applied in the standard scaling method. C_{Fm} follows from Equation (2.23) using the Reynolds number of the 6.5 m long model.

2.3.2 Added resistance in waves

When a ship is moving with a forward speed in waves, it experiences an additional resistance that is not captured by the calm water resistance. It is the same as the longitudinal drift-force components, but is commonly referred to as the added resistance in waves, R_{AW} . The resistance is a non-viscous, second-order mean wave load. With reference to Figure 2.3, there are two main features of the added resistance in waves for a ship at moderate Froude numbers in head sea regular waves (Faltinsen, 1993). At small wavelengths, typically $\lambda/L < 0.5$, the resistance is mainly due to reflection off the bow of the ship, while the resistance due to ship motions is dominant in larger wavelengths. The maximum occurs when the wavelength is in the order of the ship length.

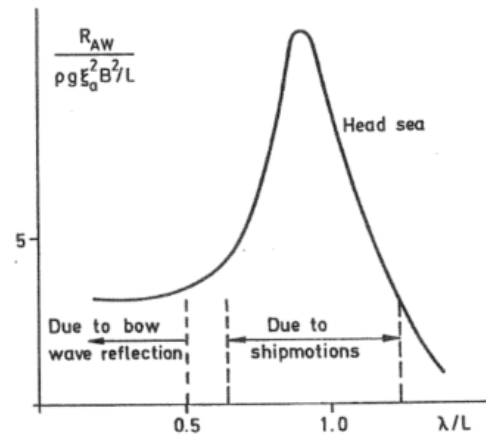


Figure 2.3: Typical wavelength dependency of added resistance of a ship in waves. λ is the wavelength and L is the ship length (Faltinsen, 1993).

Equation (2.37) presents a formula for the added resistance in waves of small wavelengths, valid for small Froude numbers and blunt ship forms (Faltinsen, 1993). It considers all wave headings.

$$\frac{R_{AW}}{\zeta_a^2} = \frac{1}{2} \rho_w g \left(1 + \frac{2\omega_0 V_S}{g} \right) \int_{L_1} \sin^2 \theta n_1 dl. \quad (2.37)$$

The integration is performed over the non-shadow part of the waterplane curve and the formula is therefore sensitive to the geometrical shape in bow region. θ is an angle related to the bow shape, see Figure 5.8 in Faltinsen (1993).

In longer wavelengths, another widely used formula for R_{AW} is derived by Gerritsma and Beukelman (1972), Equation (2.38). It is based on a strip theory approximation, such that it assumes that the variations of the flow in the cross-sectional plane are much larger than the variations of the flow in the longitudinal directions (Faltinsen, 1993). The expression should be used with care for unconventional ships and at small wavelengths, because it neglects the effect of wave reflection off the bow of the ship.

$$R_{AW} = \frac{k}{2\omega_e} \int_L \left(B_{33}^{(2D)} + V_S \frac{d}{dx} A_{33}^{(2D)} \right) V_{za}^2(x) dx, \quad (2.38)$$

where L is the ship length over which the integration is performed, k is the wave number and $B_{33}^{(2D)}$ and $A_{33}^{(2D)}$ are the two-dimensional damping and added mass coefficients, respectively. V_{za} is amplitude of the relative vertical velocity between the ship and the waves,

$$V_z = \dot{\eta}_3 - x\dot{\eta}_5 + V_S \eta_5 - \dot{\zeta}^*. \quad (2.39)$$

$\dot{\zeta}^*$ is the time derivative of the effective vertical wave displacement,

$$\dot{\zeta}^* = \dot{\zeta} \left(1 - \frac{k}{y_w} \int_{-T}^0 y \exp\{kz\} dz \right), \quad (2.40)$$

where ζ is the instantaneous wave elevation, y_w is the half width of the designed waterline and (y, z) are points of the section at x in the ship-fixed coordinate system axes. The integration is performed over the ship draught. In the original paper of Gerritsma and Beukelmann (1972), the differential variable in the integral of Equation (2.40) is given as dx , not dz . However, given draught as the integral limit, the differential variable is assumed to be a typing error. The author of this thesis has therefore taken the liberty to reproduce what is thought to be the correct expression, Equation (2.40). Because of V_{za} , the quality of the prediction of the added resistance is sensitive to the accuracy of the relative vertical velocity. Furthermore, it is seen from Equation (2.38) that the added resistance varies with the squared wave height, because V_{za} is proportional to it.

Loukakis and Sclavounos (1978) extended the analytical expression of Gerritsma and Beukelmann (1972) to allow for the calculation of added resistance in oblique waves. While the derivation and final expression are too extensive to be reproduced here, it is on the form

$$|R_{AW}| = |R_T \cos(\beta_w)|, \quad (2.41)$$

$$|R_T| = \frac{k}{\omega_e} (P_{35} + P_{26} + P_4) + \frac{2k}{\omega_e} P_{24}, \quad (2.42)$$

where R_T is the mean horizontal resistance in the wave direction β_w . The wave number of the incident waves is k . The integrals of P_{35} , P_{26} , P_4 and P_{24} can be found in the original source (Loukakis and Sclavounos, 1978).

2.3.3 Increased resistance due to drift

This section is to a certain extent based on parts of the project thesis written by this author during the autumn of 2020. Although many sources (Fujiwara, Hearn, Kitamura, Ueno, and Minami, 2005; Kramer et al., 2016a, 2016b; Tillig and Ringsberg, 2020; van der Kolk, 2016) were reviewed for that work, further work of this master thesis include more research on the topic.

The main effect of the interaction between the sails and hull of a wind assisted ship is the induced drift angle of the ship. The large side force created by the sails must be balanced by a hydrodynamic side or lift force in the opposite direction, produced by the hull and potentially also the rudder. This leads to an induced drag resistance, which is absent in the calm water resistance calculations. According to Tillig and Ringsberg (2020), the distribution of the side force between the hull and rudder is coupled with the position of the sails and the superstructure. Even though the main focus of this section is predicting the added resistance due to drift, the side and drag forces are closely connected. Thus, the prediction of them both is included in this section.

It is common to estimate the drift induced side force and drag based on empirical manoeuvring equations. In recent literature, a trend is to express the hydrodynamic forces and moments by a so-called MMG model (Sukas et al., 2019). It is a simplified model that decomposes the total forces and moments into components from the hull, rudder and propeller. A big advantage of the model is that it allows for the inclusion of hull-propeller-rudder interaction. While manoeuvring equations are usually expressed in terms of the horizontal degrees of freedom surge, sway and yaw, the roll degree of freedom is also relevant in a wind assisted ship context. To obtain the

flow oriented resistance of the ship, such that it can be added to the calm water resistance and added resistance in waves, the manoeuvring forces must be corrected with respect to the drift angle.

Yasukawa and Yoshimura (2015) introduced the MMG standard method and formulated the hydrodynamic forces acting on the hull as functions of the lateral ship velocity, v_m , and yaw rate, r . See Figure 2.4 for reference. The ship drift angle is then expressed by the relation between the lateral velocity and the longitudinal velocity component, u ,

$$\beta = \arctan\left(\frac{-v_m}{u}\right). \quad (2.43)$$

In the context of a steady sailing condition of a wind assisted ship, the yaw rate is zero. The non-dimensional hydrodynamic forces on the hull in surge, sway and yaw reduces to functions of lateral velocity only,

$$X'_H = -X'_0 + X'_{vv}v'^2 + X'_{vvv}v'_m{}^4, \quad (2.44)$$

$$Y'_H = Y'_v v'_m + Y'_{vv}v'_m{}^3, \quad (2.45)$$

$$N'_H = N'_v v'_m N'_{vv}v'_m{}^3, \quad (2.46)$$

where H denote the hull and the prime symbol indicate non-dimensional forms. X'_0 is the calm water resistance. The forces are made dimensionless according to Equation (2.47) and the yaw moment according to Equation (2.48),

$$X', Y' = \frac{X, Y}{\frac{1}{2}\rho_w V_S^2 \cdot L_{PP} T}, \quad (2.47)$$

$$N' = \frac{N}{\frac{1}{2}\rho_w V_S^2 \cdot L_{PP}^2 T}, \quad (2.48)$$

where L_{PP} is the ship length between perpendiculars.

Fujiwara, Hearn, Kitamura, Ueno, and Minami (2005) included the influence of both drift and heel angle expressed in the hydrodynamic derivative form to the external loads on the ship, consistent with the common MMG model. While the expressions were suggested in another work, the original source is written in Japanese and cannot be revised in this thesis. Equation (2.49) to (2.52) describe the non-dimensional surge, sway, roll and yaw forces on the hull,

$$X'_H = X'_0 + X'_{\beta\beta}\beta^2 + X'_{\beta\Phi}\beta\Phi + X'_{\Phi\Phi}\Phi^2 + X'_{\beta\beta\beta\beta}\beta^4, \quad (2.49)$$

$$Y'_H = Y'_{\beta}\beta + Y'_{\Phi}\Phi + Y'_{\beta\beta\beta}\beta^3 + Y'_{\beta\beta\Phi}\beta^2\Phi + Y'_{\beta\Phi\Phi}\beta\Phi^2 + Y'_{\Phi\Phi\Phi}\Phi^3, \quad (2.50)$$

$$K'_H = K'_{\beta}\beta + K'_{\Phi}\Phi + K'_{\beta\beta\beta}\beta^3 + K'_{\beta\beta\Phi}\beta^2\Phi + K'_{\beta\Phi\Phi}\beta\Phi^2 + K'_{\Phi\Phi\Phi}\Phi^3, \quad (2.51)$$

$$N'_H = N'_{\beta}\beta + N'_{\Phi}\Phi + N'_{\beta\beta\beta}\beta^3 + N'_{\beta\beta\Phi}\beta^2\Phi + N'_{\beta\Phi\Phi}\beta\Phi^2 + N'_{\Phi\Phi\Phi}\Phi^3, \quad (2.52)$$

The surge and sway forces and the yaw moment are made dimensionless according to the common normalisation of Equation (2.47) and (2.48). The roll moment is made dimensionless according to,

$$K' = \frac{K}{\frac{1}{2}\rho_w V_S^2 \cdot L_{PP} T^2}. \quad (2.53)$$

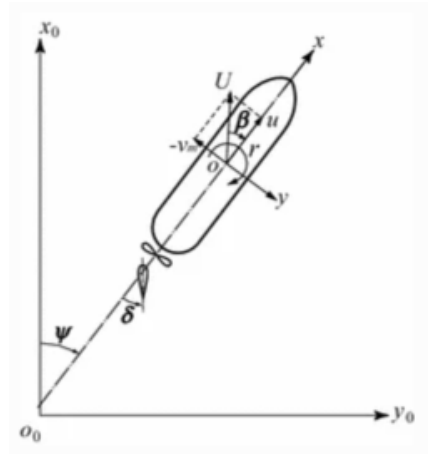


Figure 2.4: The coordinate system of Yasukawa and Yoshimura (2015).

While the manoeuvring equations are relatively easy to obtain and use, the challenge in calculating the drift induced force is related to the correct estimation of hydrodynamic derivatives. The values relevant for Equation (2.49) to (2.52), obtained from model tests of a bulk carrier with $L/B = 5.8$, $B/T = 2.6$ and $C_B = 0.8$, may be found in Fujiwara, Hearn, Kitamura, Ueno, and Minami (2005). Other methods to predict the derivatives are circular motion tests and planar motion mechanism. In the work of Sukas et al. (2019), which uses the complete force and moment formulations of Yasukawa and Yoshimura (2015), a wide range of empirical formulae from various researchers are given. Another option is to calculate the derivatives using CFD (Kramer and Steen, 2021).

Tillig and Ringsberg (2020) argued that other methods than manoeuvring equations provide a better solution for analysing a static sailing condition of a wind assisted ship. With the requirements of fast predictions, methods like CFD is not an option. Instead, Tillig and Ringsberg (2020) applied theoretical methods using only the main parameters of the hull; low aspect wing theory and a cross flow drag. These forces are thus subject to the flow oriented coordinate system, unlike the surge and sway forces of manoeuvring theory. In the following, the coefficients discussed are obtained by normalising the corresponding forces as the manoeuvring standard, Equation (2.47).

Low aspect ratio wing theory is applicable to conventional ships because these have aspect ratios (AR) well below the definition of $AR < 3$ (Hoerner, 1975). The AR of a ship is the ratio of the draught and length,

$$AR = \frac{T}{L_{PP}}. \quad (2.54)$$

A restriction to the applicability is connected to the drift angle. The angle must be such that there is circulatory lift. The maximum allowable drift angle is estimated to around $20^\circ - 40^\circ$, which is much higher than reasonable static drift angles for ships. The inability of the low aspect wing theory to capture the effect of a wave pattern on the drag and lift poses a limitation to the model. However, this might not be crucial as Kramer and Steen (2015) found the free surface to be of little importance for the drift induced forces, at least for Froude numbers that are normal for cargo ships. This is also indicated by the experimental results of Kramer et al. (2016b), although the study emphasise that more tests should be performed to validate it as a general phenomenon. Of course, whether the associated error is acceptable is dependent upon the situation and study where it is applied. The applied lift coefficient in Tillig and Ringsberg (2020) is the sum of a linear part and a non-linear one, according to Hoerner (1975),

$$C_L = C_{L,1} + C_{L,2}, \quad (2.55)$$

where

$$C_{L,1} = \left(1 + \frac{\Delta s}{s}\right)^2 \frac{\pi}{2} \cdot AR \cdot \sin \beta, \quad (2.56)$$

$$C_{L,2} = k' \cdot \sin |\beta| \sin \beta \cos \beta. \quad (2.57)$$

The linear part is low aspect theory but includes a factor $\left(1 + \frac{\Delta s}{s}\right)$ that represents the decrease of the aspect ratio due to rounded edges. Reasonable values are given in Hoerner (1975), depending on the planform and lateral edges of the foil. The non-linear term include the component of the cross-flow drag that is normal to the inflow direction. k' is the cross-flow coefficient. The bilge radius is commonly argued to be important for the cross-flow drag coefficient (Faltinsen, 1993; Kramer et al., 2016b). However, Tillig and Ringsberg (2020) could not detect a clear correlation for k' on the block coefficient, C_B , nor a dependency on other typical hull parameters. The

conclusion that the cross-flow drag coefficient is highly dependent upon local hull form features is supported by the discussion of van der Kolk (2016).

Similar to the lift force, the drag is also composed of a linear and non-linear part,

$$C_{Di} = C_{Di,1} + C_{Di,2}, \quad (2.58)$$

where

$$C_{Di,1} = C_{L,1} |\beta|^{0.6} \cdot a, \quad (2.59)$$

$$C_{Di,2} = k' \cdot \sin^3 |\beta|. \quad (2.60)$$

The first term is proportional to the drift angle, β , to the power of 0.6. The power of 0.6 was found to be a good fit for the sample ships so that the factor a was in fact nearly constant for each ship hull type over the drift angle (Tillig and Ringsberg, 2020). The ship geometry influence on this constant was not fully determined, but an increasing value with increasing block, midship or prismatic coefficient was mentioned. A dependency on the residual resistance coefficient was also investigated, in an attempt to include the effect of wave pattern. However, no clear dependency was reported. The second term in Equation (2.58), i.e Equation (2.60), is the part of the cross-flow term that is parallel to the inflow direction.

Chapter 3

Aerodynamics and modelling of sail systems

This chapter describes the general aerodynamic theory of two common sail systems, the Flettner rotor and rigid wingsail. See Figure 3.1 for reference. These particular systems are chosen because of their promising future in wind assisted ship propulsion. Both systems are commercially available, and while the Flettner rotor may be the most mature system today, there are several examples of promising wingsail projects. Another reason for the choice is that most of the research and published paper on wind assisted ship propulsion focus on these two systems. Furthermore, a short review of interaction effects is given in this chapter. However, the subject has not been much weighted as the sail model created for this thesis (see chapter 4) does not include such effects.

The theory of this chapter was reviewed for the work of the project thesis leading up to this master thesis. While the project thesis focused on the physical processes and details regarding the aerodynamics, the text presented in this chapter has been re-processed and shortened such that the relevant theory and equations are known prior to the implementation in chapter 4. The exception is the dynamic lift in section 3.2.3, a concept which was not included in the project thesis.

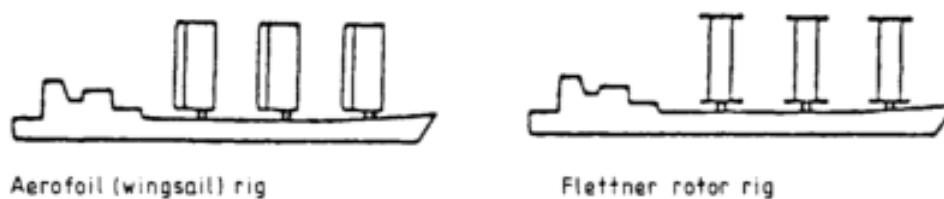


Figure 3.1: Idea sketch of the sail systems (Clayton, 1987)

3.1 Flettner rotor

The Flettner rotor is a rotating cylinder that uses the Magnus effect to generate aerodynamic lift. The device is named after its inventor Anton Flettner. In 1924, he developed a ship fitted with two rotor sails, shown in Figure 3.2. The development was done with assistance from Albert Betz, Jakob Ackeret and Ludwig Prandtl. Today, several ships are operated with the assistance from Flettner rotors, like the tanker *Timberwolf* (previously *Maersk Pelican*) or passenger vessel *Viking Grace* (Norsepower, 2020a). Unlike other sail technologies, the Flettner rotor is an active rotating device, such that it requires power to be operated.

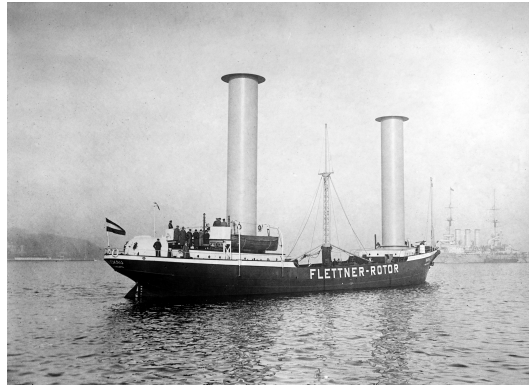


Figure 3.2: The *Buckau* photographed in 1924. (Available from the United States Library of Congress's Prints and Photographs division under the digital ID ggbain.37765)

The Magnus effect is the superposition of a uniform flow and a circulatory flow, illustrated in Figure 3.3. The circulatory velocity, U_c works either in favour or against the tangential velocity around the cylinder surface, U_e . This creates an unsymmetrical velocity and pressure field, which along with the change in momentum, generates the lift. Equation (3.1) describes the total force per unit span and is commonly known as Kutta Joukowski's law:

For any two-dimensional body moving with a constant velocity in an unbound inviscid fluid, the hydrodynamic pressure force is directed normal to the velocity vector and is equal to the product of the fluid density, body velocity and the circulation about the body (Newman, 2018).

$$L = \rho U_0 \Gamma. \quad (3.1)$$

Because the circulation is produced by the cylinder's rotation, it can be shown that the theoretical lift coefficient is dependent upon the ratio of the rotational velocity and the inflow velocity of the undisturbed flow,

$$C_L = 2\pi \frac{U_c}{U_0}. \quad (3.2)$$

The ability to consider the circulatory velocity equal to the rotational velocity requires the no-slip condition. In practical use, the velocity ratio is commonly known as the spin ratio, SR, Equation (3.3). It is the ratio of the local tangential velocity, v_t , and the local apparent wind velocity, v_A ,

$$\text{SR} = \frac{v_t}{v_A} = \frac{\Omega \frac{1}{2}d}{v_A}, \quad (3.3)$$

where Ω is the rotor's angular velocity and d is the diameter of it. What can be deduced from the above relationships is the inherent characteristic of a Flettner rotor being so-called storm

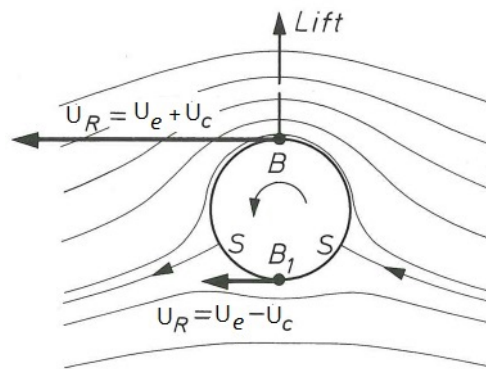


Figure 3.3: The Magnus effect (Marchaj, 2000).

proof. With an increasing apparent wind speed, the velocity ratio and obtainable lift is limited by the maximum rotational velocity of the rotor.

3.1.1 Viscous effects and three-dimensional flow

The obtainable lift coefficient is lower than the ideal coefficient due to viscous effects and the three-dimensional flow. The effects are present in several forms. Firstly, the pressure difference described by the Magnus effect, causing the lift generation, is not preserved when the rotor is three-dimensional with a finite end. Due to the air flow over the end, the leak of pressure reduces the efficiency of the rotor as a lift-producing device. Thus, the lift coefficient decrease with the aspect ratio, as it moves further away from the ideal two-dimensional flow. The aspect ratio of a Flettner rotor is defined by the ratio of the height, H , and diameter,

$$AR = \frac{H}{d}. \quad (3.4)$$

To improve the loss, end plates are commonly used to create a flow closer to the two-dimensional one. Experiments show that the lift coefficient is dependent upon the ratio of the end disk diameter and rotor diameter, d_e/d .

Secondly, viscous effects and flow separation cause a wake behind the cylinder. This leads to the pressure field being unsymmetrical about an axis perpendicular to the inflow velocity as well. Thus, the rotor also produces a drag force directed parallel to the inflow. The total drag is a sum of this pressure drag and a viscous drag. In other words, the Reynolds number is an important parameter. However, the quantified importance is still under debate and research. Experimental work indicate that the lift coefficient is only affected by the Reynolds number in the critical flow region for velocity ratios below 2.5 (Bordogna et al., 2019). The drag coefficient on the other hand, is influenced by the Reynolds number over the entire range of flow conditions for velocity ratios between 1 and 2.5.

3.1.2 Experimental data

Due to the previously mentioned effects which cannot be mathematically formulated, the Flettner rotor has been subject to many experimental tests to test various influencing parameters. The testing ranges back to when the rotor sail technology was developed and continues to recent studies like the work of Bordogna (2020). Today, full scale measurements of existing wind assisted vessels also exist, but the availability is often limited due to confidentiality. Either way,

there are many sources that formulate empirical expressions for the lift and drag coefficients. One example is those of Tillig (2020), which also include the power coefficient describing the required input power, P_{rotor} , to the Flettner rotor. The expressions are fitted to match full scale measurements from a cruise ferry with a single Flettner rotor of 24 m height and 4 m diameter. Expressed as functions of the rotor spin ratio, they are valid for rotors of $AR = 6$ and $d_e/d = 2$,

$$C_L = -0.0046 \cdot SR^5 + 0.1145 \cdot SR^4 - 0.9817 \cdot SR^3 + 3.1309 \cdot SR^2 - 0.1039 \cdot SR, \quad (3.5)$$

$$C_D = -0.0017 \cdot SR^5 + 0.0464 \cdot SR^4 - 0.4424 \cdot SR^3 + 1.7243 \cdot SR^2 - 1.641 \cdot SR + 0.6375, \quad (3.6)$$

$$C_P = 0.0001 \cdot SR^5 - 0.0004 \cdot SR^4 + 0.0143 \cdot SR^3 - 0.0168 \cdot SR^2 + 0.0234 \cdot SR. \quad (3.7)$$

The force coefficients are defined by Equation (3.8) and the power coefficient by Equation (3.9),

$$C_{L,D} = \frac{L, D}{\frac{1}{2} \rho_a \cdot A_p \cdot V_A^2}, \quad (3.8)$$

$$C_P = \frac{P_{\text{rotor}}}{\frac{1}{2} \rho_a \cdot A_p \cdot V_A^3}, \quad (3.9)$$

where ρ_a is the air density, A_p is the projected area of the sail and V_A is the apparent velocity of the wind.

Comparison of the full scale measurements and the fitted expressions to model test results show deviations and could possibly support the reported scale effects of Bordogna et al. (2019). The larger lift coefficients of Tillig (2020) and full scale measurements compared to model tests could be due to the influence of the Reynolds number.

3.2 Rigid wingsail

Rigid wingsails, analogous to airplane wings, are vertically aligned lifting surfaces that generate lift by the principles of foil theory. A proposed concept utilising this technology, the Oceanbird, is shown in Figure 3.4. The main geometry of such a sail is described by the span/height and chord length. Although most of the projects involving rigid wingsails today are still in the design stage, like the Swedish wPCC project which presented the Oceanbird (Wallenius Marine, 2020) and the British Windship system (Windship Technology, 2020), they represent promising concepts. Because of the need to generate lift from both port and starboard wind, the cross section of wingsails are generally symmetric foil profiles, with or without high-lift devices such as flaps.



Figure 3.4: The Oceanbird concept (Wallenius Marine, 2020).

The lift force acting on a foil section arises due to the pressure distribution along the chord on both sides of the foil. The potential flow around a foil is described by the superposition of a uniform flow and a circulatory flow. The circulation is sufficient to move the stagnation point to the trailing edge, such that the flow leaves the edge in a smooth and tangential manner, known as the Kutta condition (Newman, 2018). See Figure 3.5 for reference. Kelvin’s theorem states that the circulation is constant about any material contour containing the same fluid particles, which must be zero if the fluid started from a straight inflow. The contour must therefore surround the foil and a portion of its wake where the circulation is zero. This means that the circulation around the foil is cancelled by an equal and opposite starting vortex shed from the trailing edge during the initial acceleration. However, this vortex is usually neglected in a steady state problem, as it is far downstream of the foil. The lift per unit span of the foil, integrated from pressure distribution, is described by Kutta Joukowski’s law, Equation (3.1).

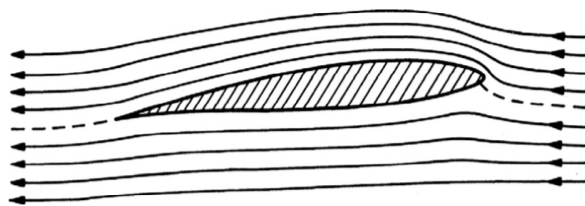


Figure 3.5: Potential flow around a foil (Newman, 2018)

3.2.1 Linear foil theory

Thin foils can quite accurately be described by linear foil theory. The theory assumes that the maximum thickness of the foil is small relative to the chord length, the angle of attack is small and the camber-to-chord ratio is small (Steen, 2014). The resulting flow is free of separation, viscous effects are confined to a thin boundary layer and the relationship between lift and angle of attack is linear. A great advantage of the linear foil theory is that the problem can be split into two separate problems that are later superposed. These are the lifting problem and the thickness problem. Literature like Abbott and von Doenhoff (1959) give tabulated data of lift, pressure and camber distribution of a large collection of foil profiles. These can be used to determine the thickness, camber and angle of attack contributions. An analytical approach to the lift coefficient is also possible, and for the simple case of a flat plate or uncambered foil, the expression is,

$$C_L^{2D} = 2\pi\alpha, \quad (3.10)$$

where α is the angle of attack in radians. The lift coefficient of a cambered profile is described by the general Equation (3.11), where the coefficient at zero angle of attack, $C_L(0)$, includes the effect of the camber,

$$C_L^{2D}(\alpha) = C_L(0) + 2\pi\alpha. \quad (3.11)$$

The coefficients are defined according to the common Equation (3.8), but in a 2D context like this, the area must be replaced with the chord length, c .

3.2.2 Viscous effects and three-dimensional flow

The flow of a three-dimensional wing is subject to pressure leakages at the ends, which leads to vortex generation. The vortices cause so-called downwash, defined by the general form of Bio Savart’s law in three-dimensional space. It changes the effective incoming velocity, such that the downwash reduced lift is lower than the ideal two-dimensional one and the drag coefficient increases. The latter is commonly referred to as induced drag. Furthermore, the vortices induce

velocities in the surroundings. Although these are of minor significance for the wing in question, as they quickly reduce with the vortices' distance from the wing, they are of vital importance for surfaces downwind of the foil, like for instance other sails.

Closely related to the pressure leakages at the wing tip, the circulation varies along the span of the wing. Usually it reduces gradually towards the tip. Assuming an elliptical circulation distribution, the 3D corrected coefficients are functions of the sail AR, Equation (3.12) to (3.14). The lift is obtained from span-wise integration of the Kutta Joukowski's law, Equation (3.1), while the drag integration is an expression of the circulation and downwash.

$$C_L = \frac{C_L^{2D}}{1 + 2/AR}, \quad (3.12)$$

$$C_{Di} = \frac{C_L^2}{\pi AR}, \quad (3.13)$$

$$C_D = C_{Dv} + C_{Di}, \quad (3.14)$$

where *i* and *v* denoted the induced and viscous drag components, respectively. The AR of a wingsail is defined as the area-to-span ratio, which for a rectangular shape (taper ratio of 1) equals the height-to-chord ratio,

$$AR = \frac{H}{c}. \quad (3.15)$$

For infinitely long wings, $AR = \infty$, the 3D lift coefficient reduces to the 2D one. The two-dimensional theory holds for infinitely long wings and can provide a good approximation for sections along the span. If the root of the wing is mounted on a surface, a mirror effect will cause the effective AR to be larger than the geometrical AR by a multiplication factor. The theoretical maximum factor of 2 is difficult to achieve in reality, and the obtainable increase is dependent upon the air flow disturbance from the deck and the gap between the wing root and the deck (Marchaj, 2000).

For other circulation distributions than the elliptical, the induced angle increases and the lift coefficient decreases. Equation (3.12) and (3.13) can be corrected with an planform efficiency *e*,

$$C_L = \frac{C_L^{2D}}{1 + \frac{2}{e \cdot AR}}, \quad (3.16)$$

$$C_{Di} = \frac{C_L^2}{\pi e \cdot AR}. \quad (3.17)$$

Naturally, the planform efficiency is 1 for the elliptical distribution and < 1 for all others.

The linear relationship between the lift coefficient and angle of attack is an accurate description until the angle of attack approaches a value where the foil is said to "stall". In this condition, the separation point is moved upstream to the upper side of the foil and the flow is far from smooth around it. The lift is drastically reduced while the drag increases, exemplified in Figure 3.6 for the NACA 0012 foil. Note that these lift and drag coefficients are two-dimensional.

3.2.3 Unsteady lift

Two main causes of unsteady effects of a foil are included in this section. The first one is a step change in angle of attack, which is described in the first paragraph of this section. The second one is the dynamic lift due to a harmonically oscillating foil.

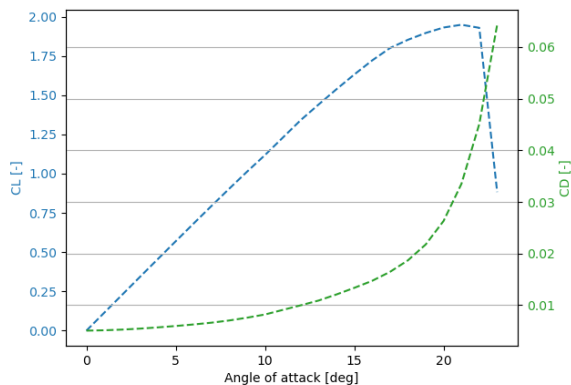


Figure 3.6: Lift and drag coefficients of NACA 0012 foil. The graph is generated from XFOIL data.

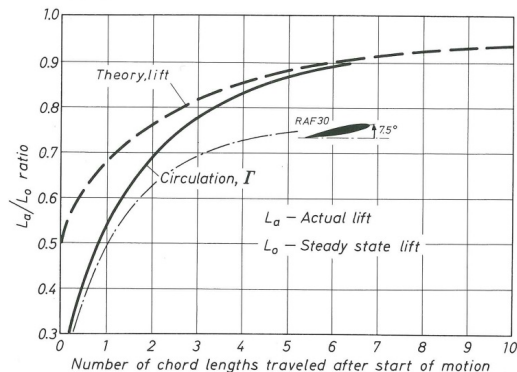


Figure 3.7: Lift and circulation development in time due to a sudden change in angle of attack (Marchaj, 2000).

A step change in the angle of attack causes the foil to experience a lift development in time. As mentioned earlier, the a starting vortex is shed during the establishment of the circulation. Due to the fluid mass that must be accelerated against inertia forces, there is a time lag connected to the circulation pattern development around a foil (Marchaj, 2000). The growth rate of lift and circulation with respect to the number of chord lengths travelled is known as the Wagner effect, Figure 3.7. The steady state magnitude is never fully reached, but approaches it asymptotically. The circulation development is indicated by the solid line and the actual lift from experimental results of a RAF 30 foil is marked with the thin broken line. The experimental results show that the nature of lift development is correct but the exact shape deviates from the theoretical.

Dynamic stall is the situation where a foil with a continuously changing angle of attack at some point passes the static stalling angle (Böckmann, 2015). The lift, drag and moment do not follow their static curves. The phenomenon is characterised by a vortex build-up at the leading edge which detaches and is spread downstream in the wake. The flow over the entire foil upper surface is separated when the vortex passes the trailing edge. When the angle of attack is again smaller, the flow reattaches to the front. The vortex build-up at the leading edge leads to an increased lift and an increase in nose-down pitching moment. The maximum dynamic value becomes significantly higher than the static equivalent. The peak is observed when the vortex passes into the wake before it drops.

A well known analytical expression of the unsteady lift of a two-dimensional flat plate in harmonic oscillation is the Theodorsen function. It assumes inviscid and incompressible fluid and small transverse motion, such that the shed vortices are assumed to remain in a straight line. Details on the physics and mathematical derivation are beyond the scope of this thesis. The main result of the analysis is that the unsteady lift can be written as the sum two terms. The first one is the non-circulatory term due to flow acceleration, i.e. added mass. The second is a quasi-steady term due to circulation about the plate, which is multiplied with the Theodorsen function $C(k)$,

$$C(k) = F(k) + iG(k) = \frac{H_1^{(2)}(k)}{H_1^{(2)}(k) + iH_0^{(2)}(k)}, \quad (3.18)$$

where $H_n^{(2)}(k)$ are the Hankel functions given by the Bessel functions of the first and second kind (Newman, 2018),

$$H_n^{(2)}(k) = J_n(k) - iY_n(k). \quad (3.19)$$

The variable k is the reduced frequency, given by the inflow velocity U_0 and chord length,

$$k = \frac{\omega c}{2U_0}. \quad (3.20)$$

From Equation (3.18), one can see that $C(k)$ consists of a real and imaginary part. The function is plotted in Figure 3.8.

Thus, for the simplest case of unsteady motion, a sinusoidal time dependence, the memory effects of the wake can be expressed as frequency-dependent force coefficients proportional to the ratio of the Hankel functions, i.e. the Theodorsen function (Newman, 2018). With reference to Figure 3.8, the Theodorsen function is 1 at low frequencies, such that the lift reduces to its quasi-steady state value. At other frequencies, it represents a reduction in lift amplitude and a force phase shift.

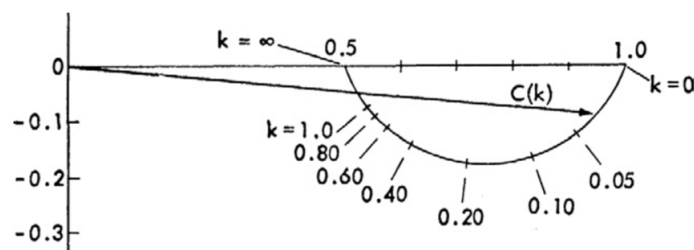


Figure 3.8: The Theodorsen function, Equation (3.18). The figure is from Bishop et al. (1972) in Newman (2018).

3.3 Interaction effects between multiple sails

When several sails are mounted close to each other, it is obvious that the flow field experienced by one is affected by the presence of the others. The effect is most prominent in the generated thrust and the changed centre of effort of the aerodynamic side force.

The effect can be divided into a potential and a viscous part (Tillig and Ringsberg, 2020). The former include the circulatory effect on the flow velocity, which can be predicted by Biot Savart's law with circulation obtained from an iterative approach with the Kutta Joukowski's law and a known lift coefficient. The viscous part consist of the wake behind the sail and turbulence from flow separation. In the horizontal plane, the vortices follow the potential streamlines. It is more difficult to predict their height and diameter in the vertical plane, requiring CFD, three-dimensional potential theory or flow measurements.

Many studies have been conducted on the interaction effects between sails (Bordogna, 2020; Fujiwara, Hearn, Kitamura, and Ueno, 2005). Experiments with Flettner rotors detect two main phenomena; the change of incoming wind speed and deflection of the incoming flow angle. The velocity change is dependent upon the spin ratio, and higher ratios can potentially increase the wind velocity compared to the undisturbed free stream velocity. Simultaneously, the downwash is increased with an increasing ratio, which affects the inflow angle. While the general phenomenon is reduced thrust, it has also been shown that optimising the sail arrangement and operation can reduce the thrust loss and in some cases increase the performance.

Chapter 4

The aerodynamic sail model

This chapter explains the implementation of the aerodynamic theory described in chapter 3, and the assumptions upon which the model is based. The model is coded in Python to calculate the aerodynamic damping from rigid wingsails and Flettner rotors. An algorithm of the code is given in section 4.6, while the code itself is found in Appendix A.

4.1 Coordinate system definitions

Although this chapter concerns the aerodynamic model, it is highly coupled with the hydrodynamic model of the ship. A definition of the reference frames of both are therefore required before further discussing the aerodynamic model. See Figure 4.1 for reference. In seakeeping theory, the reference frame is fixed to an equilibrium state, not the ship. It is inertial, i.e. non-accelerating and fixed in orientation with respect to the Earth-fixed reference frame. A constant heading and speed define the equilibrium state. The first coordinate system (X, Y, Z) is such a flow-fixed inertial system. The ship moves with a ship velocity V_S in the X -direction. The second coordinate system is a ship-fixed (x, y, z) . It is used to describe the rigid body motions, it is fixed to the mean position of the body and moves with the ship speed. The origin of both coordinate systems is at the undisturbed free-surface and they are right-handed systems, such that the vertical axes are directed upwards through the body centre of gravity. The angle between them is the drift angle β , defined positive in the clockwise direction. β is exaggerated in Figure 4.1 for illustrative purposes.

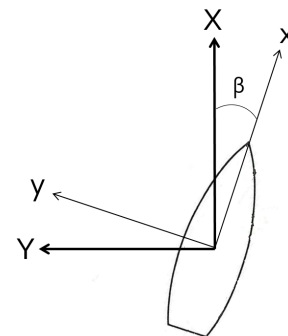


Figure 4.1: Defined coordinate systems.

The aerodynamic model can be divided into the wind model, described in section 4.3, and the sail models, described in section 4.4 and 4.5. The wind model is subject to the flow-fixed (X, Y, Z) coordinate system, while the sail models use both systems. The sails are the connection between the wind and ship model, which means that they transform the forces in the flow fixed coordinate system to the ship-fixed.

4.2 Assumptions and governing equations

The main assumptions of the aerodynamic model are listed below. Some of these are actually assumptions regarding the wind assisted ship model. However, due to their importance in the aerodynamic model, they require mention here.

1. The air is assumed homogeneous and incompressible and the flow is potential everywhere except for in the boundary layer and wake regions. The density is 1.21 kg/m^3 (Steen and Minsaas, 2014)
2. The true wind velocity and direction is steady, i.e. turbulence is neglected, but the wind varies in height due to the atmospheric boundary layer.
3. The sailing problem is known, meaning the ship is sailing with a constant ship speed V_S at a small drift angle β . The drift angle is small enough to neglect its effect on the hydrodynamic problem, except for the induced resistance.
4. Small mean angles of heel and trim may be present but does not affect the analysis, such that the sail is considered vertical at all times.
5. Ship motions induce small harmonic perturbations off the steady flow, such that separate modes can be superposed. The centre of body motions is situated on the still water surface. While the centre usually moves from the water line to the centre of mass when a motion goes from being stiffness to inertia dominated, chapter 6 will show that these points coincide for the sample ship at design loading condition.
6. The sea state is steady and regular with incident wave frequency ω_0 .
7. The sail is positioned mid-centre of the ship at deck height equal to the ship freeboard.
8. Hull interference effects and interference effects between several sails are disregarded.
9. Dynamic lift due to oscillatory motion is disregarded.
10. The aerodynamic damping is linear.

Additional assumptions specific for a certain sail system are given in the corresponding section.

The six coupled equations of motions, Equation (2.13), reduce to two sets of equations for a ship with lateral symmetry (Faltinsen, 1993). These are the coupled equations in surge, heave and pitch and another set of coupled sway, roll and yaw. For simplicity, the aerodynamic model only considers the ship roll and pitch motion. The chosen degrees of freedom are of particular interest in a seakeeping analysis. Thus, from an hydrodynamic point of view, the roll and pitch motions are decoupled. However, the sail systems may induce moments leading to coupled degrees of freedom, as indicated by the work of Sinclair (1991). Hence, the sail model initially assumes the roll and pitch moments to be aerodynamically coupled. The importance of the coupling terms will be discussed.

The model is quasi-steady, i.e. the inertia terms of the sail forces are not included. The added mass contribution of sails are assumed to be small relative to the hydrodynamic contributions from the vessel. A rough estimate of roll added mass for a Flettner rotor can be calculated using a strip theory approach (Faltinsen, 1993; Newman, 2018) and integrating over the sail height

from the roll centre. The analytical two-dimensional added mass of a circle is (Newman, 2018),

$$A_{22}^{(2D)} = \rho \frac{\pi}{4} d^2. \quad (4.1)$$

The bottom and top of the sail are denoted z_b and z_t , respectively. The three-dimensional roll added mass estimate is thus,

$$A_{44} = \int_{z_b}^{z_t} z^2 A_{22}^{(2D)}(z) dz \quad (4.2)$$

$$= \left[\frac{1}{3} z_t^3 - \frac{1}{3} z_b^3 \right] \cdot \rho_a \frac{\pi}{4} d^2 \quad (4.3)$$

$$= \frac{\pi}{12} \rho_a d^2 [z_t^3 - z_b^3] \quad (4.4)$$

$$= \frac{\pi}{12} 1.21 \text{ kg/m}^3 \cdot (5 \text{ m})^2 [42.5 \text{ m}^3 - 12.5 \text{ m}^3] \quad (4.5)$$

$$\approx 6 \cdot 10^5 \text{ kg m}^2 \quad (4.6)$$

From Equation (4.2) to (4.3), the integration is performed with $A_{22}^{(2D)}(z) = A_{22}^{(2D)}$, because the rotor diameter is constant. The estimate, Equation (4.5), is based on a rotor height and diameter of 30 m and 5 m, respectively. According to assumption 5 above, the roll centre is situated at the still water surface, such that the integration limits are dependent upon the freeboard, f , of the ship,

$$z_b = f = 12.5 \text{ m}, \quad (4.7)$$

$$z_t = H + f = 30 \text{ m} + 12.5 \text{ m} = 42.5 \text{ m}. \quad (4.8)$$

The value of the freeboard is chosen based on the sample ship in this work, which will be explained in chapter 6. Assuming the sail is surrounded by infinite air, the pitch and roll added mass terms are equal, $A_{55} = A_{44}$.

According to Newman (2018), the two-dimensional added mass of a flat plate for motion normal to the plate is equal to the displaced mass of the circumscribed circle. Thus, Equation (4.1) is applicable to a plate with the length equal to d . The worst case scenario added mass of a wingsail may therefore be based on Equation (4.4) with $d = c$. If the chord is 10 m and one assumes a wingsail of equal height as the Flettner rotor, A_{44} and A_{55} of the wingsail are approximately $2 \cdot 10^6 \text{ kg m}^2$.

The rough estimates show that the added mass terms due to the sail geometries are much smaller than the hydrodynamic equivalents of a large cargo or passenger ship. The hydrodynamic roll added mass of the sample ship, section 6.1.1, is around the order of 10^9 in roll and even larger in pitch. The maximum added mass, that of the wingsail, is 0.2% of the hydrodynamic roll added mass. The dimensions and number of sail would have to be increased beyond reasonable for it to be significant. Thus, the aerodynamic added masses are negligible. Furthermore, the excitation loads induced by sails are neglected because previous work indicate that the effect of Flettner rotors could only be noticed as a constant external heeling force in roll motion (Copuroglu and Pesman, 2018).

To summarise, the governing equations of motion of the problem are stated in Equation (4.9) and (4.10). The superscript aero denote the aerodynamic coefficients, while all other are hydrodynamic coefficients.

$$(I_{44} + A_{44})\ddot{\eta}_4 + (B_{44} + B_{44}^{\text{aero}})\dot{\eta}_4 + B_{45}^{\text{aero}}\dot{\eta}_5 + C_{44}\eta_4 = F_4, \quad (4.9)$$

$$(I_{55} + A_{55})\ddot{\eta}_5 + B_{54}^{\text{aero}}\dot{\eta}_4 + (B_{55} + B_{55}^{\text{aero}})\dot{\eta}_5 + C_{55}\eta_5 = F_5, \quad (4.10)$$

with assumed corresponding harmonic motions which follow from Equation (2.10),

$$\eta_4 = \eta_{4a} \cos(\omega_e t + \delta_4), \quad (4.11)$$

$$\eta_5 = \eta_{5a} \cos(\omega_e t + \delta_5). \quad (4.12)$$

According to Equation (2.9), the horizontal motion and velocities of the sail in the (x, y) plane, are functions of the height z from the centre of motions. The expressions are reduced compared to Equation (2.9), as only roll and pitch motions are considered,

$$s_1 = z\eta_5, \quad (4.13)$$

$$s_2 = -z\eta_4, \quad (4.14)$$

$$\dot{s}_1 = z\dot{\eta}_5, \quad (4.15)$$

$$\dot{s}_2 = -z\dot{\eta}_4. \quad (4.16)$$

Due to assumption 5 and 7, the point z of a sail section is the sum of the height of that section, h, and the ship freeboard,

$$z = h + f. \quad (4.17)$$

Due to linearity, the damping terms are calculated by forced oscillation in each degree of freedom. Throughout this and following chapters, the term *mode* is used in relation to the Python calculations and refers to the forced motions. If roll mode is initialised in the code, Equations (4.9), (4.11), (4.14) and (4.16) are governing equations. In pitch mode, these are Equations (4.10), (4.12), (4.13) and (4.15). The resulting aerodynamic moment j due to the forced rigid body motion (mode) k is assumed to be expressed by a harmonic function such that it is linear and proportional to the rigid body motion,

$$F_{jk}^{\text{aero}} = A_{jk}^{\text{aero}} \sin(\omega_e t + \epsilon_k) + D_{jk}^{\text{aero}}. \quad (4.18)$$

A_{jk}^{aero} is the amplitude of the moment and is given the superscript *aero* to avoid confusion with the wave amplitude in irregular sea, Equation (2.1), or the hydrodynamic added mass of Equation (4.9) and (4.10). D_{jk}^{aero} is the constant moment. The damping coefficient is thereafter calculated as,

$$F_{jk}^{\text{aero}} = \frac{A_{jk}^{\text{aero}}}{\omega_e \eta_{ka}} \cdot \omega_e \eta_{ka} \sin(\omega_e t + \epsilon_k) + D_{jk}^{\text{aero}} \quad (4.19)$$

$$= -\frac{A_{jk}^{\text{aero}}}{\omega_e \eta_{ja}} \dot{\eta}_k + D_{jk}^{\text{aero}} \quad (4.20)$$

$$= -B_{jk}^{\text{aero}} \dot{\eta}_k + D_{jk}^{\text{aero}}, \quad (4.21)$$

where the response velocity in Equation (4.20) follows from Equation (2.10). The above derivation leads to the definition of the aerodynamic damping coefficients of Equation (4.9) and (4.10),

$$B_{jk}^{\text{aero}} = \frac{A_{jk}^{\text{aero}}}{\omega_e \eta_{ka}} \quad j, k = 4, 5 \quad (4.22)$$

The constant damping moment D_{jk}^{aero} leads to a constant heeling or trim angle of the ship, but it is not further considered in the analysis due to assumption 4. It is the seakeeping characteristics which are of interest in this model, not the hydrostatics.

4.3 Wind model

The wind experienced by the sails while the ship is sailing, the apparent wind, is different from the true wind. The apparent wind is dependent upon the ship forward velocity and sail horizontal velocities. As mentioned, the wind is subject to the flow-fixed (X, Y, Z) reference frame but is assumed to be in the horizontal (X, Y) plane.

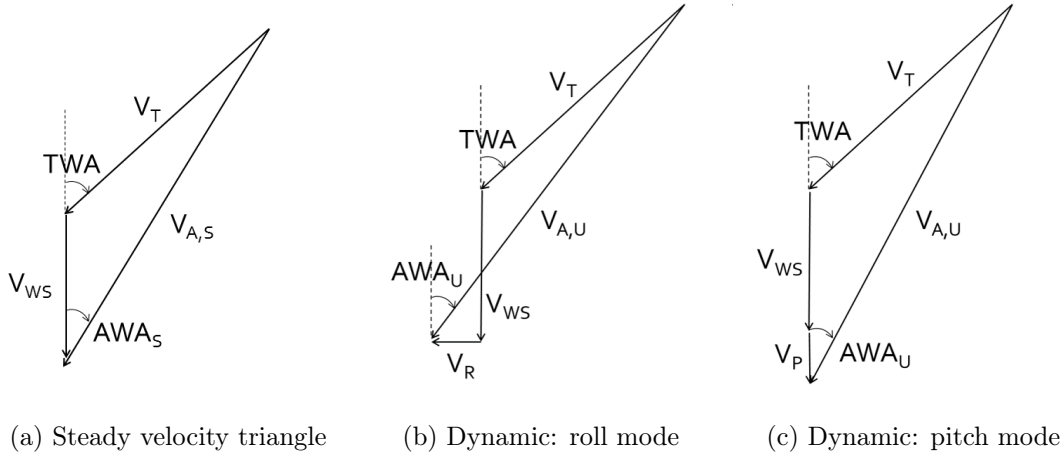


Figure 4.2: The steady and dynamic wind velocity triangles, subject to the (X, Y, Z) reference frame. V_{wS} and V_P are drawn as negative values.

The model includes the wind components shown in the velocity triangles of Figure 4.2. Figure 4.2a is the steady velocity triangle when neglecting rigid body motions, commonly known from literature on wind assisted propulsion. The subscript S refer to steady. Due to the rigid body motion, the instantaneous wind varies like a perturbation off the steady apparent wind. This gives rise to the unsteady terms, which are given the subscript U in Figure 4.2b and 4.2c. The following list explains the wind velocity components.

- **True wind velocity**, V_T , or true wind speed (TWS) is always of positive value and the direction is defined by the true wind angle (TWA). TWA is defined as zero when the wind is directed along the negative X-direction, i.e. in opposite direction of the ship velocity. The angle is positive in the clockwise direction and the valid range is $[0, \pi]$. The TWS varies in the vertical direction due to the atmospheric boundary layer,

$$\text{TWS} = \text{TWS}_{10} \cdot \left(\frac{z}{10}\right)^a, \quad (4.23)$$

where a is the Hellmann coefficient and TWS_{10} is the true wind speed at reference height 10 m. The Hellmann coefficient used in the model is 0.11, which is appropriate for unstable air above a flat, open coast (Kaltschmitt et al., 2007).

- **Wind velocity due to ship velocity**, V_{wS} , along the X-axis,

$$V_{wS} = -V_S. \quad (4.24)$$

Because the ship is assumed to always sail in the positive X-direction, V_{wS} will always be a negative property.

- **Relative wind velocity due to ship roll motion**, V_R , along the Y-axis. This component is only included if roll mode is initialised in the damping model. The wind speed follows

from the transverse sail velocity, \dot{s}_2 of Equation (4.16), transformed to the flow-fixed Y-axis,

$$V_R = -\dot{s}_2 \cos \beta = z \cos \beta \cdot \dot{\eta}_4. \quad (4.25)$$

- **Relative wind velocity due to ship pitch motion**, V_P , along the X-axis. The component is only included if pitch mode is initialised. It follows from the longitudinal sail velocity, \dot{s}_1 of Equation (4.15), transformed to the flow fixed X-axis,

$$V_P = -\dot{s}_1 \cos \beta = -z \cos \beta \cdot \dot{\eta}_5. \quad (4.26)$$

Like the true wind, the apparent wind velocity, V_A , is always a positive scalar and its direction is defined by the apparent wind angle, AWA. Even though TWA is in the range $[0, \pi]$, the model operates with AWA in the range $[-\pi, \pi]$. This is a consequence of V_R , which may cause the apparent wind to cross the X-axis if the TWA is close to zero or π . Like for the TWA, AWA of zero means that the apparent wind is aligned with the X-axis, pointing in the negative X-direction. Positive values are clockwise. The apparent wind is computed from the geometry of the wind velocity triangle. In roll mode with reference to Figure 4.2b, the unsteady apparent wind is given by,

$$V_{A,U} = \sqrt{[-V_{wS} + V_T \cos(\text{TWA})]^2 + [V_T \sin(\text{TWA}) + V_R]^2}, \quad (4.27)$$

$$\text{AWA}_U = \arctan \left[\frac{V_T \sin(\text{TWA}) + V_R}{-V_{wS} + V_T \cos(\text{TWA})} \right], \quad \in [-\pi, \pi], \quad (4.28)$$

and in pitch mode with reference to Figure 4.2c, it is given by,

$$V_{A,U} = \sqrt{[-V_{wS} + V_T \cos(\text{TWA}) - V_P]^2 + [V_T \sin(\text{TWA})]^2}, \quad (4.29)$$

$$\text{AWA}_U = \arctan \left[\frac{V_T \sin(\text{TWA})}{-V_{wS} + V_T \cos(\text{TWA}) - V_P} \right], \quad \in [-\pi, \pi]. \quad (4.30)$$

The scalar of V_A is AWS (apparent wind speed). In the following sections, lower case letters will be used to indicate the local apparent wind speed and angle, aws and awa . These are functions of the sail section height, h , and the rigid body motion.

The atmospheric boundary layer causes the true wind speed to vary over the sail height, while the ship speed is constant. This leads to a significant wind twist and change in wind velocity over the sail. As an example, with TWS_{10} equal to 10 m/s, the $V_{A,S}$ differ with about 1.6 m/s over a 35 m tall sail, assuming the sail root is mounted at the ship freeboard of 12.5 m. The steady apparent wind angle is around 8 degrees. If the freeboard is lower, the speed and angle difference is greater due to the exponential form of the boundary layer, Equation (4.23). Additionally, the rigid body motions lead to even larger changes in the unsteady apparent wind. Thus, the wind twist and velocity gradient over the sail are also dependent upon parameters like encounter frequency and rigid body motion amplitude, in addition to the sail height and ship freeboard.

4.4 Flettner rotor model

Because the wind model is built to handle TWA in the range $[0, \pi]$, anticlockwise rotation of the rotor generates lift in the positive X-direction, see the blue area of Figure 4.3. This is defined as a positive spin ratio in the model. In the few cases where the local AWA on the rotor sections are in the range $[-\pi, 0]$ and the spin ratio is positive, the lift will act in the negative direction. Consequently, a negative spin ratio indicates that the Flettner rotor spins in the clockwise direction and generates negative thrust. The lift is perpendicular to the inflow but acts in the negative X-direction, i.e. the unmarked area in Figure 4.3. The drag is unaffected due to the definition of a drag force, it is always parallel to the flow direction.

The model uses the empirical expressions of lift, drag and power coefficients suggested by Tillig (2020), given in Equation (3.5), (3.6) and (3.7). They were chosen due to the easy implementation in a mathematical model. Because they originate from full scale measurements of a ship with Flettner rotors, they should be free of scale effects. Their implementation leads to the model being limited to rotors of AR 6. Furthermore, modifications of the lift and drag coefficients are done in order to ensure that they are applicable to the current physical model. Equation (3.5) and (3.6) are only valid for positive values of spin ratio, and judging from the full scale measurement data from which they arise, the valid range is up to SR 5–6. If the sail is set to act as a break in the current model, i.e. SR is negative per definition, the lift coefficient is calculated by the absolute value of SR and later corrected to its negative value. The sign is required to indicate which perpendicular direction off the wind velocity that the lift is directed. The direction of the drag force is unaffected and thus the drag coefficient is always calculated from the absolute value of the spin ratio. This is the first modification, or rather a modification of the usage. In other words,

$$C_L(\text{SR} < 0) = -C_L(|\text{SR}|), \quad (4.31)$$

$$C_D(\text{SR} < 0) = C_D(|\text{SR}|). \quad (4.32)$$

The second modification deals with the upper limit of SR. In the current configuration, the local SR at a particular sail section can be unreasonably large if AWS is small. This might for instance happen if the V_R is large in beam apparent wind. To correct for such cases, the lift and drag coefficient expressions are extrapolated from the point of SR equal to 6, see Figure 4.4. The lift coefficient is constant for increasing values of SR from 6, while the drag coefficient is linearly increasing based on linear extrapolation between SR 5 and 6. Although the drag extrapolation might not be physically correct, it models the penalty of an increasing SR leading to separation, which is a state that should normally be avoided in the operation of a Flettner rotor. The power coefficient of Equation (3.7) does not require any modifications due to its constant non-linear increase for all SR. Thus, the expression is used in its original form, and Equation (3.7) and the modification are equals in the bottom graph of Figure 4.4.

The model trims the rotor velocity based on a target SR, which is defined by the user. Further-

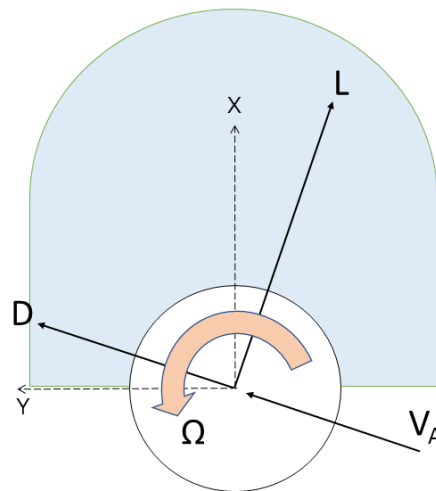


Figure 4.3: Definition of positive SR and lift force in the Flettner rotor model. The blue area marks the area of positive lift, i.e. towards the positive X-direction

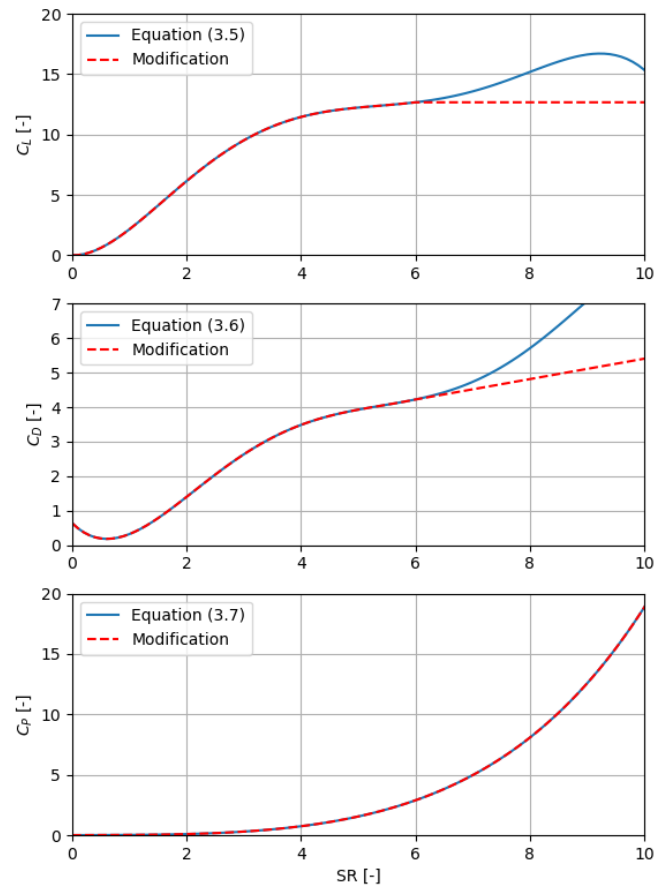


Figure 4.4: Empirical lift, drag and power coefficients of Tillig (2020) and their modifications used in the Flettner rotor model.

more, the sail is trimmed relative to the height- and time-averaged apparent wind velocity over the sail and encounter period. A more complex model could estimate the RPM based on an optimisation to maximise the total power of the rotor (i.e. thrust minus required input power). However, in the current analysis it was deemed interesting to test and investigate the effects of various sail loadings, as the amount of wind propulsion is expected to affect the damping characteristics. Thus, the rotational velocity of the rotor is,

$$\Omega = \frac{SR_{\text{target}} \cdot \overline{V_A}}{\frac{1}{2}d}. \quad (4.33)$$

The local SR along the sail is thereafter calculated according to Equation (3.3), based on the local apparent wind velocity at the particular sail height.

The lift and drag forces follow from the definition of the coefficients, Equation (3.8). However, the two-dimensional forces at a certain sail section, dL and dD , are based on the diameter of the rotor rather than the projected area of the entire sail,

$$dL = \frac{1}{2}\rho_a C_L V_A^2 d, \quad (4.34)$$

$$dD = \frac{1}{2}\rho_a C_D V_A^2 d. \quad (4.35)$$

As indicated by Equation (4.31), the lift coefficient can be either positive or negative depending on the SR. The lift force follows its sign, such that it is a mathematically positive value when directed in the positive X-directions. The drag is always positive since only the AWA is required to know its direction. The precise directions of the forces are accounted for in the driving and heeling forces, Equation (4.36) and (4.37), subject to the (X, Y) reference frame,

$$dF_D = dL \sin(AWA) - dD \cos(AWA), \quad (4.36)$$

$$dF_H = dL \cos(AWA) + dD \sin(AWA). \quad (4.37)$$

Finally, the roll and pitch moments are calculated from the sway and surge components, respectively, of the driving and heeling forces,

$$dF_4 = -dF_H z \cos \beta - dF_D z \sin \beta, \quad (4.38)$$

$$dF_5 = -dF_H z \sin \beta + dF_D z \cos \beta, \quad (4.39)$$

where z is the distance between the sail section and the roll or pitch motion centre, Equation (4.17). dF_4 and dF_5 are subject to the ship-fixed (x, y) reference frame. The negative signs in Equation (4.38) and (4.39) arise from the right hand rule, because a positive heeling force gives negative contributions to the roll and pitch moments. Equivalently, a positive driving force gives a negative contribution to roll, but a positive contribution to pitch. This is seen by studying Figure 4.1.

4.5 Wingsail model

The wingsail model is largely based on the demonstrated approach of Persson et al. (2019) named Sectional Integration with 3D-correction (SILL). It is based on a lifting line approach. Out of the tested simplified methods, Persson et al. (2019) concluded this method to provide the best sail force prediction up until angles close to stall. Considering its very easy implementation, it was deemed sufficiently accurate for this model and analysis.

The wingsail model assumes that the sail consists of a thin foil with zero camber, for instance the NACA 0012 profile. Thus, linear foil theory and Equation (3.10) is applied. As a simple approach, the viscous drag coefficient in 2D is assumed to be a fixed value. $C_{Dv} = 0.01$ is chosen as a rough estimate of the mean value in normal operating conditions according to Figure 3.6. These values are used within a range of angles of attack (AoA) below the assumed stalling angle. The implemented method to trim the sails and the corresponding AoA with force direction definitions require a more intricate explanation, see section 4.5.1.

With reference to the NACA 0012 foil, Figure 3.6, the stalling angle is set to 20° . The chosen value may be overpredicted, as a starting threshold of the stall can be observed at 15° . However, the exact point of stalling is not the most significant detail, as the model is simple in nature. In the overall sail damping model, the negative effect of stalling is captured this way, nevertheless. Thus, if the AoA exceeds the stalling angle, a high penalty viscous drag coefficient and low lift coefficient is assumed,

$$C_{L,\text{stall}} = 0.5, \quad (4.40)$$

$$C_{Dv,\text{stall}} = 2. \quad (4.41)$$

The value of the drag coefficient is based on the drag of a flat plate (Çengel and Cimbala, 2014) as an upper conservative penalty. The actual values chosen are not of great significance because the model focuses on the sail effects at angles below stall. It is not created to calculate the sail

forces during stalling. The important feature is to capture the low foil efficiency at stall, which is obtained with Equation (4.40) and (4.41).

Because the aerodynamic sail model does not take yaw motion into account, the wingsail moment is neglected. Three-dimensional effects are included by assuming an elliptical circulation, such that the lift coefficient is corrected and the induced and total drag is calculated according to Equation (3.12) to (3.14). Due to mirroring effects against the ship deck upon which the sail is mounted, the effective AR of Equation (3.12) could be increased by a factor from 1 to 2 compared to the geometrical AR. Because an accurate prediction requires more advanced methods like experiments or CFD, a conservative approach with a factor of 1 is used in this work. As for the Flettner rotor, the sectional lift and drag forces follow from Equation (4.34) and (4.35). Note that the foil chord is used for scaling instead of the rotor diameter as presented in the equations.

Mathematically, a positive lift force is directed in the positive X-direction and contributes to positive thrust, while a negative lift force is directed in the negative X-direction. Section 4.5.1 explains how the model handles this. The drag is always of positive value since the induced drag term is proportional to the square of the lift coefficient, Equation (3.13). This means that the driving force is calculated based on the absolute value of the AWA, Equation (4.42). The direction of the heeling force is dependent on the sign of the AWA, Equation (4.43),

$$F_D = L \sin |AWA| - D \cos |AWA| \quad (4.42)$$

$$F_H = \begin{cases} -L \cos |AWA| - D \sin |AWA| & , \text{ if } AWA \in [-\pi, 0] \\ L \cos (AWA) + D \sin (AWA) & , \text{ if } AWA \in [0, \pi] \end{cases} \quad (4.43)$$

Finally, the roll and pitch moments follow according to Equations (4.38) and (4.39).

4.5.1 Sail trim and local angle of attack

The wingsail is assumed to operate in a “stick fixed” mode, meaning the sail is trimmed to a fixed value during subsequent oscillations. It is analogous to a wind assisted ship sailing in a steady wind condition and trimming the sail to an appropriate fixed mode. If the steady wind condition changes to another steady condition, the sails can be trimmed to a new angle. However, during one model state, the sail trim is kept constant and the instantaneous angle of attack at different sail sections will vary due to the dynamic wind conditions. More structurally advanced wings can in principle be twisted, but this feature is not included in the current analysis due its rarity in existing projects with rigid wingsails and the increased modelling complexity.

To account for the varying wind inflow, Clayton and Sinclair (1988) suggested that the sail can be trimmed based on the theoretical maximum angle of attack variation, $d\alpha$, caused by the rigid body motion. The variation is the difference between the steady and unsteady apparent wind angle, Figure 4.5. Using the small angle approximation $\tan \alpha \approx \alpha$, it may be calculated according to,

$$|d\alpha| = \frac{V_{R,\max} \cdot \cos AWA_S}{V_{A,S}} \quad \text{roll mode,} \quad (4.44a)$$

$$|d\alpha| = \frac{V_{P,\max} \cdot \sin AWA_S}{V_{A,S}} \quad \text{pitch mode,} \quad (4.44b)$$

where the maximum motion induced velocities are calculated at the top of the sail. The trim should then aim to obtain an angle of attack,

$$\alpha_{\max} = \alpha_{\text{stall}} - |d\alpha| \quad (4.45)$$

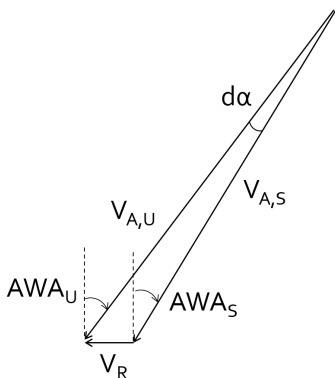


Figure 4.5: Variation of angle of attack in roll mode

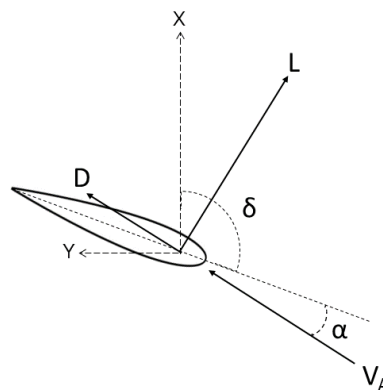


Figure 4.6: Wingsail trim for positive values of AWA

However, the current wingsail model trims the sail based on a target AoA, and the height- and time-averaged AWA experienced over an encounter period. The trim angle, δ ,

$$\delta = \overline{\text{AWA}} - \alpha_{\text{target}}. \quad (4.46)$$

Recall that the mathematical symbol of AoA is α . By trimming the sails relative to $\overline{\text{AWA}}$, the target AoA is obtained the most frequently. The target is defined by the user whom is free to choose any angle, but Equation (4.44) could be a good choice to avoid stalling. However, in a thrust perspective, it might be acceptable to risk foil stall and use a smaller incidence margin in some conditions, because the maximum roll velocities only represent a small portion of the roll period (Satchwell, 1986). Either way, like with the Flettner rotor and target SR, the ability to vary the target AoA is desirable so that the effect on sail damping can be studied.

With a known trim angle, the local AoA can be calculated from the local apparent wind angle, awa ,

$$\alpha = \text{awa} - \delta. \quad (4.47)$$

Recall that awa is dependent upon the sail section height and rigid body motion. In the model, a positive local AoA implies that the foil section is oriented such that the lift acts towards the positive X-direction. In other words, if awa is in the range $[0, \pi]$, the sail is trimmed in the anticlockwise direction relative to the apparent wind. The value of trim, Equation (4.46) is positive. This defines a positive AoA in Equation (4.47). The situation is illustrated in Figure 4.6. Consequently, a negative local AoA means that the lift acts towards the negative X-direction, generating negative thrust. In this case, the sail is trimmed in the clockwise direction relative to the apparent wind. The trim is still a positive value, but larger than the local apparent wind angle ($\delta > \text{awa}$), such that local AoA is negative in Equation (4.47).

Because the model assumes the rigid body motion to be a small perturbation off the steady flow, the mean apparent wind angle is assumed to always be in the range $[0, \pi]$. However, as mentioned in the description of the wind model, the roll mode can cause the local wind to cross the X-axis, such that awa is negative in the range $[-\pi, 0]$ at some sail sections. Two possible cases require different corrections:

- If $\text{awa} \in [-\frac{\pi}{2}, 0]$: an anticlockwise trim relative to the local apparent wind gives lift in the negative X-direction, as illustrated in Figure 4.7a. This case can occur in head wind if $\overline{\text{AWA}}$ is small and the target AoA is larger, such that the trim is negative, Equation (4.46).

The sign of the AoA must be corrected to the negative, such that the lift is negative in future calculations of Equation (3.10).

- If $\text{awa} \in [-\pi, -\frac{\pi}{2}]$: an anticlockwise trim relative to the local apparent wind gives lift in the negative X-direction. See Figure 4.7b. The trim is still of positive sign because $\overline{\text{AWA}}$ is large and approaching π . Because of the negatively directed lift, the sign of AoA must be corrected to the negative. Additionally, AoA must be shifted with 2π because Equation (4.47) gives $\alpha < -2\pi$, which is outside the defined valid range in the model.

For clarity, the corrections are summarised as follows:

- If: $-\frac{\pi}{2} < \text{awa}(h, \eta_4) < 0$ perform: $\alpha(h, \eta_4) = -\alpha(h, \eta_4)$
 If: $-\pi < \text{awa}(h, \eta_4) < -\frac{\pi}{2}$ perform: $\alpha(h, \eta_4) = -(2\pi + \alpha(h, \eta_4))$

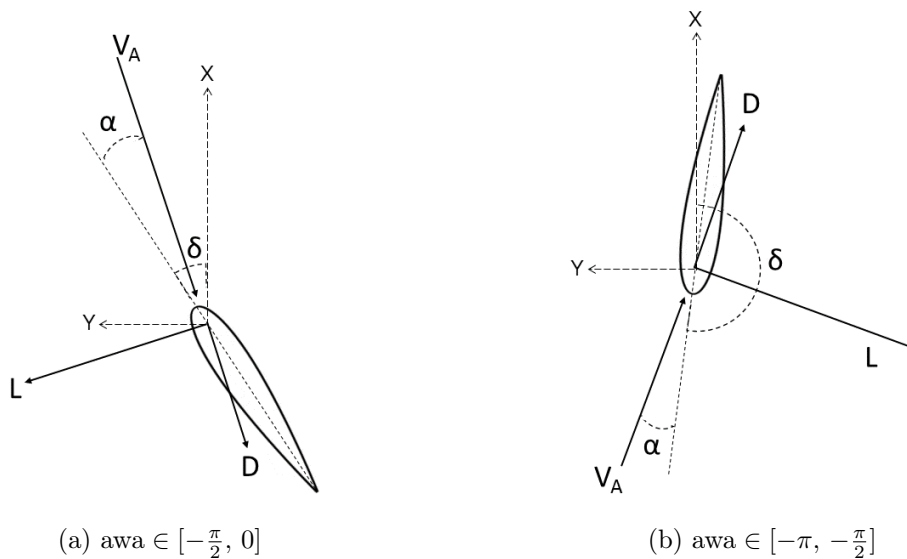


Figure 4.7: Wingsail trim for the two cases of negative AWA. The trim angle, AoA and drag are amplified for illustrative purposes.

4.6 Code algorithm

The required inputs to the code are: The specific sail system (Flettner rotor or wingsail), the relevant target sail trim ($\text{SR}_{\text{target}}$ [-] or α_{target} [deg]), true wind speed at reference height (TWS_{10}), ship velocity (V_S), rigid body motion (roll or pitch), whether or not to include wingsail stalling (which is ignored if the chosen sail system is the Flettner rotor), the incident wave frequency (ω_0) and whether or not to include the atmospheric boundary layer.

The descriptions of the Flettner rotor and wingsail model of section 4.4 and 4.5 are summarised in the code algorithm below. Only equations that apply to both the Flettner rotor and the wingsail are referred to in the list.

1. Import the ship model describing ship geometry and the known sailing problem: freeboard f , drift angle β . Calculate the encounter frequency ω_e and rigid body velocity $\dot{\eta}_k(t)$.
2. Import the sail geometry of the chosen sail system: height H , diameter d (Flettner rotor) or chord c (wingsail) and AR .
3. Discretise the sail into N sections along the height.

4. Calculate the wind speed at each section according to Equation (4.23), based on TWS_{10} and section height h .
5. At each section, perform the following:
 - (a) Calculate the properties of the apparent wind, Equation (4.27) to (4.30).
 - (b) Calculate the lift and drag coefficients. In case of the Flettner rotor, calculate the power coefficient.
 - (c) Calculate 2D lift and drag forces, and 2D power in case of Flettner rotor.
 - (d) Convert the lift and drag to driving and heeling forces.
 - (e) Calculate the roll and pitch moment, Equation (4.38) and (4.39).
6. Vertically integrate local roll and pitch moments using Simpson's rule to obtain total moments. In case of Flettner rotor, integrate the power to obtain total required input power.
7. Perform curve fit to data to express the roll and pitch moments as sinus functions.
8. Calculate the damping coefficient, Equation (4.22), from the moment term that is proportional to the rigid body velocity.

4.7 Convergence of sail discretisation

The sails are discretised in height and it must be validated that the discretisation is converged. The sail thrust coefficient is used as the parameter to monitor in the convergence check. A constant wave frequency, motion amplitude and TWA were chosen, based on reasonable values for the wind assisted ship. This will be discussed further in coming chapters and is not of significance in this particular section. The thrust force is normalised by the apparent wind speed at reference height and the sail projected area,

$$C_T = \frac{F_D}{\frac{1}{2}\rho_a AWS_{10}^2 A_p}. \quad (4.48)$$

If the thrust coefficient from the sail using i discretisations is denoted $C_{T,i}$ and the coefficient from $(i+1)$ discretisations is $C_{T,i+1}$, the relative change is calculated as

$$\Delta C_T = \left| \frac{C_{T,i} - C_{T,i+1}}{C_{T,i}} \right|. \quad (4.49)$$

The result of the convergence check is shown in Figure 4.8 for a sail of height 30 m. The tested number of discretisations range from 10 to 100 with a step of 10. The sail system used for demonstration is the Flettner rotor, but the wingsail provide very similar results of ΔC_T . During the rest of the thesis work a number of 70 discretisations is chosen, with a limit of 0.3% in ΔC_T . Although the convergence analysis uncover that the relative change of thrust coefficient is small even for a lower number of discretisations, the Python code is a relatively quick analysis to run. Thus, there is little need to speed up the calculations by decreasing the number of discretisations. Furthermore, the low error between each iteration means that a larger sail height can be used with the same number of discretisations within a reasonable convergence criteria. This enables an analysis of different sail heights.

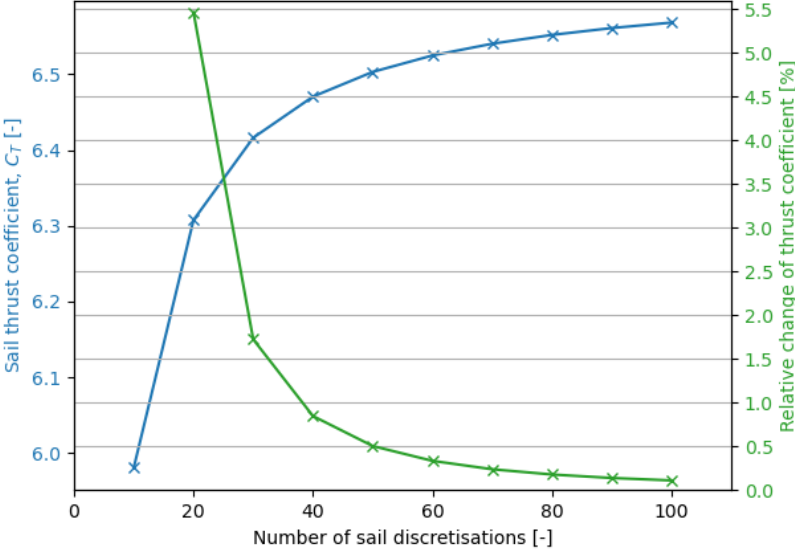


Figure 4.8: Sail discretisation convergence check, Flettner rotor.

Chapter 5

Sail model verification

This chapter goes through the verification of the aerodynamic model described in chapter 4. Different results from literature are used as targets for comparison with the results of the model. Firstly, the implementation of the aerodynamic theory is verified in section 5.1 with regards to steady force generation. Secondly, the numerical damping model caused by the dynamic ship rigid body motions is compared with an analytically derived model in section 5.2.

5.1 Sail force generation

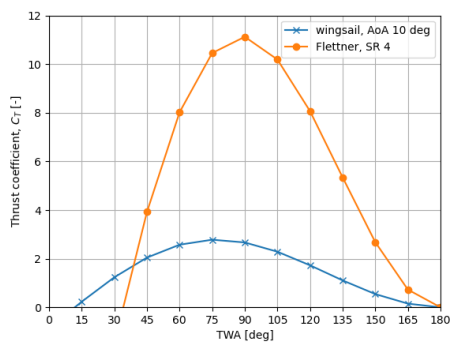
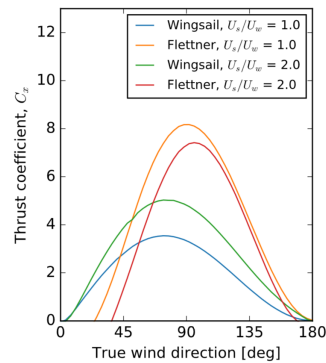
The first verification point is the steady thrust generation of the sail systems. The results of the model are compared with the external results of Kramer et al. (2016a) who used CFD. In Figure 5.1, the thrust coefficient of each of the sail systems are presented as functions of TWA. Figure 5.1a shows the results of the aerodynamic model created for this thesis, while Figure 5.1b is the graph presented in Kramer et al. (2016a). The thrust is made dimensionless with respect to TWS,

$$C_{T, TWS} = \frac{F_D}{\frac{1}{2}\rho_a TWS_{10}^2 A_p}. \quad (5.1)$$

The subscript TWS is added to mark the difference from Equation (4.48), where the thrust coefficient was normalised with respect to AWS.

The overall shape of the thrust coefficients corresponds well to those of Kramer et al. (2016a). It is recommended that one does not pay excessive attention to the actual values of the thrust coefficients for three key reasons. Firstly, the numerical methods differ such that the lift and drag coefficients are modelled differently. Secondly, the ratio of the ship velocity and wind velocity (denoted U_s/U_w in Kramer et al. (2016a)) differ, making the sail conditions incomparable. Finally, the wingsail model in Kramer et al. (2016a) has a flap in addition to the main sail foil. Additional differences which have not been listed may produce further deviations. In fact, the wingsail thrust coefficient of Figure 5.1a is amplified by a factor 2 to better observe the shape.

The key concept to take from the comparison is not the magnitude of the thrust coefficient, but rather, its relationship with respect to TWA. Three similar features between the thrust coefficients of Figure 5.1a and 5.1b are observed. Firstly, the thrust coefficient shapes with respect to TWA are similar. Secondly, the results agree on the wind angle at which the thrust coefficients peak. Thirdly, the angle range of positive thrust is equal, particularly for the Flettner

(a) The aerodynamic model. $V_S/V_T = 0.64$ 

(b) Kramer et al. (2016a)

Figure 5.1: Comparison of calculated thrust coefficient with external reference (Kramer et al., 2016a)

rotor. These three similarities confirm that the created aerodynamic model produces reasonable results on the sail's reaction to true wind angle.

A more appropriate source for comparison of the lift force density is Reche (2020) who created a performance prediction programme for the evaluation of sail systems. However, the named work used other experimental data for Flettner rotor force coefficients, which predict a smaller magnitude than the expressions implemented in this thesis. Table 5.1 presents the 3D lift coefficient and lift density, i.e. force per unit projected sail area, of one Flettner rotor and one wingsail. The results of Reche (2020) are marked with the source citation, while the results of the aerodynamic model of this work are marked with the rigid body mode from which they are calculated.

Table 5.1: 3D lift coefficient [-] and lift force per unit projected sail area [N/m^2].

WAPS and source/mode	3D C_L [-]	L/A_p [N/m^2]
Flettner rotor, Reche (2020)	9.15	650.37
Flettner rotor, $\dot{\eta}_4 = 0$	12.23	847.35
Flettner rotor, $\dot{\eta}_5 = 0$	12.23	847.51
Wingsail, Reche (2020)	1.18	83.45
Wingsail, $\dot{\eta}_4 = 0$	1.12	81.95
Wingsail, $\dot{\eta}_5 = 0$	1.09	80.21

The results in Reche (2020) were produced to compare the two sail systems. Firstly, the Flettner rotor values were obtained from a condition that gave the maximum forward thrust, TWA 10 m/s, V_S 12.5 kn and TWA 110°. The Flettner rotor was of dimensions 30m x 5m, such that the AR is 6, and it was fitted with an end disk of d_e/d equal to 2. Secondly, the maximum possible wingsail coefficient was determined from sail data. The wingsail with no flap was of AR 2. The required projected sail area to equalise the rotor lift was then calculated. The wind assisted ship model of Reche (2020) did not consider rigid body motions. Thus, to better compare the wingsails, the results of this work were collected at the instant where rigid body motions are zero. However, the calculations are based on $\omega = 0.7$, $\eta_{4a} = 0.07$ and $\eta_{5a} = 0.03$. The justification for the selection of these parameter values will be detailed in chapter 7.

One must keep in mind that the work of Reche (2020) is a performance prediction programme,

such that the sail is optimised to obtain maximum savings at the given ship speed. The sail model of this thesis does not support optimisation. Thus, to target the WAPS state of Reche (2020), the SR of the Flettner is set to 5. According to Figure 4.4, the lift coefficient ceases to increase around this point. However, the drag coefficient continues to increase, which should lead to lower thrust.

As explained above, the wingsail results in Reche (2020) are produced to equalise the Flettner rotor lift. Thus, a similar result production is done in the current sail model to check whether the model can reproduce similar results. Reche (2020) reports a required projected wingsail area of 1163.47 m^2 if the AR is 2. This corresponds to a sail of height 48.2 m and chord length 24.1 m, and these dimensions are trialled in this model. Because of the sail height and motion induced horizontal wind velocities (V_R and V_P), stalling must be ignored. Otherwise, the reported lift coefficient of Reche (2020) would not be obtainable over the whole sail height. This is not a problem for Reche (2020) when the rigid body motions are ignored. One can justify the ignored stall by the fact that the results of Table 5.1 are obtained when the rigid body motion is zero. If it was zero for all times, stalling would not be a problem, as it would be easy to trim the sails when AWA is independent of V_R or V_P . Therefore, the described configuration can be used to confirm correct implementation of the aerodynamic foil theory. The angle of attack is set to 20° , the angle where maximum theoretical lift is achieved, see Figure 3.6.

With reference to Table 5.1, the effect of the small rigid body motion perturbation is less pronounced for the Flettner rotor than the wingsail. The rotor is less sensitive to the wind angle. In Table 5.1, one notes two results, one for zero roll velocity and one for zero pitch velocity. These values are unequal because of how the model trims the sail. The wingsail trim is based on the height- and time-averaged AWA over the sail and an encounter period, which is dependent upon the rigid body motion. The Flettner rotor RPM is trimmed relative to the height- and time-averaged AWS. Thus, the lift force densities of the two sail systems is not equal in roll and pitch modes, even though the result is obtained at the time where the motion is zero. The differences are, however, relatively small.

Comparing the results of Reche (2020) with this aerodynamic model, the difference between the Flettner rotor results is large. However, this is expected, given that the experimental lift coefficients differed significantly. Good agreement is observed for the wingsail, Table 5.1.

5.2 Damping derivatives

The numerical damping model is tested against the analytically derived expressions Sinclair (1991), who presented dimensionless damping coefficients, i.e. damping derivatives. Sinclair (1991) includes roll and pitch induced damping derivatives in roll, pitch and yaw. Both lift and drag contributions are accounted for, by assuming a thin symmetric aerofoil with theoretically known values of lift, form drag and moment coefficients at zero angle of attack. Dynamic lift is included by the Theodorsen's function, $C(k)$. Other assumptions of Sinclair (1991) include a steady and uniform true wind velocity, i.e. neglecting the atmospheric boundary layer, a rectangular wingsail (taper ratio 1), small angle of attack, harmonic oscillations and no hull interference effects. More details on the derivation can be found in the source.

The analytically derived damping derivatives of Sinclair (1991) are,

$$b_{44} = 0.5 F(k) E_1 [(1 + 0.5\alpha^2) \cos(2 \text{AWA}^* - \alpha) + 1], \quad (5.2a)$$

$$b_{54} = 0.5 F(k) E_1 [(1 + 0.5\alpha^2) \sin(2 \text{AWA}^* - \alpha) + 3\alpha], \quad (5.2b)$$

$$b_{45} = 0.5 F(k) E_1 [(1 + 0.5\alpha^2) \sin(2 \text{AWA}^* - \alpha) - 3\alpha], \quad (5.2c)$$

$$b_{55} = 0.5 F(k) E_1 [1 - (1 + 0.5\alpha^2) \cos(2 \text{AWA}^* - \alpha)]. \quad (5.2d)$$

The yaw damping derivatives are omitted, as yaw is beyond the scope of the numerical model created in this thesis. In Equation (5.2), AWA^* is the apparent wind angle measured relative to the ship longitudinal axis, such that $\text{AWA}^* = \text{AWA} - \beta$. $F(k)$ is the real part of $C(k)$, see Equation (3.18). $E_1 = 2 \cdot \text{AR}^{0.6}$ is obtained assuming representative values of taper ratio 1 and gap ratio 0.2. The gap ratio is defined as f/H , the normalised distance between the sail bottom and sea surface with respect to the wing span, i.e. sail height. Standard aerofoils with moderate to high lift-to-drag ratios are assumed.

According to Sinclair (1991), the damping derivatives are made non-dimensional with respect to the air density, the steady apparent wind speed, sail projected area and the squared steady moment lever arm, $\frac{1}{2}\rho_a V_A A_p z_M^2$. In a ship propulsion point of view, the data are related to the true wind speed. Therefore, the expressions of Equation (5.2) can be multiplied by a factor of (V_T/V_A) to obtain damping coefficients normalised by the true wind velocity. Thus, for comparison with the work of Clayton and Sinclair (1988), the coefficients obtained from the aerodynamic model of this thesis are made dimensionless according to,

$$b_{jk} = \frac{B_{jk}^{\text{aero}}}{\frac{1}{2}\rho_a V_T c H z_M^2} \quad j, k = 4, 5, \quad (5.3)$$

where the lever arm of the steady moment is $z_M = \frac{1}{2}H + f$ (Sinclair, 1991). B_{jk}^{aero} is defined in Equation (4.22).

Figure 5.2 presents the four damping derivatives as functions of TWA. The label ‘‘numerical model’’ refers to the aerodynamic model of this thesis. Recall that the expressions of Equation (5.2) are multiplied by the factor (V_T/V_A) in this figure. Due to differences in the defined coordinate systems, the coupled damping terms of the current work and Equation (5.2) are of opposite signs. Hence, in Figure 5.2, b_{jk} from the current work is plotted with $-b_{jk}$ from Sinclair (1991) for $j \neq k$. The taper ratio is 1 in both models, and neither model includes flaps on the wingsail. The following list describes other parameters that have been set to certain values to facilitate a direct comparison of the two models.

- The gap ratio is set to 0.2 in the numerical model because of the assumed value in Sinclair (1991).
- The target AoA is set to 10° in the numerical model to ensure the avoidance of stalling. As Sinclair (1991) do not consider stalling, Equation (5.2) could technically be used for any angle of attack. However, large angles will induce stalling in the numerical model.
- $F(k)$ in Equation (5.2) is set to 1 as dynamic lift is neglected in the numerical model.
- β equal to 5° is assumed in both models.
- The atmospheric boundary layer is disregarded in the numerical model, due to the assumption of Sinclair (1991). In other words, TWS is constant over the sail height, unlike Equation (4.23).

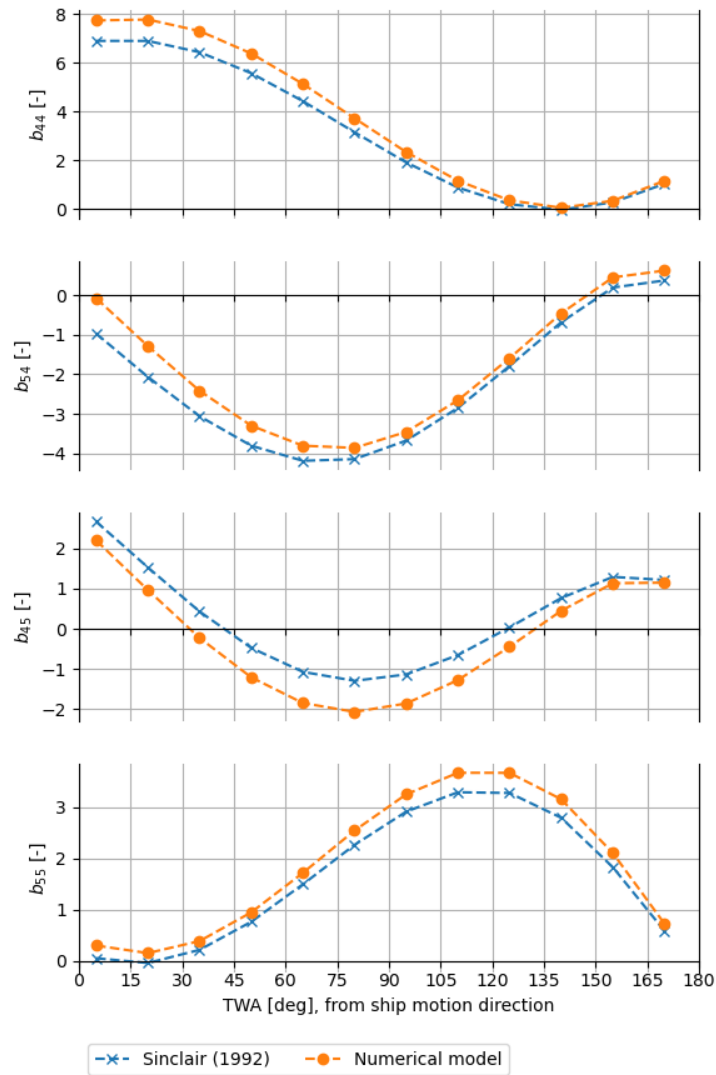


Figure 5.2: Comparison of induced damping derivatives

The shape of the damping derivatives as functions of TWA are well-captured by the numerical model. The magnitude differences are largest in head winds for b_{44} . However, b_{54} , b_{45} and b_{55} show the largest relative errors, considering the derivatives are of lower values than b_{44} . The differences might be partially attributed to differences in the theoretical lift coefficient. Simple linear foil theory is implemented in the numerical model, while Sinclair (1991) use load grading integrals of Abbott and von Doenhoff (1959).

Chapter 6

The wind assisted ship model

This chapter describes the model of the wind assisted ship used in the seakeeping analysis. It is obtained by superposing the aerodynamic sail model described in chapter 4 and the hydrodynamic system of a conventional ship. The latter is subject to the theory described in chapter 2. Calculations are performed with the two ShipX Plug-Ins Vessel Responses (Veres) and Ship Speed and Powering. Their use in the analysis is explained in the following sections.

6.1 Assumptions of the model

In section 4.2, the assumptions of the aerodynamic sail model were described. With reference to these, some additional assumptions about the wind assisted ship model are required for completeness:

1. Potential theory is valid, i.e the fluid is incompressible and inviscid, while the flow is irrotational.
2. Linear wave theory is applicable. The wave induced motions and load amplitudes are linearly proportional to the wave amplitude.
3. The body is slender and strip theory is applicable. This means that the submerged part of the body is divided into a finite number of strips, the flow is approximated as two-dimensional at each strip and integration along the body is used to obtain three-dimensional results.
4. The wave and wind directions coincide, i.e. $\beta_w = \text{TWA}_{10}$. These will sometimes be referred to as wind and wave heading in the remaining chapters. The assumption means that swell is neglected, to reduce the variables in the analysis.
5. The sea environment is described by irregular waves only, i.e. there is no current.
6. The aerodynamic damping coefficients of the sail system are independent of the hydrodynamic coefficients and these are superposable in the equations of motions.
7. The sailing problem is quasi-steady, i.e. the ship sails with a constant velocity in an environment where the wind and wave heading is constant and the steady sea state is described by a wave spectrum with constant significant wave height, H_S , and peak

period, T_p .

8. The ship's rigid body motions are characterised by significant amplitudes, which are used as inputs in the aerodynamic damping model.

As described in section 4.2, the ship drift angle is assumed positive and constant for all sailing cases. This is a generalisation and not physically correct. The drift angle affects the roll and pitch moments on the vessel, according to Equation (4.38) and (4.39). For small angles, the effect on the moments are small. Furthermore, the dominant cosine terms in Equation (4.38) and (4.39) are unaffected by a sign shift in β , as long as $\beta < 90^\circ$. This condition is true at normal operating conditions of a wind assisted vessel. Thus, the constant drift angle assumption is acceptable in this work, which focuses on the ship motion. In a propulsion analysis of a wind assisted ship, it would be required to calculate the drift angle by obtaining force equilibrium at each sailing condition.

6.1.1 Representative ship and sea states

The sample ship of this analysis is the open ship hull geometry SINTEF Ocean Bulk Carrier 1 (SOBC-1). The ship hydrostatics report from ShipX is given in Appendix B.1 but the principal hull data relevant for the current chapter are presented in Table 6.1.

Three representative sea states, Table 6.2, are defined for the wind assisted ship based on hindcast weather data from the North Sea (MetOceanView, 2021). The location is assumed to be a reasonable area of operation. The JONSWAP spectrum is assumed applicable since it is based on a project in the North Sea and is commonly used in the industry. The peak parameter of each sea state is calculated according to the recommended practice by DNV, Equation (2.5), and the results are given in Table 6.2. It may be noted that because γ is 1 for sea state 1 and 3, these states are in fact described by the PM spectrum.

Table 6.1: Principal hull data of the SOBC-1.

Parameter	Symbol	Value	Unit
Length overall	L_{OA}	199.299	m
Length on designed waterline	L_{WL}	196.942	m
Length between perpendiculars	L_{PP}	190.000	m
Length over surface*	L_{OS}	200.002	m
Breadth waterline	B_{WL}	32.201	m
Depth to 1st deck	D	23.502	m
Draught at $L_{PP}/2$	T	11.000	m
Bilge radius		2.000	m
Wetted surface of transom stern	A_T	2.91	m ²
Displacement	Δ	50351.4	tonnes
Vertical centre of gravity**	VCG	11.000	m
Trim	t	0.000	m
Block coefficient	C_B	0.727	[-]
Water plane area coefficient	C_W	0.828	[-]
Mid section area coefficient	C_M	0.995	[-]

* Relevant for Hollenbach's method to calculate C_R

** Measured from base line

Table 6.2: Sample sea states.

Number	H_S [m]	T_p [s]	γ [-]
1	3	14	1
2	2.5	8	1.58
3	2	12	1

6.2 Calculation tool: ShipX

Calculations of the wind assisted ship is performed using the two ShipX Plug-Ins Vessel Responses (Veres) (D. E. Fathi, 2018) and Ship Speed and Powering (D. Fathi et al., 2021), created by SINTEF Ocean, former MARINTEK. Veres is a tool intended for early design, and while the details on the implemented theory can be studied in the manual, it must be known that it is based on linear, potential strip theory. These assumptions invoke limitations on the model. The theory is developed for moderate wave heights inducing moderate ship motions and the ship's length should be much larger than the breadth and draught. The change of cross-sectional area with the ship length should be small and the vessel is symmetric about the centreline. This leads to the possibility of reducing the three-dimensional problem to a set of two-dimensional strips, assuming no interaction between them. The forces are then obtained by integration over the ship length. Furthermore, strip theory is applicable for Froude numbers lower than 0.4 (Faltinsen, 1993).

The fact that ShipX assumes a symmetric flow results in an incompatibility with the wind assisted ship model and its aerodynamic model described in chapter 4. It means that the drift angle cannot be included in the calculations. The tool is still deemed sufficient for this analysis, as it presents an initial study of the seakeeping capabilities of a wind assisted ship. As will be discussed in section 6.4, the importance of the drift angle might not be significant for a wind assisted ship, such that the angle is small in practice. Thus, in the present work, the drift angle effect is present in the estimation of the aerodynamic roll and pitch moments (see chapter 4) and the steady added resistance due to drift (section 6.4). Its effect on the ship motions in an unsymmetrical flow picture should be investigated in a more extensive analysis.

The Veres calculations are performed for an incident wave period range from 4 s to 40 s, with 48 periods in total. Within the range [4 s, 25 s] the interval is 0.5 s, while it is increased to 3 s in the range [25 s, 40 s]. The former, smaller sampling intervals are used to ensure a good resolution of the results in the resonance area, while the latter, larger intervals are used to reduce the number of calculations of the aerodynamic damping coefficients in Python.

Although potential theory assumes inviscid fluid, viscous damping is important in roll motions. Veres therefore includes viscous roll damping from empirical formulae. These are frictional damping caused by skin friction stresses on the hull, eddy damping caused by pressure variations on the naked hull and bilge keel damping. The latter is unimportant for the current analysis because bilge keels are not added to the hull. The other components are given in the following, as described in the Theory Manual of Veres (D. Fathi and Hoff, 2004). The frictional roll damping is,

$$B_{44}^{V1} = \frac{8}{3\pi} \cdot 0.9275 \rho_w S r_s^2 \omega^{0.5} \nu^{0.5}, \quad (6.1)$$

$$B_{44}^{V2} = 0.00755 \rho_w S r_s^{2.772} \omega^{-0.114} \nu^{0.114} \eta_{4a}^{-0.228}, \quad (6.2)$$

$$B = B_0 \left(1 + 4.1 \frac{V_S}{\omega L} \right), \quad (6.3)$$

where it is seen that the roll amplitude affects the non-linear component $B_{44} V^2$ in Equation (6.2). Equation (6.3) is used to correct for forward speed effects, where B_0 is the frictional damping at zero forward speed. The eddy damping is,

$$B_{44} V^1 = 0, \quad (6.4)$$

$$B_{44} V^2 = 0.5 \rho_w r_{\max}^2 \int_S c_p(s) l(s) ds, \quad (6.5)$$

$$B = B_0 \frac{0.04 \omega^2 L^2}{V_S^2 + 0.04 \omega^2 L^2}, \quad (6.6)$$

where r_{\max} is the maximum distance from the toll axis to the hull surface, $c_p(s)$ is the pressure coefficient, $l(s)$ is the roll moment lever and S is the wetted surface. Equation (6.6) is used to correct for a forward speed.

When solving the linear equations of motion, the viscous roll damping terms must be linearised. This is done by so-called equivalent linearisation, where the non-linear damping term is replaced by a linear damping term which provides the same work over one period (Faltinsen, 1993). The linear damping term is a function of the roll amplitude. Due to the linear relationship between roll amplitude and wave amplitude, known from the RAO, the equivalent linearisation requires the wave amplitude of the sea state.

6.2.1 Compatibility of coordinate systems

The global coordinate system in Veres equals the one defined in Faltinsen (1993), seen in Figure 6.1. The vertical position is optional and decided by the user. The two options are the centre of gravity and the still water plane, where the latter was chosen in the current work for compatibility with the coordinate systems of Figure 4.1. However, as Table 6.1 states, these two points coincide at the design load condition of the SOBC-1, so the choice is not of significance. The (x, z) plane coincides with the centre plane of the vessel. While the vertical positions of the global coordinate system and the motion coordinate system coincide, the horizontal positions do not. In the motion coordinate system, the horizontal position is the vessel longitudinal centre of gravity.

The aerodynamic model of chapter 4 calculates the damping coefficients subject to the (x, y, z) coordinate system of Figure 4.1, which is unequal to the coordinate system in Veres just described. However, the damping roll and pitch induced coefficients are still applicable to the Veres calculations because both the horizontal axes are oppositely directed in the aerodynamic model and Veres. Thus, a positive roll velocity in Veres equals a negative roll velocity in the aerodynamic model and a positive pitch velocity in Veres is a negative pitch velocity in the aerodynamic model. The resulting damping moments when using the same calculated damping coefficient are:

	Sign of $\dot{\eta}_4$	Sign of B_{44}	Sign of $B_{44}\dot{\eta}_4$	Equivalent ship rotation
Veres	+	+	+	Starboard up
The Simple Model	-	+	-	Starboard up
	Sign of $\dot{\eta}_4$	Sign of B_{54}	Sign of $B_{54}\dot{\eta}_4$	Equivalent ship rotation
Veres	+	+	+	Bow up
The Simple Model	-	+	-	Bow up

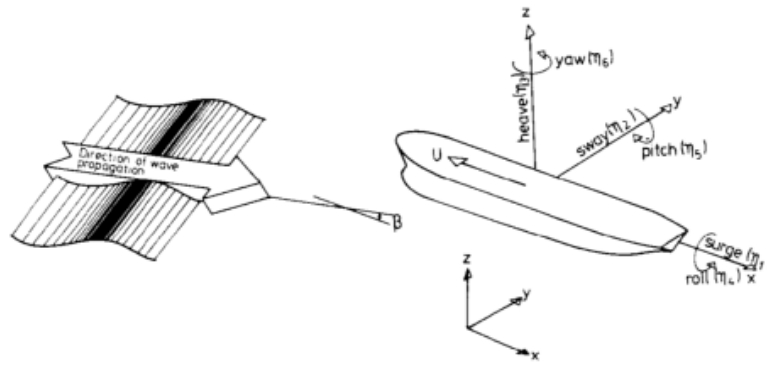


Figure 6.1: The global coordinate system and sign convention used in Veres. Reprint of Figure 2.2. Figure from Faltinsen (1993).

6.3 Quasi-steady sailing model

In the following, the methodology of the analysis is described. While all mentioned assumptions are important, the methodology is mainly based on assumption 7. With a quasi-steady model, the ship velocity, wave direction, wind direction and sea state is constant during each calculation. Several calculations are then performed for different constant parameters, such that the vessel response in different sailing problems are determined.

The hydrodynamic coefficients and excitation loads of the original ship are obtained from Veres calculations using the implemented 2D strip theory calculation method. These are written to the .re7 and .re8 files (D. E. Fathi, 2018). The damping coefficients of the sails are calculated with the Python code described in chapter 4 and written to a .txt file. If the wingsail is the chosen sail system, an additional .txt file is created (stall_info.txt), containing information about each situation that led the sail to stall during the calculations. In specific, this information include the ship velocity, wind and wave direction, wave frequency and forced rigid body motion.

The individual hydrodynamic and aerodynamic systems are then superposed. Because Veres does not provide the opportunity of adding an extra frequency-dependent damping matrix, the total wind assisted ship equation of motions are solved in an external program called NewMotions. The program is coded in Fortran by Senior Research Scientist Jan Roger Hoff at SINTEF Ocean, and given to the author of this thesis through personal communication. NewMotions may be seen as an extension of Veres, as it uses the calculated hydrodynamic coefficients and excitation loads from Veres (the .r7 and .r8 files), combines them with the additional frequency-dependent aerodynamic damping matrices and solves the equations of motion. In other words, the same theory used in Veres is implemented in NewMotion, the difference is the ability to input additional frequency-damping. Linear aerodynamic damping is assumed, but the program could theoretically be extended to include non-linear damping and an additional aerodynamic excitation matrix. However, due to the assumptions of this work's aerodynamic model, those extensions were not necessary. The results from NewMotion are written to a .r1 file which is imported into ShipX for Veres post-processing.

As mentioned in section 4.6, the model requires the amplitude of the rigid body motion to calculate the aerodynamic damping coefficient. The damping affects the vessel response, and so an iterative approach is required to solve the equations of motion. The initial amplitudes are the significant amplitudes of the original hull without sails, measured in the centre of gravity. For

each solution with sails, the RAO and significant amplitudes change as a result of the additional damping term. A convergence criteria in significant amplitudes of each sea state and wind and wave heading is required. The criteria is defined as,

$$\delta\eta_{s,k} = \left| \frac{\eta_{s,k}^{(i)} - \eta_{s,k}^{(i+1)}}{\eta_{s,k}^{(i)}} \right| < 0.1, \quad (6.7)$$

where $\delta\eta_{s,k}$ is the change of significant amplitude after an iteration is performed. The superscripts refer to the iteration number. The criteria of $\delta\eta_{s,k} < 10\%$ is based on the ship's roll resonance amplitude at 90° in sea state 3. Naturally, the roll response is largest in beam sea, and calculations show (see chapter 7) that sea state 3 provides the maximum amplitude of the three sample sea states. The amplitude is about 21.8° . Due to the relationship between the significant roll amplitude and the RAO, described in section 2.2.2, the accuracy of the roll amplitude is less than 2° with the 10% convergence criteria. It is deemed sufficient considering the many assumptions and simplifications of the model.

The above can be summarised into the steps of the calculation method, which are performed for one sea state at a time:

1. Calculate the short term statistical response of the original vessel for a range of wave headings.
2. For each wave and wind heading, use the significant amplitude to calculate the damping matrix as function of ship velocity and wave frequency.
3. Solve the superposed aerodynamic and hydrodynamic equation of motion.
4. Calculate the short term statistical response of the wind assisted ship each wind and wave heading.
5. Check for convergence of significant amplitude in both degrees of freedom and each wind and wave heading.
6. If the solution is not converged, perform step 2 – 5 again.
7. If the solution is converged, calculate the response transfer function of the wind assisted ship.

Finally, an additional note must be made regarding the aerodynamic damping coefficient calculation for the wingsail. As will be seen in the results of chapter 7, stall occurrence makes the sail forces non-harmonic and the linear damping model invalid. In other words, the ship response solution is irrelevant when stalling occurs and it should not be used in further analyses. The `stall_info.txt` file previously mentioned is used to compare the original vessel RAOs and resonance area with the periods where stalling occurs. The invalid results are discovered and can be discarded.

6.4 Wind assistance fraction

According to assumption 7, the ship velocity is assumed constant and known in this analysis. This means that the actual mechanism driving the ship is ignored. However, to quantify the importance of the sails in the sailing problem, the fraction of wind assistance (WA) is defined as the ratio of the driving force from the sails and the total ship resistance. In the case of Flettner rotors, the required power input must be included and is described as a force by the ship velocity,

$$\text{WA} = \frac{F_{D,\text{sail}} - P_{\text{rotor}} \cdot \frac{1}{V_S}}{R_T} \quad \text{Flettner rotor,} \quad (6.8a)$$

$$\text{WA} = \frac{F_{D,\text{sail}}}{R_T} \quad \text{wingsail,} \quad (6.8b)$$

The total ship resistance is the sum of the calm water resistance, the added resistance in waves and the added resistance due to drift,

$$R_T = R_{CW} + R_{AW} + R_{AD}. \quad (6.9)$$

While the theory related to these three components were described in section 2.3, required details on the application in the wind assisted ship model are given in the following paragraphs.

The calm water resistance (R_{CW}) is calculated according to the standard ITTC method implemented in ShipX Ship Speed and Powering (D. Fathi et al., 2021). The residual coefficient is estimated using Hollenbach's method, using the mean resistance curve. The complete set of calm water resistance coefficient report of a range of ship velocities is added in Appendix B.2. The projected area of the ship above water is required for the air resistance coefficient, Equation (2.30). As a rough estimate, the height of the superstructure is assumed to be equal to the freeboard height, based on observations of the dry cargo ship SC Connector and tanker Timberwolf (Norsepower, 2020a). The width is approximately equal to the ship breadth. Thus, using the ship hull dimensions of Table 6.1, the transverse area above water is roughly,

$$A_p = B \cdot 2f \approx 32 \text{ m} \cdot 2 \cdot 12.5 \text{ m} = 800 \text{ m}^2, \quad (6.10)$$

where the freeboard height is the difference between the depth to 1st deck and the draught. Ship Speed and Powering allows for several types of appendages to be added in the appendage resistance. Only a resistance due to rudder is included in this model for simplicity, to obtain a quick and easy estimate of the hull resistance. A reasonable approximation of the rudder area, A_R , is (Tillig, 2020),

$$A_R = 0.036 \cdot L_{PP}T = 0.036 \cdot 190.0 \text{ m} \cdot 11 \text{ m} \approx 75.0 \text{ m}^2, \quad (6.11)$$

and the wetted surface area of the rudder is assumed twice the rudder area. The suggested appendage parameter of 1.5 in Ship Speed and Powering is used.

The added resistance in waves (R_{AW}) is calculated in Veres. The implemented calculation method is the extended Gerritsma & Beukelman formulation by Loukakis and Sclavounos (1978), described in section 2.3.2. Within short term statistics, the mean added resistance of the SOBC-1 hull in waves is estimated for each sea state and wind and wave heading.

Finally, the added resistance due to drift (R_{AD}) is estimated. Keeping in mind that the focus of this thesis work is the sail's influence on the ship rigid body motion, the accurate prediction of

increased steady resistance due to drift has not been weighted. It is rather a conceptual estimate that is desired. Thus, the theoretical model implemented by Tillig and Ringsberg (2020) and described in section 2.3.3 has been used, and the resistance due to drift becomes,

$$R_{AD} = \frac{1}{2} \rho_w C_{Di} V_S^2 L_{PP} T, \quad (6.12)$$

where the drag coefficient C_{Di} is defined by Equation (2.58). The decrease of aspect ratio due to rounded edges, $(1 + \frac{\Delta s}{s})^2$ in Equation (2.55), is set to 0.78 for wings with rounded planform and rounded lateral edges (Hoerner, 1975). There is an uncertainty related to the estimation of the cross flow drag coefficient and the factor a of Equation (2.58), which in the work of Tillig and Ringsberg (2020) showed to differ significantly for a range of ships types. Because none of the sample ships studied by Tillig and Ringsberg (2020) matched the SOBC-1 hull in all three parameters C_B , C_M and AR, the average values of $k' = 0.6541$ and $a = 0.66$ have been used in this work. Thus, the added resistance due to drift is based on the drag coefficient,

$$C_{Di} = 0.66 \cdot C_{L,1} |\beta|^{0.6} + 0.6541 \cdot \sin^3 |\beta|, \quad (2.58, \text{reprinted})$$

$$C_{L,1} = 0.78 \cdot 0.5\pi \text{AR} \cdot \sin \beta. \quad (2.56, \text{reprinted})$$

It may be mentioned that the effect of a constant heeling angle is neglected, according to assumption 4 in section 4.2. This should not significantly affect the added resistance due to drift, as Fujiwara, Hearn, Kitamura, Ueno, and Minami (2005) reported the sway and surge forces on a bulk carrier to be fairly insensitive to changes of the heeling angle over a range of drift angles up to $\pm 30^\circ$.

Finally, the actual drift angle is required for the resistance estimation. Its importance is dependent upon sail type, the amount of thrust generated from it, the sail control strategy, whether the sail is retractable and the hydrodynamics of the vessel hull (Kramer et al., 2016a). The effect of drift on the added resistance of a general cargo ship fitted with a two-element wingsail or Flettner is evaluated by Kramer et al. (2016a). In the work, a route simulation was performed and the drift angle was calculated for a given wind speed, direction and sail loading. The energy savings reduction due to drift was small with only one sail, and naturally, the hydrodynamic effects increased with an increasing amount of sails. A clear difference between wingsails and Flettner rotor was observed, caused by the high side force to thrust ratio of Flettner rotors. The high drag force of Flettner rotors in off-position is also a source of added drift induced resistance. Including the effect of drift and rudder, the mean value of drift angle during the simulation with six wingsail was only around 1° . Excluding the rudder, the mean increased to around 3° . The corresponding mean values with six Flettner rotors were around 2° and 4.5° .

The current work does not solve the complete set of the equations of motion to obtain sailing equilibrium, such that the drift angle is found. Instead, a constant drift angle is assumed throughout the whole analysis of this work. This means that the influence of sail type and number of sails have not been considered, for simplicity and due to the objectives of this thesis. The drift angle is set to 5° in the wind assisted ship model, which is chosen as a conservative upper value based on the results Kramer et al. (2016a).

Chapter 7

Results

This chapter presents the results of the wind assisted ship analysis. Section 7.1 and 7.2 deal with the sails as isolated aerodynamic systems, from the model described in chapter 4. Results regarding the wind assisted vessel as a hydrodynamic and aerodynamic system are treated in the last three sections of this chapter.

As a base case, the parameters of Table 7.1 are defined. The sail and sailing data of this table is referred to as *the standard case*. The environmental data and ship rigid body motions of the standard case are only used in section 7.1 and 7.2, because the wind assisted ship results of section 7.3 to 7.5 are based on the representative sea states described in section 6.1.1, Table 6.2. Furthermore, the dimensions of the Flettner rotor are based on one of the commercially available rotors from Norsepower (2020b). The wingsail dimensions are chosen so as to obtain the same AR as the sail of the Oceanbird project (Wallenius Marine, 2020). However, the Oceanbird sails are unusually tall compared to other existing wingsails projects. Thus, the sail height was set to that of the Windship system (Windship Technology, 2020).

Table 7.1: Standard case data.

Rigid wingsail			
Height	H	35	m
Chord	c	10	m
Aspect ratio	AR	3.5	-
Flettner rotor			
Height	H	30	m
Diameter	d	5	m
Aspect ratio	AR	6	-
Sailing problem and environment			
Wave frequency	ω_0	0.7	rad/s
Significant wave height	H_S	2	m
True wind velocity	V_T	10	m/s
Ship velocity	V_S	12.5	kn
Drift angle	β	5	deg
Roll motion amplitude	η_{4a}	0.07	rad
Pitch motion amplitude	η_{5a}	0.03	rad

The number of variables in this analysis must be reduced compared to the true seakeeping problem. Thus, all results in this thesis are based on a ship velocity of 12.5 kn. This corresponds to a Froude number of 0.15, which is well within the limit of strip theory. Furthermore, the true wind velocity is 10 m/s throughout. The effect of ship and wind velocity in the wind assisted ship seakeeping problem is therefore not included in this work. Variables like the wind direction and frequency, the number of sails and target SR or AoA were deemed more interesting.

The weather data in Table 7.1, i.e. wave frequency, significant wave height and wind speed, are based on hindcast data from the North Sea (MetOceanView, 2021). The roll and pitch amplitudes originate from the roll and pitch RAOs for the SOBC-1 vessel at the relevant wave frequency. Other than choosing reasonable data, the particular values of weather data and motion amplitudes in Table 7.1 are not important, as they are only used in the isolated aerodynamic sail analysis of section 7.1 and 7.2. As mentioned, a more accurate calculation model, described in section 6.3, is used for the wind assisted ship model, presented in section 7.3 to 7.5.

7.1 Dominant damping mechanism

To evaluate the dominant damping mechanism of the sails at various wind angles, a selection of TWA have been tested. These cases are summarised in Table 7.2 with corresponding steady apparent wind angle and encounter frequency. The dimensions of the sails and the properties of the sailing problem are the ones of the standard case, Table 7.1. The complete amount of plots showing the induced roll and pitch moments at each wind angle are added in Appendix C and D for the Flettner rotor and wingsail, respectively. The moments calculated by the model of this thesis are labeled “numerical model”. The label “linear model, curve fit” refers to the application of a linear damping model to the numerical result, as described in section 4.2. The global coordinate system, Figure 4.1, is frequently referred to throughout the following section and should be revised before reading.

Before each sail mechanism is evaluated, the following note can be made regarding the the apparent wind angle and velocity. In head apparent wind, i.e. $AWA < 90^\circ$, the AWA_U and AWS_U vary in phase with each other in roll mode, and out of phase in pitch mode due to the induced horizontal velocities, V_R and V_P . In following apparent wind, $AWA > 90^\circ$, they are in phase with each other in pitch mode and out of phase in roll mode.

It should be noted that the drift angle affects the result of this evaluation because it defines the angle between the global and local coordinate axes. For a small drift angle, the driving force is almost in parallel with the surge direction and the heeling force with the sway direction. This is not true if the drift angle is large and one must be careful to apply the following results to a ship with a larger drift angle causing significant deviation.

Table 7.2: Wind angle cases in evaluation of damping mechanism.

Case number	1	2	3	4	5	6	Unit
TWA_{10}	30.0	70.0	110.0	130.0	150.0	175.0	deg
$AWA_{S,10}$	18.3	43.6	72.2	90.0	114.0	166.1	deg
Encounter frequency, ω_e	0.84	0.99	1.01	0.96	0.88	0.76	rad/s

7.1.1 Flettner rotor

The target SR is set to 3 in all cases to limit the variables in this evaluation. The particular SR was chosen because the increase of lift coefficient stagnates at approximately SR 4, Figure 4.4, and the force generation will thus vary over the sail due to the local SR. Although the target might not be the best configuration in a ship power performance point of view, it is not the purpose of this evaluation.

The dominant mechanism causing damping in each case and mode is summarised in Table 7.3. If a force is added in parenthesis, it is contributing to the damping, but to a lesser degree than the other force in the cell. Judging from Table 7.3, the coupled damping terms (B_{54} and B_{45}) are caused by the lift force, while the decoupled damping terms (B_{44} and B_{55}) are mainly caused by drag. Furthermore, observations during this analysis show that the lift force varies more with respect to time than the drag force, due to the steeper slope of the lift coefficient. In roll mode, the driving force is varying more than the heeling force, while it is the opposite in pitch mode.

Table 7.3: Dominating damping mechanisms of a Flettner rotor.

Case	TWA	B_{44}	B_{54}	B_{45}	B_{55}
1	30°	drag	lift	lift	drag
2	70°	drag and lift	lift	lift	drag
3	110°	drag and lift	lift	lift	drag
4	130°	drag (lift)	lift	lift	drag
5	150°	drag	lift	lift	drag
6	175°	drag	lift	lift	drag and lift

As mentioned previously, the apparent wind velocity and angle are in and out of phase with each other depending on wind heading and rigid body mode. The cases show that the lift and drag forces are always in phase with the wind velocity. In other words, the force magnitude increases more at high AWS_U than the force coefficient decreases at this instance due to low SR.

The induced moments during case 3 are given in Figure 7.1, which is provided as an example for illustrative purposes. In roll mode for AWA_S less than 90°, the AWS and AWA vary in phase with each other and it is this feature that is causing the damping. The lift force is mainly directed in the global X-direction since AWA_S is 72.2°, Table 7.2. Figure 7.2 shows the two extreme situations of maximum and minimum V_R . Different colours are used to clearly distinguish between the maximum (blue) and minimum (green). The black arrows are the steady velocity vectors that are present in both. The lift magnitude is at its maximum when AWS_U and AWA_U are at their maximum. Because of maximum AWA_U , the lift is more aligned with the X-direction than at AWA_S . Similarly, the lift is at its minimum when AWS_U and AWA_U are at their minimum. Hence, when moving from the AWS_U and AWA_U minima, the angle induced increase of the X-component of lift is further amplified by the increase of lift magnitude due to the wind velocity. At the same time, the angle induced decrease of lift in Y-direction is compensated by the velocity (and magnitude) induced increase. Thus, the lift contributes to pitch damping because of the large variation in X-direction. The orange dashed lines in Figure 7.2 show that there is a large change in the lift X-component, while the change in the Y-component is smaller.

The same mechanism can be observed for the drag force causing roll moment in Figure 7.2, where the Y-component of drag varies more than the X-component. With reference to Figure 7.1a, the lift is also contributing to roll damping because of the larger magnitudes compared to drag. However, as discussed, the lift variation in pitch is much larger than in roll.

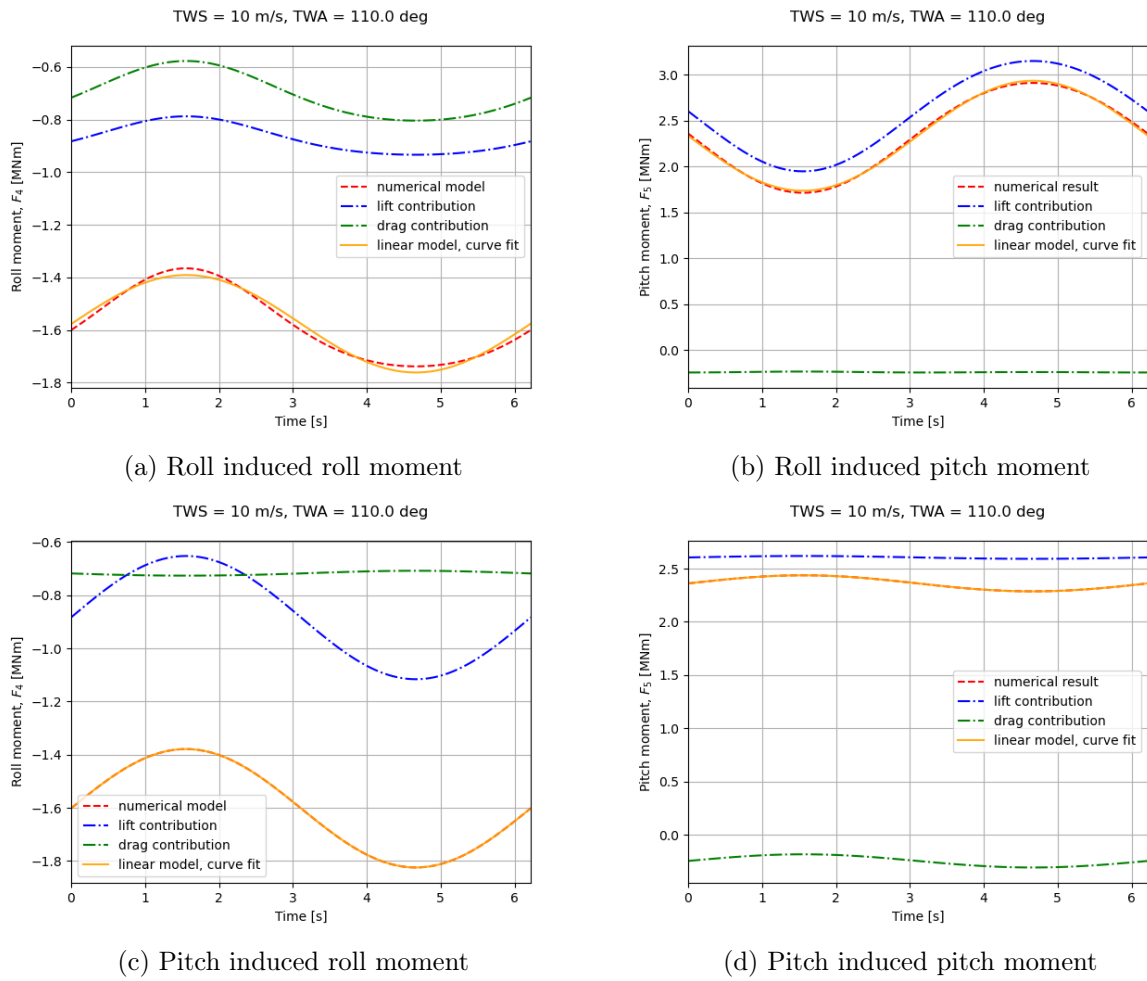


Figure 7.1: Aerodynamic roll and pitch moments from Flettner rotor, case 3: TWA = 110°.

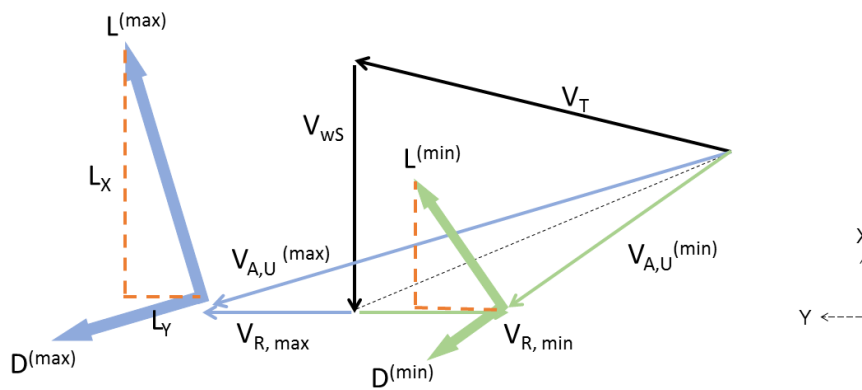


Figure 7.2: Change of Flettner rotor lift force during an oscillation of V_R . The figure is meant as an illustration, and magnitudes and angles are not of correct values.

In pitch mode, the situation is the opposite of roll mode. When V_P is positive, AWA_U is at the maximum, lift is mostly directed in X-direction, but AWS_U is at the minimum leading to minimum force magnitude. As the wind angle decreases when V_P is negative, the lift is directed slightly away from the X-direction. The magnitude increases due to larger AWS, such that the Y-component of the lift changes and causes roll damping. In the same way, drag causes the pitch damping.

The above holds for AWA_S above 90° as well. However, because the wind acts in the ship velocity direction, AWS_U and AWA_U act out of phase with each other in roll mode, and in phase with each other in pitch mode. It leads to the same dominant damping mechanism in each mode. For instance, the lift is mainly directed in the X-direction during case 5 as AWA_S is 114.0° . When AWA_U is at its minimum in e.g. roll mode, the angle between the lift force and X-axis is small. Simultaneously, AWS_U is at its maximum. Thus, the increase of lift force in the X-direction is induced by both the angle and velocity.

7.1.2 Wingsail

The wingsail is a high-lift device. In an unsteady wind environment at small angles of attack, the lift typically varies a lot more in magnitude than the drag force. This is caused by lift coefficient being proportional to α , Equation (3.10) and (3.12), while the drag coefficient is proportional to α^2 , Equation (3.13). Furthermore, the force magnitudes are proportional to $V_{A,U}^2$, which changes with the rigid body motion and contributes to the variation in both forces.

The target angle of attack is set to 10° in all cases, independently of whether it leads to sail stall at some time instances and sail heights. This way, both non-stalling cases and stalling cases are demonstrated in the six cases. The responsible mechanisms are summarised in Table 7.4. Note that the cases where sail stall occurred, clearly affecting the induced moments are marked in the table. In these cases, concluding that e.g. lift is the dominant damping mechanism is insufficient to describe the situation.

Table 7.4: Dominating damping mechanisms of a wingsail.

Case	TWA [deg]	B_{44}	B_{54}	B_{45}	B_{55}
1	30	lift	lift (drag)	-	lift
2	70	lift (drag)	lift (drag)	lift	lift
3	110	lift (drag)	lift	lift and drag	lift
4	130	lift and drag	lift	lift and drag *	lift *
5	150	lift (drag) *	lift (drag) *	lift (drag) *	lift *
6	175	lift *	lift *	lift	lift and drag

* Stall occurring and affecting the results

As mentioned previously, the apparent wind speed and angle are in or out of phase with each other depending upon the rigid body mode and whether the wind is head or following. The cases investigated show that the forces vary with the wind speed when the angle and velocity are out of phase. Thus, the roll induced moments are out of phase with the pitch induced moments.

Judging from Table 7.4, lift is the dominant mechanism in wingsail damping. Even though drag is significant or contributing in some cases, lift is never insignificant. Due to the described dependence upon the angle of attack, the lift generally varies more than the drag. The direction in which the forces act and their variation in magnitude due to the unsteady wind are the main causes of damping, and since the lift variation is greater than the drag variation, it is dominant

in almost every case and mode. For instance, in roll mode of case 1, the drag is mainly directed along the X-direction due to the head apparent wind, and so the drag variation causes pitch moment variation and thus damping. However, because of the inherent high lift-to-drag ratio of wingsails, the lift is large enough to contribute to pitch damping as well. In pitch mode, V_P and $V_{A,S}$ are mainly directed in the same direction, making AWA_U vary only to a small degree. Thus, the force variations are small and so is the damping.

In case 2, when AWA_S is almost 45° , lift and drag are approximately equally directed in X- and Y-direction, such that the pitch and roll damping in each mode are relatively similar in magnitude and source. Case 4, Figure 7.3, demonstrates an exception to the above generalisation that the lift is almost always dominant. In this case, AWA_S is 90° , such that the lift is perfectly aligned in the X-direction and drag in the Y-direction. In roll mode, AWA_U is almost constant since V_R is parallel to AWA_S , but the drag and lift magnitude vary with AWA_U . Since the drift angle is small but present, the lift and drag are equally important in roll induced roll moment (see Figure 7.3a), contrary to other cases where lift is dominant and drag only of minor contribution. A similar deduction can be done for the case 4 pitch mode. However, V_P is perpendicular to AWA_S , which leads to a variation in AWA_U . It contributes to the force variation and even leads to sail stall, as shown in Figure 7.3c and 7.3d.

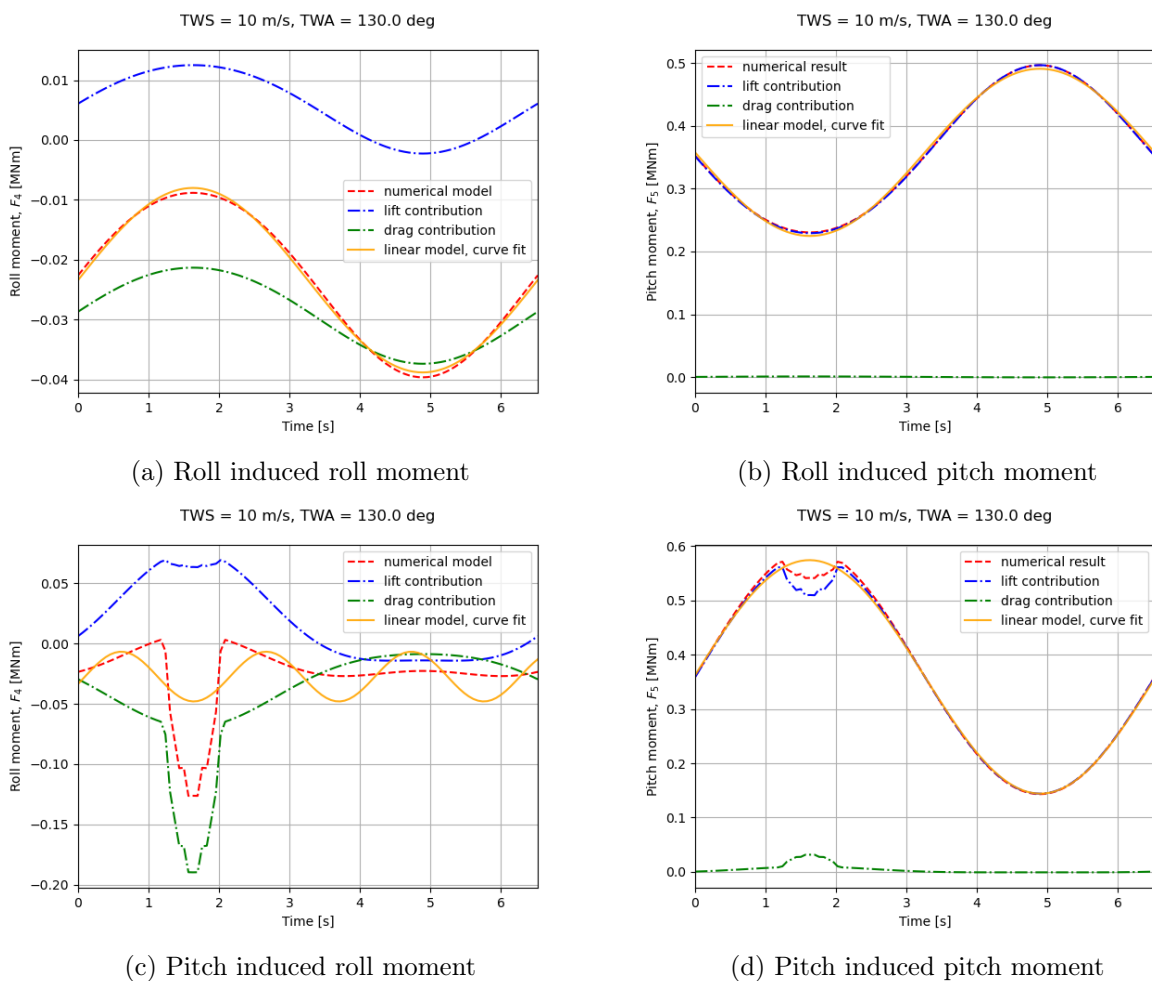
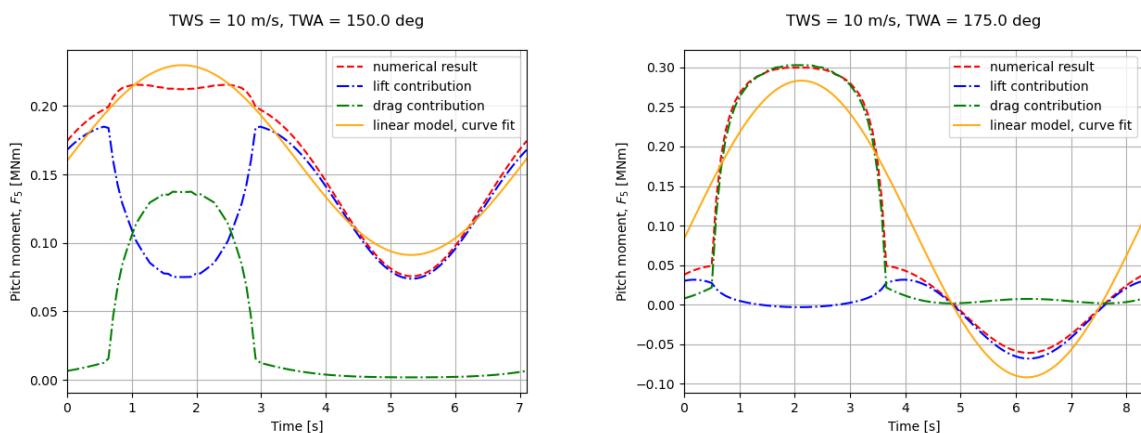


Figure 7.3: Aerodynamic roll and pitch moments from wingsail, case 4: $TWA = 130^\circ$.

Stalling is an important factor to the moment generation and damping. It occurs when the difference of maximum and minimum AWA_U are larger than the range of angle of attack where the sail foil does not stall. If so, the sail cannot be trimmed to avoid stall. Figure 7.3c is an example of where stalling leads to a large sudden increase in drag force and the roll moment adapts a spike-like shape. Although the magnitude might not be of significance in the overall sailing problem, it shows an important feature that an impulse moment, increase or decrease, can be generated due to sail stall and contribute to sudden impulse heeling force. Furthermore, the attempted linear model fit, seen as the orange sinus curve, is not a good fit. If the lift and drag forces are both contributing to a positive driving force, the increase of drag might compensate for the loss of lift when stall occurs, such that the total moment and damping are somewhat preserved, see the numerical result in Figure 7.4a. However, this feature is highly dependent upon drag and lift generation at stall. As described in chapter 4, the current model is not created to model stalling accurately enough for dependable conclusions to be drawn.

The sail trim configuration affects the moment and damping in case 6, Figure 7.4b. Trimming the sails relative to the mean AWA , the apparent wind tackles the foil from both sides of the sail throughout a cycle. In other words, the lift contribution to pitch moment adapts a harmonic-like shape with twice the frequency of the encounter frequency, if one ignores the effect of stalling temporarily. The doubled frequency arises from the fact that lift is generated from both sides of the sail and thus directed in opposite directions, leading to an additional oscillation to the already existing magnitude oscillation.



(a) Roll induced pitch moment, case 5: TWA 150° (b) Roll induced pitch moment, case 6: TWA 175°

Figure 7.4: Aerodynamic roll and pitch moments from wingsail, stall and trim effects.

7.2 Thrust and damping conflict

Six sample angles are chosen to observe the thrust and damping in head, beam and following wind. These are TWA 30.0° , 70.0° , 90.0° and 130.0° , 150.0° and 175.0° , which correspond to AWA_S of 18.3° , 43.7° , 57.3° and 90.0° , 114.0° and 166.1° , respectively. Figure 7.5 to 7.7 show the damping and thrust coefficients of the standard case sails as functions of relevant target loading (SR or AoA). While wingsail stalling is included in Figure 7.7, it is not included in Figure 7.6 to show the difference between a more realistic case and an ideal one. The thrust coefficient is defined according to Equation (4.48).

7.2.1 Flettner rotor

The topmost graphs in Figure 7.5 show that the thrust coefficient of Flettner rotors is unsymmetrical about zero SR. Due to the ship speed and the apparent wind, the flow around the cylinder with negative SR is not strictly the exact opposite of the flow with a positive SR. The drag direction is unaffected by the rotational direction of the rotor and is always parallel to the wind direction. For positive spin ratios, the lift contributes to positive thrust, while it for negative spin ratios acts as a break. Hence, the drag and lift do not work equally towards positive or negative thrust, resulting in the unsymmetrical thrust picture. The thrust coefficients are high at high rotational speeds in beam wind, although the increase is reduced at SR above 4. At this point, an increase of SR does not produce higher lift, but the drag increases. Little thrust is generated in head wind, which is seen in the case of TWA equal to 30° . While there is no propulsive motivation to use a Flettner rotor in such a condition, the damping data show that the rotor can contribute high damping coefficients in all modes but the roll induced pitch motion.

In roll mode, Sinclair (1991) reported that low rotational speeds could lead to negative roll damping in head apparent winds, especially in the range of $40^\circ - 60^\circ$. This feature is indicated by B_{44} in Figure 7.5a. The damping is negative for low positive SR and positive for low negative SR, if TWA is 30° , 70° or 90° . These all correspond to an apparent wind in the coordinate system's first quadrant. Thus, a conflict between thrust and damping is observed for moderate spin ratios for starboard head apparent winds. For example, at TWA 70° and SR -3, B_{44} is positive and C_T is negative. However, the presented results indicate that the conflict ceases to exist at higher absolute values of SR. For instance, at TWA 70° with SR above 2 and below -3.5, damping is positive and negative, respectively.

Utilising the Flettner rotor as a break to obtain voluntary speed loss is a possibility to reduce roll induced pitch motion. Although this condition might give negative roll damping, the magnitude of the negative roll damping is much smaller than the magnitude of positive pitch damping, which may make such a configuration worth the potential increase in roll motion. In pitch mode, the situation is different, and positive roll and pitch damping is achieved while obtaining positive thrust. However, another possible voluntary speed loss situation is observed in head wind, where a large increase of pitch damping is seen for large negative SR.

With reference to the decoupled coefficients in Figure 7.5a and 7.5b, the rotor contributes to positive damping even at SR equal to zero. A viscous drag force is always produced since this work does not consider the possibility of tilting the rotor when not in use. At the same time, the coupled damping is zero, and hence in a situation where the Flettner rotor is turned off, the rotor might give a small positive effect, and no negative effects to the ship motions.

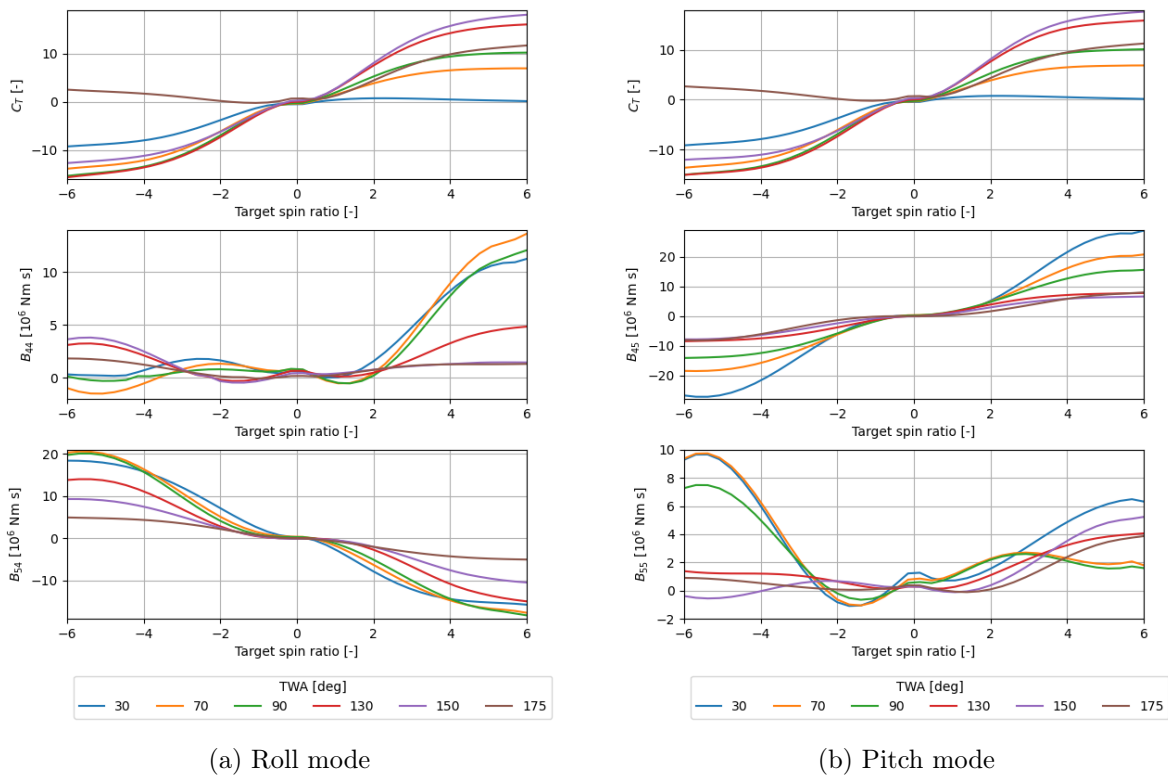


Figure 7.5: Flettner rotor damping and thrust as functions of spin ratio.

7.2.2 Wingsail

The thrust generated from a wingsail is dependent upon on the sail trim. Reasonable trim settings were briefly mentioned in section 4.5. The aerodynamic model in this work trims the sail based on the mean AWA over the encounter period and sail height. The following section is therefore based on this trim configuration, and the effect of trimming has not been explored.

One example of the effect of the current trim is the non-zero thrust at zero AoA in forced roll motion and following wind. See TWA 150° and 175° in Figure 7.6a or Figure 7.7a for reference. The AWA_U is not a perfectly harmonic function. The feature becomes more apparent in following wind or when the forced rigid body motion is more extreme. It leads to a non-zero mean thrust coefficient at zero target AoA because the mean local and instantaneous AoA is non-zero. Other trim configurations could be implemented, but was not considered in this analysis due to the main objectives. This feature is not relevant for Flettner rotors, which are insensitive to the wind tackle angle.

With reference to how Figure 7.6 differ from Figure 7.7, it is observed that thrust and damping of wingsails are highly affected by sail stall. In the ideal case of no stall, Figure 7.6a indicate that there is a conflict between thrust and roll induced roll damping for AWA above 90°, i.e. TWA 150° and 175°. The damping decreases slightly if AoA and thrust increase. However, the damping is always positive. It is also seen that beam apparent wind gives the largest thrust coefficient at any positive angle of attack because the lift is mainly directed in the ship velocity direction. At the same time, it provides poor, almost zero, roll and pitch induced roll damping. Instead, the pitch damping induced by roll and pitch motion is largest in beam apparent winds. The particular wind angle which provides the largest damping coefficient depends on the motion

mode, due to the rigid body motion affecting the unsteady apparent wind angle.

In roll mode, pitch damping is negative for $TWA \leq 90^\circ$ at most AoA, corresponding to starboard head apparent wind. The conflict between thrust and pitch damping is present for all wind angles investigated, but the rate of change of the damping coefficient is less prominent at $TWA 30^\circ$, 150° and 175° , corresponding to head and beam winds. In pitch mode, the conflict is indicated for AWA below 90° , while it changes for AWA above 90° . Here, the pitch damping increases with increasing thrust.

When stall is accounted for and occurs, Figure 7.7 shows that the above mentioned characteristics are lost. This generally happens at large AoA around the foil stalling angle, although the forced motion mode and TWA affects the actual point of stalling. Hence, Figure 7.7 coincide with Figure 7.6 at small and moderate angles of attack. At large AoA, the thrust is seen to quickly decrease due to loss of lift when the sail stalls. An interesting finding is that the thrust does not seem to decrease much at $TWA 150^\circ$. The responsible mechanism is the increased drag that compensates for the lost lift. Due to the local apparent wind angle, drag contributes to the driving force. In the current result, the drag seems to almost entirely compensate for the lost lift. However, this is highly dependent upon the value of modelled drag and lift coefficient at stall. As mentioned in section 4.5, reasonable values were chosen to model the penalty of stall, but the exact values should not be weighted.

Note the spike of B_{44} at AoA 5° for the case of $TWA 150^\circ$, Figure 7.7a. The extreme increase of damping is not physically correct and is caused by the inappropriate fit of a harmonic function to the aerodynamic roll moment. As a measure of the poor fit, the R^2 value of the harmonic function to the numerically calculated roll moment is around 0.13.

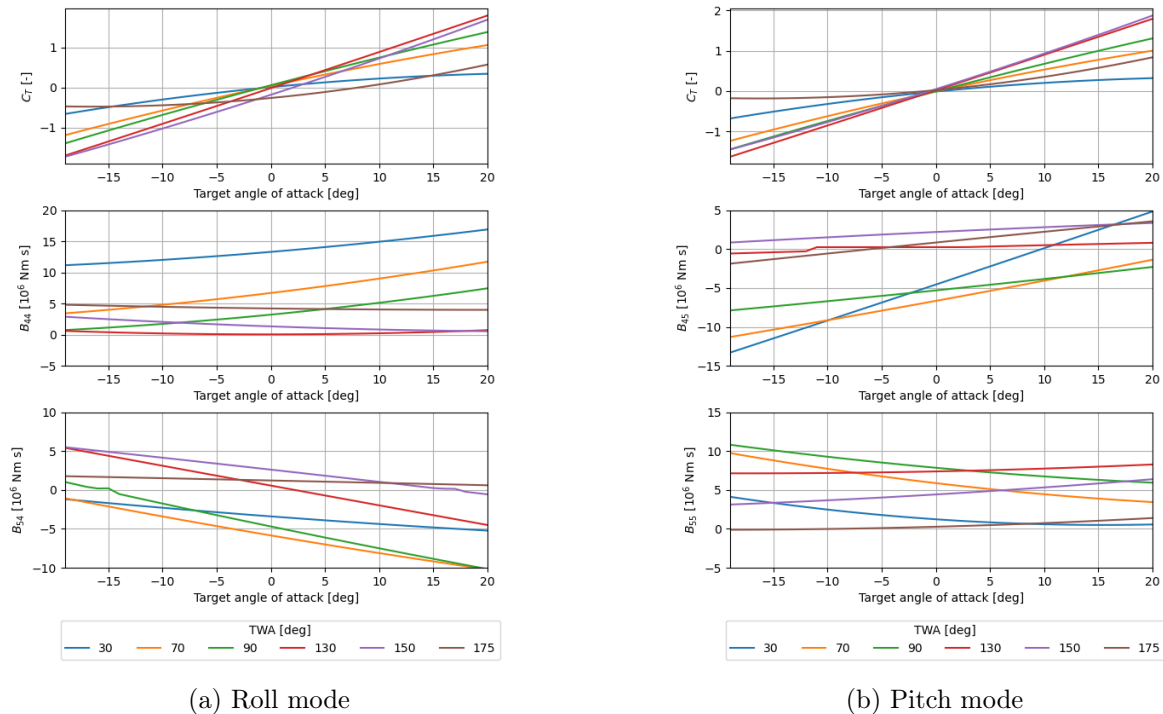


Figure 7.6: Wingsail damping and thrust as functions of angle of attack. Stall not included.

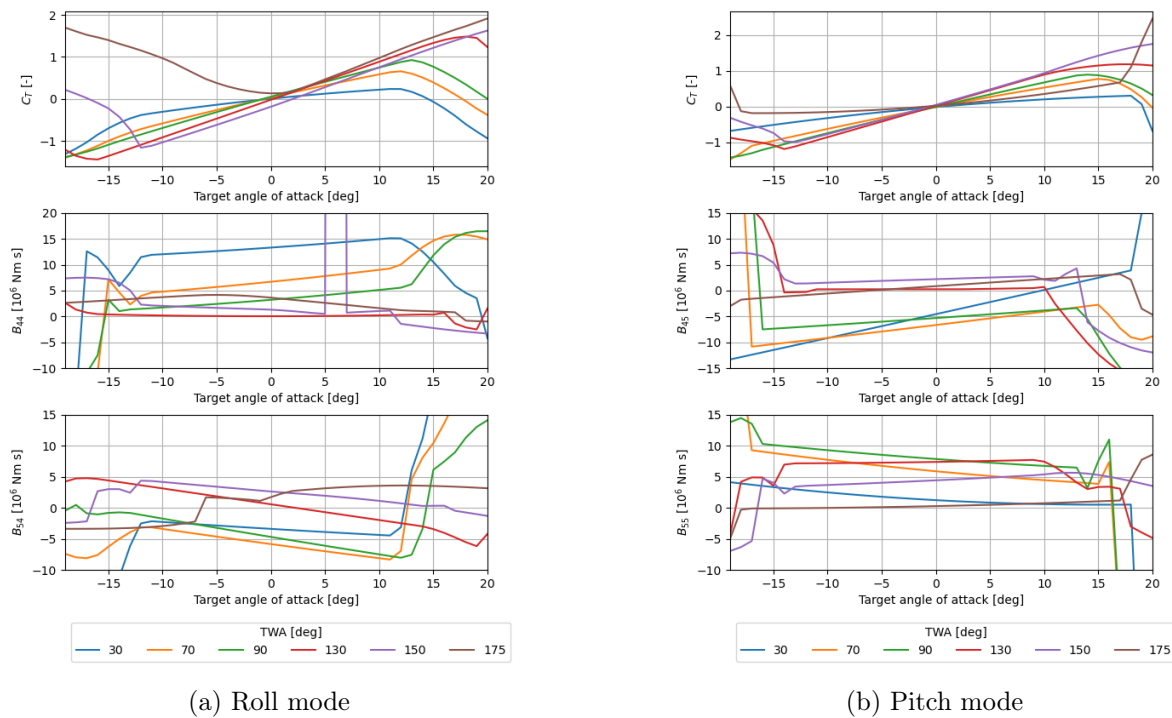


Figure 7.7: Wingsail damping and thrust as functions of angle of attack. Stall included.

7.3 Roll and pitch amplitude reduction

The roll RAOs of the original SOBC-1 hull without sails are shown in Figure 7.8. Only the RAOs of sea state 1 are produced to show the overall trend of the response. The magnitude of the RAOs at resonance will differ slightly between the sea states due to the viscous roll damping dependency on roll amplitude and thus wave amplitude. See section 6.2. Thus, since H_S decreases with the increasing sea state number (see Table 6.2), the linearised roll damping term decreases and the roll response at resonance increases. See Figure 7.9 for reference. The difference is most pronounced in beam sea where viscous roll damping is important. Nevertheless, the shape and resonance area of the RAOs in Figure 7.8 are representative for all sea states.

A measure of the effect of sail damping is the roll and pitch amplitude reduction at resonance. Satchwell (1986) quantified the roll reduction as given in Equation (1.2). In a general form to include pitch as well, the equation becomes,

$$\delta\eta_{ka,\max} = \frac{\eta_{ka,\max} - \eta_{ka,\text{WAPS},\max}}{\eta_{ka,\max}} \quad k = 4, 5, \quad (7.1)$$

where $\eta_{ka,\max}$ is the displacement amplitude in rigid body motion k at resonance for the original ship hull without sails, and $\eta_{ka,\text{WAPS},\max}$ is the equivalent for the wind assisted ship hull fitted with sails.

As described in chapter 6, iterations are required when solving the amplitude dependent solution. Table 7.5 presents a summary of all the cases investigated in this work, including the sea state (SS, referring to Table 6.2) and the number of iterations (Iter, column 3) required to obtain a converged solution. Iteration 1 corresponds to the first solution with sail damping included and iteration 2 is the second solution (based on significant amplitudes from the solution of iteration 1). The solution of the original hull without sails is referred to as iteration 0. Table 7.5 also provides

notes on stall occurrence for the wingsail cases, which is discussed more in the wingsail section below. The significant roll amplitudes from the response of iteration 0 is given in Figure 7.10. Two sail loading targets are chosen for each sail system; one small to moderate of AoA 5° and SR 2, and one higher loading of AoA 10° and SR 4.

For the following discussion on motion damping in each case, the reader should keep in mind that because interaction effects are ignored in the current work, the damping coefficients of for instance two Flettner rotors at SR 4 is simply equal to twice the damping coefficients of a single Flettner rotor at SR 4.

The wave amplitude, leading to roll motion amplitude through the response transfer function, is required as an input in Veres for viscous non-linear roll damping, Equation (6.2), and the equivalent linearisation. Unfortunately, during the analysis of iteration 0, the wave height was wrongfully entered into Veres. This causes the linear damping term to be overestimated, such that the RAO at resonance is smaller than if the correct parameter was used. It affects the significant amplitudes of the short term statistical response, Equation (2.19), which is used as input to the aerodynamic damping calculations of iteration 1. Unfortunately, the error was not discovered until all the calculations of Table 7.5 were performed, including iterations. However, it must be noted that the programme NewMotions uses the wave height, not amplitude. Thus, the calculations in NewMotions are based on the correctly estimated viscous roll damping, but incorrect significant amplitudes from iteration 0 in Veres. A check of the influence of the error has been performed and it is deemed insignificant. The significant amplitude of the corrected iteration 0 calculation changed less than 4% for all sea states and headings, compared to the incorrect one. The maximum change occurred in sea state 1, as the significant wave height (and thus the incorrectly entered amplitude) is largest here. Because the error is less than the convergence criteria, Equation (6.7), the calculations of iterations 1 and 2 have not been redone. Within the accuracy of this wind assisted ship model, the difference is insignificant.

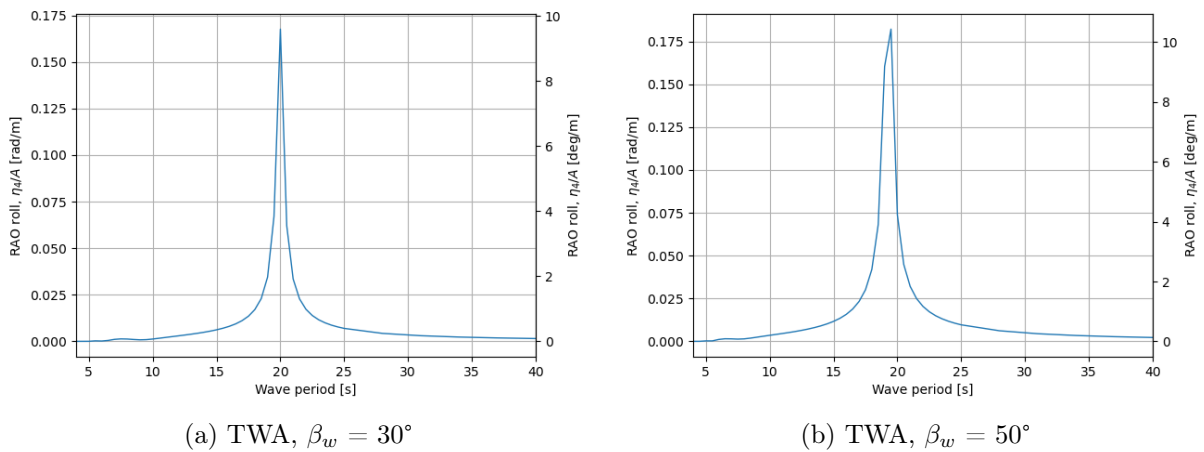
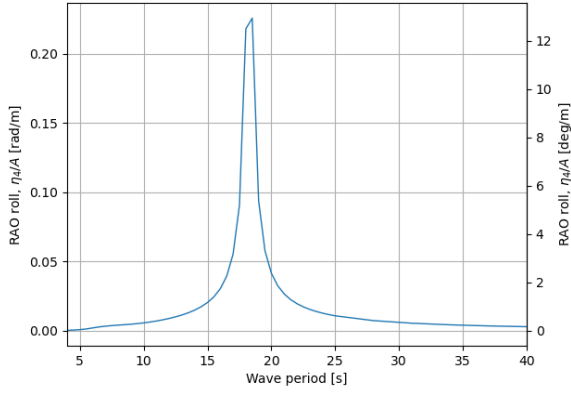
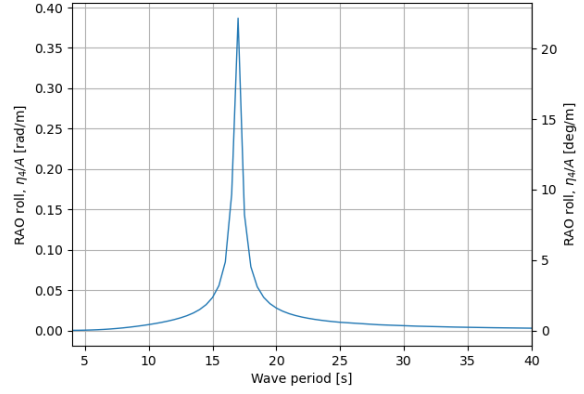


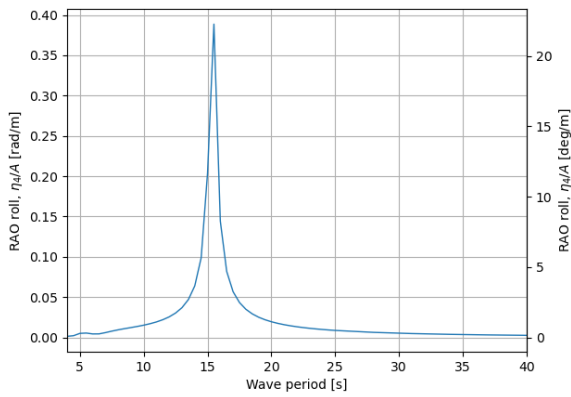
Figure 7.8: RAO in roll of the original hull without sails.



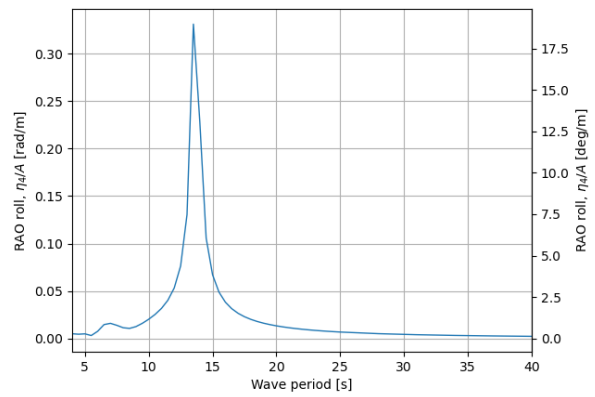
(c) TWA, $\beta_w = 70^\circ$



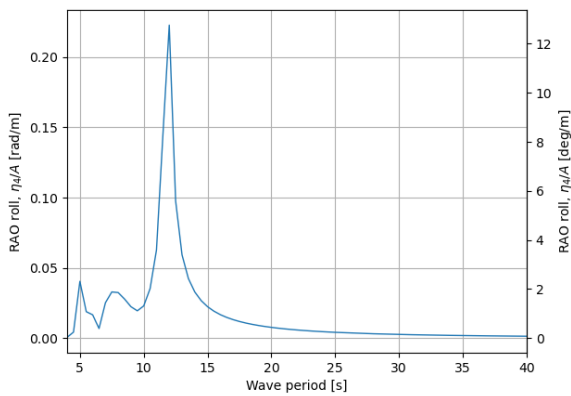
(d) TWA, $\beta_w = 90^\circ$



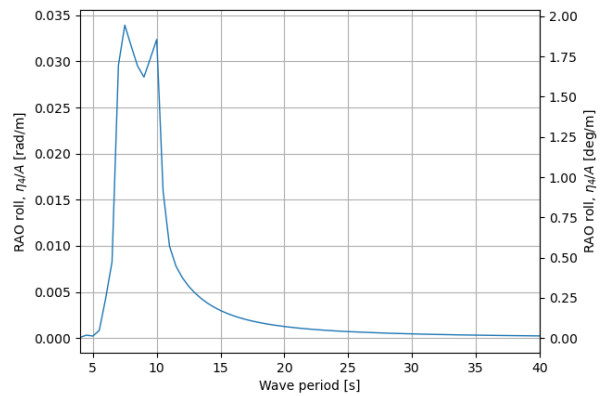
(e) TWA, $\beta_w = 110^\circ$



(f) TWA, $\beta_w = 130^\circ$



(g) TWA, $\beta_w = 150^\circ$



(h) TWA, $\beta_w = 175^\circ$

Figure 7.8: Continued.

Table 7.5: Case summary, including required iterations (iter) for converged solutions.

SS	Case	Iter	Note	
1	1 Flettner SR 2	1		
	2 Flettner SR 2	1		
	4 Flettner SR 2	1		
	1 Flettner SR 4	1	Calculated with both 1 DoF and 2 DoF models	
	2 Flettner SR 4	1	Calculated with both 1 DoF and 2 DoF models	
	4 Flettner SR 4	2	Calculated with both 1 DoF and 2 DoF models	
				150°: stalling in resonance area
	1 wingsail AoA 5°	1	175°: stalling close to resonance area ($T_{\max} = 5.5s$)	Additional calculation with AR 6
	2 wingsail AoA 5°	2	150°: stalling in resonance area	
	4 wingsail AoA 5°	2	150°: stalling in resonance area	
	1 wingsail AoA 10°	1	150° and 175°: stalling in resonance areas	
	2 wingsail AoA 10°	2	130°: stalling close to resonance area ($T_{\max} = 12.0s$)	150° and 175°: stalling in resonance areas
	4 wingsail AoA 10°	2	130°: stalling close to resonance area ($T_{\max} = 12.0s$)	150° and 175°: stalling in resonance areas
	2	1 Flettner SR 2	1	
2 Flettner SR 2		1		
4 Flettner SR 2		1		
1 Flettner SR 4		1		
2 Flettner SR 4		1		
4 Flettner SR 4		1		
1 wingsail AoA 5°		1	175°: stalling close to resonance area ($T_{\max} = 6.5s$)	
2 wingsail AoA 5°		1	175°: stalling close to resonance area ($T_{\max} = 6.5s$)	
4 wingsail AoA 5°		1	175°: stalling close to resonance area ($T_{\max} = 6.5s$)	
1 wingsail AoA 10°		1	175°: stalling in resonance area	
2 wingsail AoA 10°		1	175°: stalling in resonance area	
4 wingsail AoA 10°		1	175°: stalling in resonance area	
3		1 Flettner SR 2	1	
		2 Flettner SR 2	1	
	4 Flettner SR 2	1		
	1 Flettner SR 4	1		
	2 Flettner SR 4	1		
	4 Flettner SR 4	2		
	1 wingsail AoA 5°	1	150°: stalling in resonance area	
	2 wingsail AoA 5°	1	150°: stalling in resonance area	
	4 wingsail AoA 5°	1	150°: stalling in resonance area	
	1 wingsail AoA 10°	1	150° and 175°: stalling in resonance area	
	2 wingsail AoA 10°	1	150° and 175°: stalling in resonance area	
	4 wingsail AoA 10°	1	150° and 175°: stalling in resonance area	

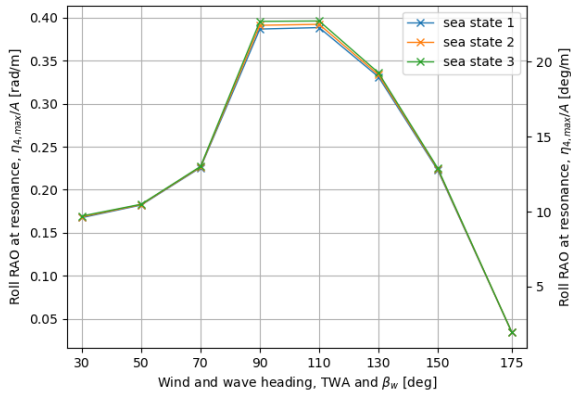


Figure 7.9: Roll RAO at resonance in each sea state.

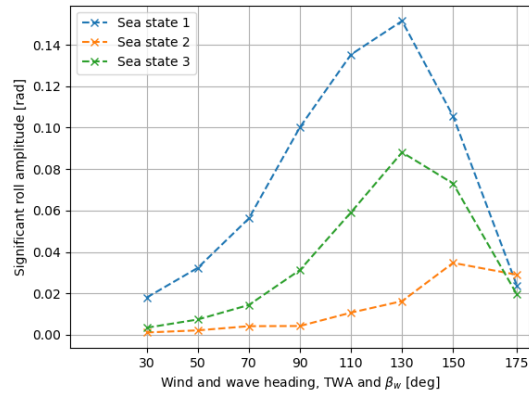


Figure 7.10: Significant roll amplitudes from iteration 0

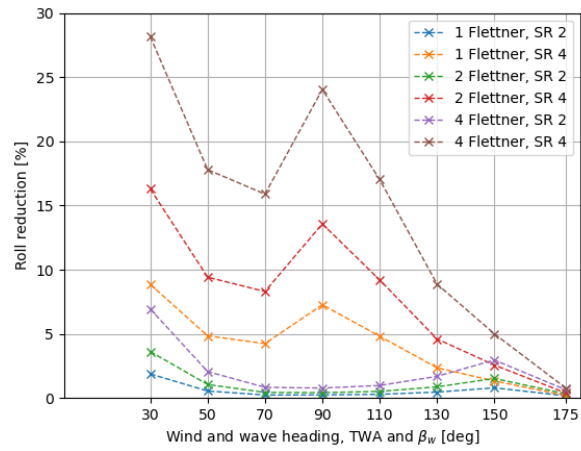
7.3.1 Flettner rotor

The roll reduction of the converged solutions of the Flettner rotor cases in Table 7.5 are presented in Figure 7.11. Figure 7.11a, 7.11b and 7.11c show the results in sea state 1, 2 and 3, respectively. While there are small differences in magnitude of each sea state, the overall shape of reduction curves are equal in all, despite the large differences in significant amplitudes, see Figure 7.10.

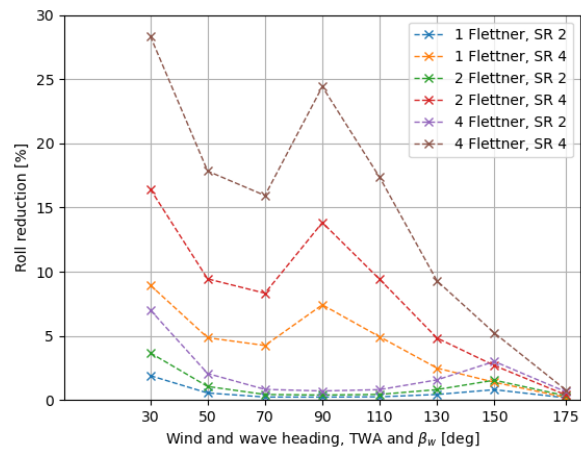
Out of the three cases where the Flettner target SR is set to 4, the roll reduction increase with increasing sea state number at headings up until 130°. However, in general, the significant roll amplitude is smallest in sea state 3 and largest in sea state 1, see Figure 7.10. Even though the roll reduction difference from sea state to sea state is marginal, it may indicate that the potential of roll motion improvement, i.e. the sea state giving the poorest condition in terms of maximum roll of the original hull, is more important than the actual rolling amplitude. The trend does not hold for the cases where the target SR is set to 2, probably due to the very small generated roll damping coefficients at this SR (recall Figure 7.5).

With reference to Figure 7.11a, all cases, i.e. sail configurations, improve the ship roll motion by reducing the roll amplitude at resonance. For a given sail configuration, the improvement is largest at TWA and β_w 30°, but a major improvement is also gained at 90° when the target SR is set to 4. Figure 7.5a showed that B_{44} is quite similar at TWA 70° and 90°. Thus, the aerodynamic damping is more significant in the total wind assisted ship system at 90° than at 70°, due to the smaller hydrodynamic damping at 90°. In other words, the aerodynamic damping improves the well known ship characteristic of poor roll damping in beam sea and wind, Figure 7.9.

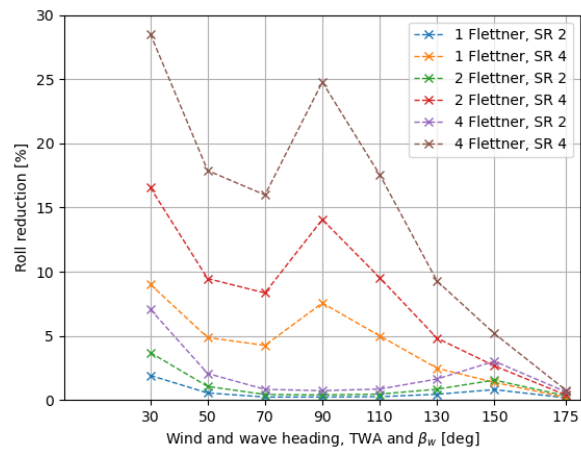
Until now, the results of the pitch motion reduction are unmentioned. The aerodynamic pitch damping is insignificant compared to the hydrodynamic contribution. The maximum pitch reduction is less than 0.02% for all sea states and cases. In some cases or configurations, the sails increase the pitching marginally. However, the maximum pitch amplification is still less than 0.03%. Thus, this negative effect of the rotors can be ignored in a sailing problem due to their positive effect on the roll motion.



(a) Sea state 1



(b) Sea state 2



(c) Sea state 3

Figure 7.11: Roll amplitude reduction at resonance, for the ship fitted with Flettner rotor.

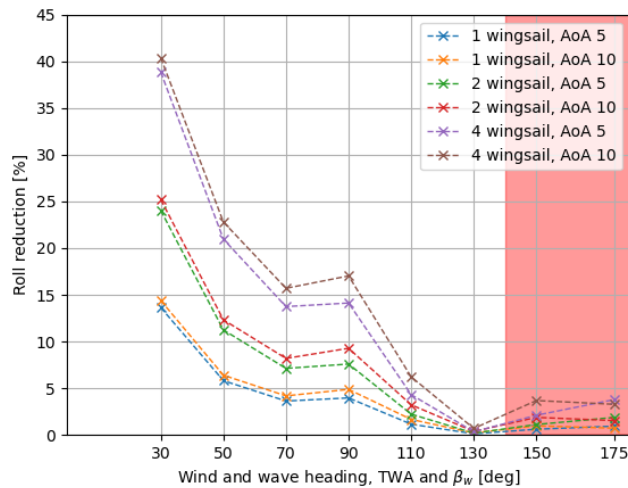
7.3.2 Wingsail

Column 4 of Table 7.5 contains the result of the comparison of stall occurrence (from `stall_info.txt` as described in section 6.3) with the resonance period, Figure 7.8, of the vessel. If stalling occurs outside the resonance area at a specific heading, the response at resonance is still valid and no notation has been made in the table.

Figure 7.12 shows the percentage of roll reduction at resonance according to Equation (7.1) in each representative sea state. The areas of invalid headings due to stalling, corresponding to the notes in Table 7.5, are marked with a red background. The roll reduction results of these headings should not be considered reliable. Earlier, Figure 7.7 indicated that B_{45} can be negative for several TWA, particularly for AWA less or equal to 90° . However, B_{44} is positive, and Figure 7.12 confirms that the ship roll motion reduces significantly in head winds. The roll induced term is dominant in the roll equation of motion, compared to the pitch induced term. The small ship pitch motion limits the impact of the negative B_{45} .

The largest roll reduction out of the tested cases occurs at TWA and β_w 30° , because B_{44} is largest in this heading. At a given positive target AoA, Figure 7.7 previously indicated a decreasing trend of B_{44} for increasing TWA. However, a local maximum of roll reduction is observed in Figure 7.12 at 90° . Although the local maximum is not very prominent, it indicates that the aerodynamic damping improves the poor roll damping of the conventional ship in beam sea, as recently discussed for the Flettner rotor.

Similarly to the Flettner rotor results, the pitch reduction results at resonance are not provided due to the insignificant effect of the sails. Out of all the cases presented in Table 7.5, the largest pitch reduction is only 0.04%. There is no notable effect of pitch motion increase from the wingsails.



(a) Sea state 1

Figure 7.12: Roll amplitude reduction at resonance, for the ship fitted with wingsail.

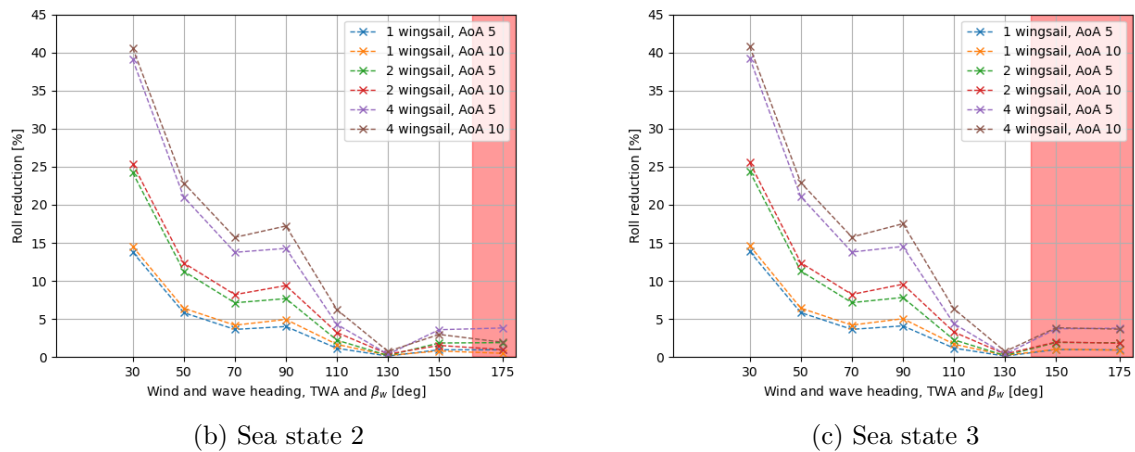
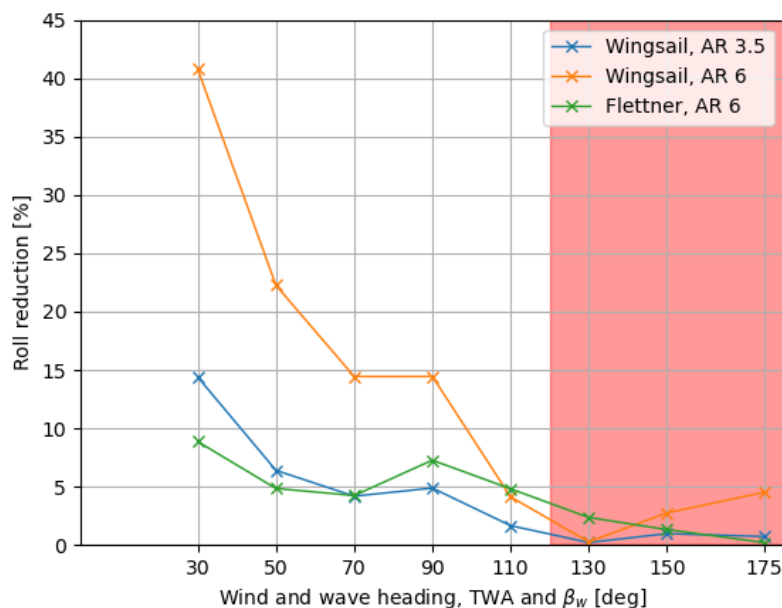


Figure 7.12: Continued.

7.3.3 Wingsail of higher AR

One calculation with a wingsail of AR 6 was performed, with a 60 m height and 10 m chord, for the purpose of comparing the damping with the Flettner rotor when the sails are of equal AR. It is also an interesting addition with respect to the effect of AR and sail height on wingsail damping. The additional calculation of wingsail with higher AR is noted in Table 7.5 at the relevant sail configuration row. Because the earlier results of wingsails with two different trims show that the damping is little affected by the AoA, the current calculation was performed with AoA 5° , to be further away from the static stalling angle. The roll reduction is presented in Figure 7.13, showing the wingsail of AR 3.5 and 6 along with the Flettner rotor of AR 6 and SR 4. The Flettner rotor at SR 2 is not included due to its determined poor damping contribution and little effect on the roll motion.

Figure 7.13: Roll reduction of a Flettner and wingsail of equal AR. The limitation on TWA and β_w with respect to model validity is posed by the AR 6 wingsail.

The problem with stalling for higher wingsails is not as pronounced in this calculation as was initially hypothesised. However, the wingsail does stall in the resonance area for 130° TWA, which is a smaller angle than for the lower AR wingsail. Nevertheless, the higher AR wingsail provides much greater damping than the lower AR wingsail and Flettner rotor. The result will be further discussed in chapter 8.

7.4 One versus two degrees of freedom model

To check the importance of a two degrees of freedom (2 DoF) aerodynamic model, the three Flettner rotor cases with SR 4 was computed again with a 1 DoF model until convergence. The calculations are noted in Table 7.5. The 1 DoF model only includes forced roll motion in the aerodynamic damping model. Hence, the pitch induced term, $B_{45}^{\text{aero}}\dot{\eta}_5$, is omitted in the roll equation of motion, Equation (4.9). The resulting RAO of the wind assisted ship is plotted with the results of the original 2 DoF model in Figure 7.14. The results are similar to such a degree that it is hard to observe any differences in the graphs. The largest relative difference of the two models, around 1.2%, occurs at TWA and β_w equal to 30° for the 4 Flettner rotors case. This is expected, as pitch motion becomes more pronounced in head seas. However, within the scope of this work, the error related to using a 1 DoF model instead of a 2 DoF model would have been acceptable.

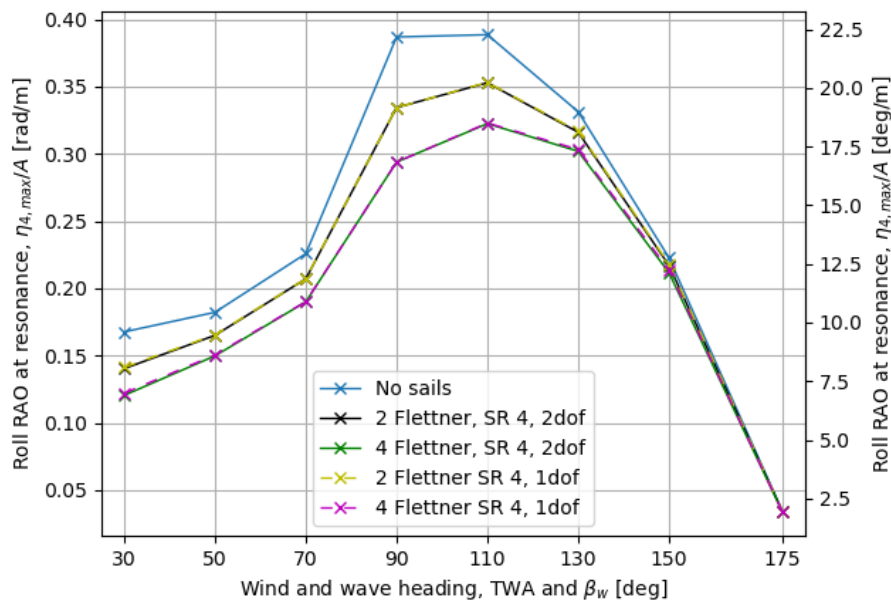


Figure 7.14: Roll RAO at resonance computed by 1 DoF model (roll) and 2 DoF model (roll and pitch).

7.5 Percentage of wind assistance

Table 7.6 to Table 7.11 present the percentage of wind assistance (WA) of each case in Table 7.5. This percentage describes the amount of required propulsion thrust that is generated from the sails. In the case of Flettner rotors, the data in parentheses in Table 7.6 to Table 7.8 include the required power input. These values are more relevant when considering the actual benefits of WAPS in terms of power or fuel savings. However, disregarding the power input provides the quantified thrust importance of the sails.

For the wind assisted ship with Flettner rotors, Table 7.6 to 7.8 show that sailing at TWA 30° requires more input power than what is gained in sail thrust at SR of 4. The WA percentages are negative. Furthermore, a completely wind propelled ship is obtained with four rotors in TWA 90° and 110°. These are however very favourable wind conditions and the WA is smaller in head and following wind.

If the ship is fitted with wingsails, Table 7.9 to 7.11 show that a much lower WA is obtained compared to the Flettner rotor cases. However, one must keep in mind that the AR are different in the two sail cases. Furthermore, the wingsail model of chapter 4 is simple. In reality, a more efficient sail would be constructed, with e.g. flaps to provide higher lift.

Table 7.6: WA [%] of ship with Flettner rotors. Numbers in parenthesis include required input power. Sea state 1.

Case	30°	50°	70°	90°	110°	130°	150°	175°
1 Flettner SR 2	2.69 (1.75)	7.72 (6.88)	12.1 (11.37)	15.24 (14.64)	15.13 (14.72)	10.72 (10.51)	6.45 (6.35)	1.71 (1.67)
2 Flettner SR 2	5.37 (3.49)	15.45 (13.77)	24.20 (22.73)	30.49 (29.29)	30.26 (29.44)	21.44 (21.02)	12.89 (12.7)	3.42 (3.33)
4 Flettner SR 2	10.74 (6.99)	30.9 (27.53)	48.40 (45.47)	60.97 (58.57)	60.52 (58.88)	42.87 (42.04)	25.79 (25.40)	6.84 (6.67)
1 Flettner SR 4	1.77 (-5.88)	11.64 (4.79)	20.38 (14.41)	26.97 (22.09)	27.63 (24.29)	20.11 (18.42)	12.48 (11.69)	3.74 (3.39)
2 Flettner SR 4	3.55 (-11.76)	23.29 (9.58)	40.77 (28.82)	53.94 (44.18)	55.26 (48.58)	40.22 (36.83)	24.97 (23.38)	7.49 (6.77)
4 Flettner SR 4	7.09 (-23.52)	46.58 (19.16)	81.53 (57.64)	107.88 (88.36)	110.52 (97.15)	80.44 (73.66)	49.94 (46.77)	14.98 (13.55)

Table 7.7: WA [%] of ship with Flettner rotors. Numbers in parenthesis include required input power. Sea state 2.

Case	30°	50°	70°	90°	110°	130°	150°	175°
1 Flettner SR 2	3.09 (2.01)	8.36 (7.45)	11.95 (11.23)	14.4 (13.84)	14.62 (14.23)	10.59 (10.38)	6.36 (6.27)	1.65 (1.60)
2 Flettner SR 2	6.19 (4.02)	16.73 (14.90)	23.91 (22.46)	28.81 (27.68)	29.25 (28.45)	21.18 (20.77)	12.72 (12.53)	3.29 (3.21)
4 Flettner SR 2	12.37 (8.05)	33.45 (29.81)	47.81 (44.91)	57.62 (55.35)	58.5 (56.91)	42.35 (41.53)	25.45 (25.06)	6.59 (6.42)
1 Flettner SR 4	2.04 (-6.77)	12.61 (5.19)	20.13 (14.23)	25.49 (20.87)	26.7 (23.47)	19.87 (18.19)	12.32 (11.54)	3.61 (3.26)
2 Flettner SR 4	4.09 (-13.54)	25.22 (10.37)	40.27 (28.47)	50.97 (41.75)	53.41 (46.94)	39.73 (36.39)	24.64 (23.07)	7.21 (6.52)
4 Flettner SR 4	8.17 (-27.09)	50.44 (20.75)	80.54 (56.93)	101.95 (83.49)	106.82 (93.88)	79.46 (72.77)	49.28 (46.15)	14.42 (13.05)

Table 7.8: WA [%] of ship with Flettner rotors. Numbers in parenthesis include required input power. Sea state 3.

Case	30°	50°	70°	90°	110°	130°	150°	175°
1 Flettner SR 2	3.02 (1.97)	8.54 (7.61)	12.87 (12.09)	15.36 (14.76)	14.68 (14.28)	10.32 (10.12)	5.96 (5.87)	1.51 (1.47)
2 Flettner SR 2	6.04 (3.93)	17.08 (15.22)	25.73 (24.18)	30.72 (29.52)	29.35 (28.56)	20.63 (20.23)	11.91 (11.73)	3.01 (2.94)
4 Flettner SR 2	12.09 (7.86)	34.16 (30.44)	51.47 (48.35)	61.45 (59.03)	58.71 (57.11)	41.27 (40.47)	23.82 (23.46)	6.03 (5.87)
1 Flettner SR 4	2.0 (-6.62)	12.88 (5.3)	21.68 (15.32)	27.18 (22.26)	26.8 (23.56)	19.36 (17.73)	11.53 (10.8)	3.3 (2.98)
2 Flettner SR 4	3.99 (-13.23)	25.75 (10.59)	43.35 (30.65)	54.36 (44.52)	53.61 (47.12)	38.71 (35.45)	23.07 (21.60)	6.60 (5.97)
4 Flettner SR 4	7.98 (-26.47)	51.5 (21.19)	86.71 (61.3)	108.72 (89.04)	107.21 (94.24)	77.43 (70.91)	46.14 (43.21)	13.19 (11.93)

Table 7.9: WA [%] of ship with wingsails. Sea state 1.

Case	30°	50°	70°	90°	110°	130°	150°	175°
1 wingsail AoA 5°	0.88	1.48	1.99	2.32	2.18	1.48	0.84	0.15
2 wingsail AoA 5°	1.75	2.97	3.98	4.63	4.35	2.95	1.69	0.30
4 wingsail AoA 5°	3.51	5.94	7.97	9.27	8.7	5.91	3.37	0.60
1 wingsail AoA 10°	1.65	2.87	3.89	4.55	4.29	2.91	1.66	0.31
2 wingsail AoA 10°	3.29	5.74	7.79	9.11	8.58	5.83	3.33	0.63
4 wingsail AoA 10°	6.58	11.48	15.58	18.21	17.16	11.65	6.66	1.26

Table 7.10: WA [%] of ship with wingsails. Sea state 2.

Case	30°	50°	70°	90°	110°	130°	150°	175°
1 wingsail AoA 5°	1.01	1.61	1.97	2.19	2.1	1.46	0.83	0.14
2 wingsail AoA 5°	2.02	3.22	3.93	4.38	4.19	2.92	1.66	0.29
4 wingsail AoA 5°	4.04	6.43	7.87	8.75	8.38	5.83	3.32	0.57
1 wingsail AoA 10°	1.90	3.11	3.85	4.30	4.14	2.88	1.64	0.30
2 wingsail AoA 10°	3.79	6.22	7.69	8.6	8.29	5.76	3.28	0.60
4 wingsail AoA 10°	7.58	12.43	15.39	17.2	16.57	11.51	6.56	1.21

Table 7.11: WA [%] of ship with wingsails. Sea state 3.

Case	30°	50°	70°	90°	110°	130°	150°	175°
1 wingsail AoA 5°	0.99	1.64	2.12	2.33	2.11	1.42	0.78	0.13
2 wingsail AoA 5°	1.97	3.28	4.24	4.67	4.22	2.84	1.55	0.26
4 wingsail AoA 5°	3.95	6.57	8.48	9.34	8.44	5.68	3.11	0.52
1 wingsail AoA 10°	1.85	3.17	4.14	4.59	4.16	2.8	1.54	0.28
2 wingsail AoA 10°	3.70	6.35	8.28	9.18	8.33	5.61	3.07	0.55
4 wingsail AoA 10°	7.41	12.7	16.57	18.35	16.65	11.21	6.14	1.11

Chapter 8

Discussion

As stated in the introduction of this thesis, the relationship between a wind assisted ship's generated thrust and seakeeping abilities is of interest, with the world's increasing motivation for decarbonisation solutions. This chapter endeavours to discuss the separate results of chapter 7 as parts of a larger picture.

In hydrodynamics, roll and pitch are uncoupled degrees of freedom for a body with lateral symmetry. In the aerodynamic system of sails, the work of this thesis shows that the degrees of freedom are highly coupled. Although there are differences depending on the sail system and wind direction, the coupled damping coefficients are significant and sometimes even larger than the decoupled coefficients. However, the wind assisted ship becomes a hydrodynamic and aerodynamic system as the individual systems are superimposed. Due to the inherently small pitch motions of the SOBC-1, the results of this study indicate that the total system can still be considered decoupled. The coupling term in roll is insignificant and a one degree of freedom model is therefore sufficient. This happens even though B_{45} is in fact larger than B_{44} for Flettner rotors. The positive consequence is that the negative pitch induced damping effects observed from wingsails have an insignificant effect on the wind assisted ship.

In the strictly aerodynamic sail system, a conflict between thrust and damping is observed in selected motions, also discussed in previous studies (Satchwell, 1986; Sinclair, 1991). Sail induced damping might therefore be a motivation for voluntary speed loss in ship operation.

Through the results of chapter 7, it is shown that the damping characteristics of the two sail systems differ from each other. One of the differences is the significance of the lift and thrust generating parameters, i.e the AoA or SR, on damping. The wingsail cases show that the AoA has little effect on damping and it is rather the number of sails that determine damping magnitude and roll reduction. For Flettner rotors, damping is highly dependent upon the SR, in addition to the number of sails. The cases with target SR 2 show that no useful damping is provided for low or moderate SR. The reason for this inherent difference between the sail systems is likely caused by the force coefficient's dependency on wind velocity and angle. AWS_U can vary significantly over an encounter period and while the wingsail force coefficients are unaffected by the velocity, the coefficients of the Flettner rotor are not. The opposite can be said regarding the AWA_U ; the wingsail force coefficients are highly dependent upon the wind angle, while the Flettner rotor coefficients are not.

Another difference of the damping characteristics of the sails is the dominant damping mech-

anism. Wingsails are high-lift devices and the damping is observed to be mainly produced by lift. However, in conditions where the drag is directed in the sway direction, it also contributes to damping. The isolated aerodynamic analysis showed that the Flettner rotor roll and pitch damping is caused by both the drag and lift forces. However, a brief investigation into the importance of a 2 DoF model versus a 1 DoF was performed. It indicates that the aerodynamic effects of, and on, the ship pitch motion is insignificant in the total wind assisted ship system. This leads to the conclusion that drag is the significant damping mechanism of a Flettner rotor. In close reached wind conditions where lift to a certain degree is aligned with the sway direction, the lift also contributes to damping.

While the sail induced moments are relatively harmonic, stalling significantly disrupts the periodic characteristic of wingsails. Stalling is mostly problematic in following wind where AWS_S is smaller than in head wind. V_R is then a more significant perturbation and causes a large time dependent variation in the unsteady apparent wind angle. The occurrence of stall can lead to a spike-like feature of the aerodynamic moment, which could cause an impulse effect on the ship. However, the work presented here is not focused on the effect of stalling. It must be further investigated in order to determine its effect on ship motions.

The knowledge on the dominant damping mechanisms can be used to construct and use sails that are beneficial with respect to roll damping. Generally, only one geometry per sail system was analysed in this thesis, due to the time-consuming nature of manually performing iterations. Instead, this work focused on the general effects of the sail system. However, beneficial sail features were observed, nevertheless. Since wingsail damping is mainly lift induced, devices that increase the lift generation without leading to stall should improve the damping characteristics. The natural choice falls on high-lift wings with movable flaps. Furthermore, because the horizontal wind velocity induced by the rigid body motion (V_R) increases linearly with sail height, the risk of stalling promotes the use of several shorter wingsails rather than fewer and taller sails.

Maximum roll reduction is obtained in close hauled sailing conditions, TWA 30° , for both sail systems. In this state, the apparent wind speed is large and a significant amount of damping is generated compared to the situation with following wind giving a small apparent wind speed. While the model verification of chapter 5 indicates that the roll damping of wingsails is overestimated, the relative results with respect to wind angle is reliable. In the current analysis, the wind speed is 10 m/s and the ship velocity is 12.5 kn, such that the apparent wind velocity is small in following winds. It leads to small sail forces and low damping. Even with other wind speeds and ship speeds, the apparent wind is always smaller in following winds than head winds, such that observed trend is applicable to other ship and wind velocity conditions.

While the damping benefits are large in head seas, it is commonly known that operating Flettner rotors in such a small wind angle is of no propulsive use. The sails do contribute to thrust, but because of the required input power, the wind assistance percentage with respect to actual power use is negative at TWA 30° . However, rotors could still be used in this condition strictly for the damping benefits, if required. If one reduced the SR to 2, the required input power reduces and the wind propulsion fraction is positive, but the damping benefits are significantly reduced. Similarly, the wingsails are also poor thrust generators in close hauled conditions. However, a negative value of wind assistance percentage is never obtained because wingsails do not require any input power once they have been trimmed to a certain position. If large roll motions were experienced, a common ship operation would be to turn the ship into the waves. With a wind assisted ship, the roll motion will then be even more efficiently damped due to the head wind.

The most critical environment in ship operation and seakeeping with respect to roll motion, is beam wind and waves. Fortunately, the relatively poor damping characteristic of the sails at $AWA_S 90^\circ$ does not coincide with beam waves, i.e. $\beta_w 90^\circ$, due to the ship velocity. With a current ship speed of 12.5 kn, beam apparent wind corresponds to TWA 130° . Thus, Figure 7.12a to 7.12c indicated near-zero roll reduction at this TWA for wingsails. The high lift-to-drag ratio of wingsails means that performance is poorer in roll damping. Actually, because of the large ratio, both forces contribute to damping in beam sea, even though drag is the force directed in the correct (sway) direction. In contrast to the wingsail, the Flettner rotor has a high drag-to-lift ratio, which means that it does dampen the motion at TWA 130° . However, the reduction is still less than at smaller TWA. Thus, at TWA 90° , the aerodynamic roll damping is relatively large because AWA is less than 90° . The poor roll resistance characteristics of the vessel are significantly improved.

Considering the sail effects from a different viewpoint, today's motivation to install sails on a vessel is related to the need to reduce fuel consumption and associated greenhouse gas emissions. In this context, motion damping effects are a welcome secondary benefit. The largest motion damping result of the wingsail cases investigated was observed with four wingsails with AoA 10° . This sail configuration corresponded to a WA percentage of around 17% in beam winds, depending on the sea state. The Flettner rotor tested has a higher AR than the wingsail, 6 and 3.5, respectively. Thus, a direct comparison is not possible. However, to obtain equal WA percentage, the results show that one Flettner rotor at SR 4 is sufficient. The WA around 20%, so strictly speaking, a smaller SR is enough to equalise the wingsail thrust. Nevertheless, the corresponding observed roll reduction is around 17% and 7% for wingsails and Flettner rotors, respectively. This equals a roll reduction of approximately 1.21% and 1.17% per unit AR. In that sense, for approximately the same fuel benefits, wingsails are better roll motion dampers. The wingsails trialled were modelled conservatively without flaps and assumed an effective AR equal to the geometric AR. Thus, the difference is likely to be even greater in practice.

One calculation was performed with a larger AR wingsail, Figure 7.13, confirming that the higher AR wingsail improves damping compared to the lower AR wingsail. However, resonance area stalling becomes a problem at smaller TWA because of the rigid body motion of the sail top. As indicated earlier in this discussion, one may conclude that smaller aspect ratio wings delay stalling problems and promotes damping, supporting the opinion of Sinclair (1991). However, comparing the high AR wingsail with the Flettner rotor of equal AR in the valid wind angle range shows that the wingsail is superior to the Flettner rotor in all headings but 110° . Here, the apparent wind is close to 90° where the Flettner rotor provides better damping due to the high drag.

On this point, however, one must recall that the AR 6 wingsail is obtained with a height of 60 m, while the AR 6 Flettner rotor is of height 30 m. Since the roll induced sail motion is proportional to sail height, Equation (4.16), the dynamic wind conditions are different at 30 m and 60 m above the deck. In that regard, the comparison of AR 3.5 wingsail and AR 6 Flettner might actually be better, since their heights of 35 m and 30, respectively, are more similar. To quantify the importance of the wingsail height, the maximum roll reduction is 6.8% per unit AR for the AR 6 wingsail, while it is 0.68% per unit AR for the AR 3.5 wingsail.

The aerodynamic moment is greatly affected by the combination of forced motion amplitude, frequency and wind direction. The degree to which the moments can be described by harmonic functions vary. For instance, wingsails can stall in a certain wind direction if the motion, described by the amplitude and frequency, is extreme enough. However, in that same environment

of a certain wind direction and motion frequency, stalling can be avoided if the motion amplitude is sufficiently moderate.

It is physically onerous to investigate all combinations of the parameters affecting the moment generation in a model such as the one created in this work. However, from the cases investigated and the many test runs of code conducted before the final results were produced, the question of whether a linear damping model is reasonable is somewhat answered. The sail induced damping in a wind assisted ship system subject to linear wave theory seems to be relatively well described by a linear damping model, provided highly viscous phenomena such as foil stalling do not occur. The aerodynamic damping is relatively unaffected by small changes in motion amplitude, however, this might not be true for larger amplitudes in a non-linear system.

Finally, observations from this model indicate that the damping varies more depending on the amplitude when the apparent wind angle is large. This leads to an uncertainty to whether the linear damping model is valid. As described earlier, the motion induced horizontal velocity (V_R) is more significant when TWA is large because AWS is relatively small. Additionally, the significant roll amplitudes of the vessel are in general larger for larger wave headings. As this model assumes that true wind is aligned with the wave direction, it further amplifies the wind angle change. A linear model might therefore be more applicable in head winds than following winds, which coincides with the range where the damping is of most importance. Further analysis into this is required before a final conclusion can be drawn.

8.1 Validity of major simplifications

Two large simplifications were assumed in the model. Firstly, interaction effects between sails were disregarded in this preliminary analysis. A simple approach to include the effects is to assume a 5% reduction of the velocity field downstream of a sail (Tillig and Ringsberg, 2020). The maximum observed roll reduction of a single sail was around 10% and 15% for Flettner and wingsail, respectively, leading to an error due to ignored interaction of around 0.5% and 0.75%. Even with a more conservative assumed interaction effect on the sails of 10%, the error is still small in the overall seakeeping problem, compared to the many other simplifications and associated errors of this study. As a preliminary analysis, it is reasonable to disregard this interaction. However, it is suggested that interaction effects are included in future more advanced research, particularly given the potential to trim the sails into a position such that the interaction benefits the motion and lowers the maximum roll angle (Fujiwara, Hearn, Kitamura, and Ueno, 2005).

The second simplification was the dynamic lift, which was also disregarded in the current work. As described in section 3.2.3, the oscillatory motion of a sail can cause a reduction in lift amplitude and a phase shift of the force, leading to an added mass contribution. In TWA and β_w 90, the roll resonance period is around 16 s, which corresponds to a frequency of 0.40 rad/s. Assuming a ship speed of 12.5 kn and TWS 10 m/s, the steady apparent wind speed is approximately 12 m/s, according to Equation (4.27). Using Equation (3.20), an estimate of the reduced frequency of the 10 m chord wingsail is,

$$k = \frac{0.40 \text{ rad/s} \cdot 10 \text{ m}}{2 \cdot 12 \text{ m/s}} = 0.16. \quad (8.1)$$

Comparing the result with the plotted Theodorsen function of Figure 3.8, it is clear that the wingsail oscillation is of significance. Thus, the effects of dynamic lift on ship motions must be included and investigated further in a more advanced study.

Chapter 9

Conclusions

Within ship hydrodynamics for a body of lateral symmetry, the roll and pitch motions are decoupled degrees of freedom. The results of this work show that the sails are highly coupled systems. However, the superposed system of the aerodynamic sail and hydrodynamic vessel model can still be considered decoupled, even for a ship driven entirely by wind with Flettner rotors. Results indicate that the pitch coupling term in the roll equation of motion is insignificant due to small vessel responses in pitch. Furthermore, the aerodynamic contribution to the ship pitch motion is negligible due to dominant hydrodynamic terms, confirming the hypothesis of Satchwell (1986). A one degree of freedom aerodynamic model in roll is therefore sufficient.

The Flettner rotor and wingsail have different damping characteristics, summarised in the following:

1. The wingsail damping is relatively insensitive to the specific angle of attack, while the Flettner rotor damping is highly sensitive to the spin ratio.
2. The wingsail force generation is sensitive to the angle of attack, causing the device to provide more damping than the Flettner rotor which is not sensitive to it. It is thought that this can be generalised to other sail technologies that are sensitive or insensitive to the inflow angle.
3. The wingsail is a high-lift device where useful damping is mainly produced by lift. The high drag-to-lift ratio of the Flettner rotor causes useful damping to originate from the drag. In this context, the term *useful* refers to situations where aerodynamic damping provides significant roll damping to wind assisted vessels. Thus,
 - (a) the wingsail is a better damper in close hauled wind, as lift is mainly directed in the sway direction,
 - (b) the Flettner rotor is a better damper in beam winds, where the drag is mainly directed in the sway direction.
4. The risk of stalling makes the wingsail less capable as a damper in beam following winds, while the Flettner rotor still provides some useful damping.

The largest benefits of damping with respect to roll reduction are achieved in close hauled

winds, independent of the specific sail system. The high apparent wind velocity leads to large sail forces causing large damping. In following winds, the apparent wind speed is small and likewise, so are the forces and damping. However, due to the poor roll damping characteristic of a conventional ship in beam waves, greater damping benefits are achieved in beam wind and waves (90°) compared to slightly smaller wind and wave headings (70°). This is particularly prominent with Flettner rotors.

Due to the sensitivity to wind angle, a single tall wingsail provides greater damping benefits than two shorter wingsails with the same total sail area. Thus, two oppositely motivating forces are observed in the question of what is the best wingsail number and dimension. On the one hand, stalling is a problem that motivates the use of several shorter wingsails rather than fewer high sails. On the other hand, the rigid body induced sail motion increases with sail height, increasing the damping. Therefore, wingsails should be constructed with high-lift devices that delay the occurrence of stalling, not only for propulsive benefits, but also for optimal damping.

A linear damping model is assumed to be reasonable within the physical assumption of rigid body motions in waves subject to linear wave theory. The main criteria of applicability is that viscous phenomena such as wingsail stall are avoided. In that sense, a linear model is more applicable for Flettner rotor damping than wingsail damping. Furthermore, the model is thought to be more applicable in head winds due to the smaller changes in wind angle, which coincide with the range of most significant damping due to the larger apparent wind velocity.

9.1 Recommendations for future work

The current calculations required manual iterations due to the un-scripted connection between the Python code and ShipX. To increase analysis efficiency and expand to a greater number of problem variables, the calculations must be included in a scripted programme. Such a programme would enable the effect of several variables to be systematically investigated, such as ship velocity, sail dimensions and drift angle.

Two main simplifications related to interaction effects were assumed in this work, which are expected to affect the results. The first one is the assumption of independent and superposable aerodynamic and hydrodynamic systems of the sail and vessel, respectively. Secondly, the interaction effects between several sails are neglected. Including such effects requires more accurate computational methods like CFD, but will provide interesting insights into how sail interactions affect damping. In particular, investigating the potential of sail configuration optimisation for enhanced damping is of interest.

Other acceptable simplifications in this work should be improved in future work. The first one include the calculation of the drift angle in a ship performance and motion analysis. The second improvement is to extend the aerodynamic damping analysis to include dynamic lift and its effect on aerodynamic added mass.

Furthermore, future work should include a study of the manoeuvrability of a wind assisted ship and to combine it with seakeeping, particularly course keeping. Time simulations in a programme like Vessel Simulator (VeSim) from SINTEF Ocean could be performed, paying attention to the possible need to redefine the present IMO manoeuvring requirements for wind assisted ships.

Bibliography

- Abbott, I. H., & von Doenhoff, A. E. (1959). *Theory of wing sections: Including a summary of airfoil data*. Dover Publications.
- Bishop, R. E. D., Parkinson, A. G., & Eatock Taylor, R. (1972). Proceedings of an international symposium on directional stability and control of bodies moving in water (R. E. D. Bishop, A. G. Parkinson, & R. Eatock Taylor, Eds.) [supplementary issue]. *Journal of Mechanical Engineering Science*, 14(7).
- Bøckmann, E. (2015). *Wave propulsion of ship* (Doctoral dissertation). Norwegian University of Science and Technology. Trondheim, Norway.
- Bordogna, G., Muggiasca, S., Giappino, S., Belloli, M., Keuning, J., Huijsmans, R., & van 't Veer, A. (2019). Experiments on a Flettner rotor at critical and supercritical Reynolds numbers. *Journal of Wind Engineering and Industrial Aerodynamics*, 188, 19–29. <https://doi.org/10.1016/j.jweia.2019.02.006>
- Bordogna, G. (2020). *Aerodynamics of wind-assisted ships* (Doctoral dissertation). Delft University of Technology. Delft, The Netherlands.
- Çengel, Y. A., & Cimbala, J. M. (2014). *Fluid mechanics: Fundamentals and applications* (3rd ed. in SI units.). McGraw-Hill.
- Clayton, B. R. (1987). Wind-assisted ship propulsion. *Physics in Technology*, 18(2), 53–60.
- Clayton, B. R., & Sinclair, F. M. (1988). Motion damping of ships fitted with marine aerofoils. *Transactions of the Royal Institution of Naval Architects*, 131, 121–133.
- Copuroglu, H. I., & Pesman, E. (2018). Analysis of Flettner Rotor ships in beam waves. *Ocean Engineering*, 150, 352–362. <https://doi.org/10.1016/j.oceaneng.2018.01.004>
- DNVGL-CG-0130. (2018). *Wave loads* (Class Guideline) [Assessed 13.05.2021]. DNV. Høvik.
- DNV-RP-C25. (2010). *Environmental conditions and environmental loads* (Recommended Practice) [Assessed 13.05.2021]. DNV. Høvik.
- Dykstra Naval Architects. (2020). WASP (Ecoliner) [Assessed 01.03.2021]. <https://www.dykstra-na.nl/designs/wasp-ecoliner/>
- Eggers, R., & Kisjes, A. S. (2019). Seakeeping and manoeuvring for wind assisted ships. *Proceedings of the International Conference on Wind Propulsion*. Royal Institution of Naval Architects.
- Faber, J., Hanayama, S., Zhang, S., Pereda, P., Comer, B., Hauerhof, E., van der Loeff, W. S., Smith, T., Zhang, Y., Kosaka, H., Adachi, M., Bonello, J.-M., Galbraith, C., Gong, Z., Hirata, K., Hummels, D., Kleijn, A., Lee, D. S., Liu, Y., . . . Xing, H. (2020). The Fourth IMO GHG Study [IMO, contracted to CE Delft-led consortium. Available at <https://webaccounts.imo.org>].
- Faltinsen, O. M. (1993). *Sea loads on ships and offshore structures*. Cambridge University Press.
- Fathi, D., & Hoff, J. R. (2004). *ShipX Vessel Responses (VERES) Theory Manual*. MARINTEK A/S. Trondheim, Norway.

- Fathi, D., Ringen, E., Alterskjær, A., & Berget, K. (2021). *User Manual, ShipX Ship Speed and Powering Plug-In*. SINTEF Ocean AS. Trondheim, Norway.
- Fathi, D. E. (2018). *ShipX Vessel Responses (VERES) User's Manual*. SINTEF Ocean AS. Trondheim, Norway.
- Fujiwara, T., Hearn, G. E., Kitamura, F., & Ueno, M. (2005). Sail–sail and sail–hull interaction effects of hybrid-sail assisted bulk carrier. *Journal of Marine Science and Technology*, 10(2), 82–95.
- Fujiwara, T., Hearn, G. E., Kitamura, F., Ueno, M., & Minami, Y. (2005). Steady sailing performance of a hybrid-sail assisted bulk carrier. *Journal of Marine Science and Technology*, 10(3), 131–146.
- Gerritsma, J., & Beukelmann, W. (1972). Analysis of the resistance increase in waves of a fast cargo ship.
- Hoerner, S. F. (1975). *Fluid-dynamic lift: Practical information on aerodynamic and hydrodynamic lift* (H. V. Borst, Ed.). Liselotte A. Hoerner.
- Hollenbach, K. U. (1998). Estimating the resistance and propulsion for single-screw and twin-screw ships. *Schiffstechnik/Ship Technology Research*, 45.
- Holtrop, J., & Mennen, G. G. J. (1982). An approximate power prediction method [NSMB publication. Reprinted from: International shipbuilding progress, 29(335). Marine Technolgy Monthly, Rotterdam - The Netherlands].
- IMO. (2002). *Standards for Ship Manoeuvrability, Resolution MSC.137(76)*.
- IMO. (2018). UN body adopts climate change strategy for shipping [Assessed 05.10.2020]. <http://www.imo.org/en/MediaCentre/PressBriefings/Pages/06GHGinitialstrategy.aspx>
- ITTC. (2017). 1978 ITTC Performance Prediction Method. ITTC recommended procedure [Procedure number 7.5-03-03-01.4].
- ITTC. (2018). Calculation of the weather factor f_w for decrease of ship speed in wind and waves. ITTC - Recommended Procedures and Guidelines [Procedure number 7.5-02-07-02.8].
- Kaltschmitt, M., Streicher, W., & Wiese, A. (2007). Basics of renewable energy supply. In M. Kaltschmitt, W. Streicher, & A. Wiese (Eds.), *Renewable energy: Technology, economics and environment* (pp. 23–102). Springer. https://doi.org/10.1007/3-540-70949-5_2
- Kramer, J., & Steen, S. (2015). Importance of the free surface for the drift-induced forces on a ship-like foil. *18th Numerical Towing Tank Symposium*.
- Kramer, J., & Steen, S. (2021). *Simplified test program for hydrodynamic CFD simulations of wind-powered cargo ships* [Submitted to Elsevier (under review)].
- Kramer, J., Steen, S., & Savio, L. (2016a). Drift forces - Wingsails vs Flettner rotors. *International Conference on High Performance Marine Vehicles*.
- Kramer, J., Steen, S., & Savio, L. (2016b). Experimental study of the effect of drift angle on a ship-like foil with varying aspect ratio and bottom edge shape. *Ocean Engineering*, 121, 530–545. <https://doi.org/10.1016/j.oceaneng.2016.06.004>
- Loukakis, T. A., & Sclavounos, P. D. (1978). Some extensions of the classical approach to strip theory of ship motions, including the calculation of mean added force and moments. *Journal of Ship Research*, 22(1), 1–19.
- Lu, R., & Ringsberg, J. W. (2020). Ship energy performance study of three wind-assisted ship propulsion technologies including a parametric study of the Flettner rotor technology. *Ships and Offshore Structures*, 15(3), 249–258. <https://doi.org/10.1080/17445302.2019.1612544>
- Marchaj, C. A. (2000). *Aero-hydrodynamics of sailing* (3rd ed.). Adlard Coles Nautical.

- MetOceanView. (2021). North sea 0.033° 59.5n 0.6w [Assessed 06.05.2021].
<https://app.metoceanview.com/hindcast/sites/nsea/59.5/-0.6>
- Newman, J. N. (2018). *Marine hydrodynamics*. The MIT Press.
- Norsepower. (2020a). Maersk Pelican [Assessed 22.03.2021].
<https://www.norsepower.com/tanker>
- Norsepower. (2020b). Norsepower Rotor sail technology [Brochure available for download. Assessed 26.03.2021]. <https://www.norsepower.com/download/brochure.pdf>
- Persson, A., Li, D.-Q., Olsson, F., Werner, S., & Dhomé, U. (2019). Performance prediction of wind propulsion systems using 3D CFD and route simulation. *Proceedings of the International Conference on Wind Propulsion*, 19–30.
- Reche, M. (2020). *Performance prediction program for wind-assisted cargo ships* (Master's thesis). Technical University of Denmark. Lyngby.
- Satchwell, C. J. (1986). *Marine aerofoil motion damping and related propulsive benefits* (Ship Science Report No. 27). University of Southampton.
- Sinclair, F. M. (1994). Aerodynamic damping on offshore installations — a comparison of experimental measurements with theory. *Journal of Wind Engineering and Industrial Aerodynamics*, 52, 321–344. [https://doi.org/10.1016/0167-6105\(94\)90057-4](https://doi.org/10.1016/0167-6105(94)90057-4)
- Sinclair, F. M., & Clayton, B. R. (1992). Motion damping of marine aerofoils - a comparison of experimental measurements with theory. *Transactions of the Royal Institution of Naval Architects*, 133, 93–104.
- Sinclair, F. M. (1991). *The motion damping characteristics of wind energy devices* (Doctoral dissertation). University of London. London, UK.
- Steen, S. (2014). *Foil and propeller theory* [Compendium in TMR4220 Naval Hydrodynamics, Vol. UK-2014-80/II]. Kompendieforlaget.
- Steen, S., & Minsaas, K. (2014). *Ship resistance* [Compendium in TMR4220 Naval Hydrodynamics, rev. nov. 2013. ed. Vol. UK-2014-80/IV]. Kompendieforlaget.
- Sukas, O. F., Kinaci, O. K., & Bal, S. (2019). Theoretical background and application of MANSIM for ship maneuvering simulations. *Ocean Engineering*, 192, 106239. <https://doi.org/10.1016/j.oceaneng.2019.106239>
- Tillig, F. (2020). *Simulation model of a ship's energy performance and transportation costs* (Doctoral dissertation). Chalmers University of Technology. Gothenburg, Sweden.
- Tillig, F., & Ringsberg, J. W. (2020). Design, operation and analysis of wind-assisted cargo ships. *Ocean Engineering*, 211. <https://doi.org/10.1016/j.oceaneng.2020.107603>
- van der Kolk, N. (2016). Hydromechanics of wind-assisted ship propulsion: Modeling of hydrodynamic sideforce. *Proceedings of the 24th International HISWA Symposium on Yacht Design and Yacht Construction*.
- Viola, I. M., Sacher, M., Xu, J., & Wang, F. (2015). A numerical method for the design of ships with wind-assisted propulsion. *Ocean Engineering*, 105, 33–42. <https://doi.org/10.1016/j.oceaneng.2015.06.009>
- Wallenius Marine. (2020). Oceanbird [Assessed 03.05.2021].
<https://www.oceanbirdwallenius.com/>
- Windship Technology. (2020). Windship Technology, Technical [Assessed 23.05.2020].
<https://windshiptechnology.com/>
- Yasukawa, H., & Yoshimura, Y. (2015). Introduction of MMG standard method for ship maneuvering predictions. *Journal of Marine Science and Technology*, 20, 37–52. <https://doi.org/10.1007/s00773-014-0293-y>

Appendices

A Python code

All functions except for `fit_sin()` are written by the author of this thesis. In the below Python file, `main()` is the main function which must be run to perform the calculations. This function then calls all other functions in the file.

```
1 """
2 Created on Mon Feb 15 09:58:04 2021
3 @author: ejtranel
4 """
5
6 import numpy as np
7 import math
8 from scipy.integrate import.simps
9 import scipy.optimize
10
11
12 def fit_sin(tt, yy):
13     ''' Fit sin to the input time sequence, and return fitting parameters "amp",
14     "omega", "phase", "offset", "freq",
15     "period" and "fitfunc"
16     OBS. This function is written by an unknown, external author.
17     '''
18     tt = np.array(tt)
19     yy = np.array(yy)
20     ff = np.fft.fftfreq(len(tt), (tt[1]-tt[0])) # assume uniform spacing
21     Fyy = abs(np.fft.fft(yy))
22     guess_freq = abs(ff[np.argmax(Fyy[1:])+1]) # excluding the zero frequency
23     "peak", which is related to offset
24     guess_amp = np.std(yy) * 2.**0.5
25     guess_offset = np.mean(yy)
26     guess = np.array([guess_amp, 2.*np.pi*guess_freq, 0., guess_offset])
27
28     def sinfunc(t, A, w, p, c): return A * np.sin(w*t + p) + c
29     popt, pcov = scipy.optimize.curve_fit(sinfunc, tt, yy, p0=guess, maxfev
30     =5000)
31     A, w, p, c = popt
32     f = w/(2.*np.pi)
33     fitfunc = lambda t: A * np.sin(w*t + p) + c
34     perr = np.sqrt(np.diag(pcov)) # standard deviation of popt (A, T_sail,
35     p, c)
36     return {"amp": A, "omega": w, "phase": p, "offset": c, "freq": f, 'std.dev':
37     perr, "period": 1./f, "fitfunc": fitfunc,
38     "maxcov": np.max(pcov), "rawres": (guess, popt, pcov)}
```

```

36 def windSpeedGrad(TWS10, z):
37     """ This fuction calculates the local velocities at each position z in the
    wind boundary layer"""
38     # Input:    TWS10, scalar, True wind speed at reference height 10 m [m / s]
39     #          z, col vector or scalar, Vertical position of points [m]
40     # Output:   TWS, col vector or scalar, Wind speed at points [m/s]
41     a = 0.11 # Hellmann exponent
42     TWS = TWS10 * (z / 10) ** a
43     return TWS
44
45
46 def apparentWind(tws, TWA, Vws, Vr, dof):
47     """ This function calculates the apparent wind speed and angle according to
    the velocity triangle.
48     Two possible modes: roll and pitch. """
49     # Input:    tws, col vector or scalar, Local true wind speed [m/s]
50     #          TWA, scalar, Reference true wind angle [rad]
51     #          Vws, scalar, Wind velocity due to ship velocity [m/s]
52     #          Vr, col vector or scalar, Horizontal velocity due to dof [m/s]
53     #          dof, integer (4 or 5), Degree of freedom, roll or pitch
54     # Output:   aws, col vector or scalar, Unsteady apparent wind speed [m/s]
55     #          awa, col vector or scalar, Unsteady apparent wind angle [rad]
56     # If vector: value at wing sail sections. If one variable is a vector, then
    all possible variables must be vectors.
57
58     if dof == 4:
59         if np.isscalar(tws): # tws is a scalar
60             aws_Y = tws * math.sin(TWA) + Vr
61             aws_X = -Vws + tws * math.cos(TWA)
62             aws = math.sqrt(aws_X ** 2 + aws_Y ** 2)
63             awa = np.arctan2(aws_Y, aws_X) # returns an angle in [-pi, pi]
64         else: # tws is a col vector
65             aws = np.zeros_like(tws)
66             awa = np.zeros_like(tws)
67             for i in range(len(tws)):
68                 aws_Y = tws[i] * math.sin(TWA) + Vr[i]
69                 aws_X = -Vws + tws[i] * math.cos(TWA)
70                 aws[i] = math.sqrt(aws_X ** 2 + aws_Y ** 2)
71                 awa[i] = np.arctan2(aws_Y, aws_X)
72         else: # dof == 5:
73             if np.isscalar(tws): # tws is a scalar
74                 aws_Y = tws * math.sin(TWA)
75                 aws_X = -Vws + tws * math.cos(TWA) - Vr
76                 aws = math.sqrt(aws_X ** 2 + aws_Y ** 2)
77                 awa = np.arctan2(aws_Y, aws_X) # returns an angle in [-pi, pi]
78             else: # tws is a col vector
79                 aws = np.zeros_like(tws)
80                 awa = np.zeros_like(tws)
81                 for i in range(len(tws)):
82                     aws_Y = tws[i] * math.sin(TWA)
83                     aws_X = -Vws + tws[i] * math.cos(TWA) - Vr[i]
84                     aws[i] = math.sqrt(aws_X ** 2 + aws_Y ** 2)
85                     awa[i] = np.arctan2(aws_Y, aws_X)
86         return aws, awa
87
88
89 def evalDOF(beta, d_eta, Vws, dof, h_mwl, TWS10, TWA10, tws):
90     """ This function calculates the apparent wind speed and angle when the ship
    is subject to roll or pitch motion.
91     Only 1 dof is assumed each time. """
92     # Inputs      beta, scalar, Ship drift angle [rad]

```



```

93 #         d_eta, 1 x m array, Rigid body velocity [rad/s]
94 #         Vws, scalar, Wind velocity due to ship velocity [m/s]
95 #         dof, integer (4 or 5), Degree of freedom
96 #         h_mwl, N x 1 array, Height of sail sections above MWL [m]
97 #         TWS10, scalar, Reference true wind velocity at z = 10m [m/s]
98 #         TWA10, scalar, Reference true wind angle at z = 10m [rad]
99 #         tws, N x 1 array, True wind speed over the sail height
100 # Outputs   aws, N x m array, Apparent wind speed
101 #           awa, N x m array, Apparent wind angle
102 #           AWS10, 1 x m array, AWS at ref height [m/s]
103 #           AWA10, 1 x m array, AWA at ref height [rad]
104
105 # Calculating relative velocity (Vr) based on dof:
106 if dof == 4: # roll:
107     Vr_10 = d_eta * 10 * math.cos(beta) # Reference Vr at 10 m above MWL
108     Vr_sec = np.multiply(h_mwl, d_eta) * math.cos(beta)
109 else: # pitch:
110     Vr_10 = - d_eta * 10 * math.cos(beta)
111     Vr_sec = - np.multiply(h_mwl, d_eta) * math.cos(beta)
112
113 # Create empty arrays:
114 AWS10 = np.zeros_like(d_eta) # reference AWS [m/s]
115 AWA10 = np.zeros_like(d_eta) # reference AWA [rad]
116 aws = np.zeros((len(h_mwl), len(d_eta))) # local AW speed [m/s]
117 awa = np.zeros_like(aws) # local AW angle [rad]
118
119 for i in range(len(d_eta)): # iterate through 1 to m.
120     AWS10[i], AWA10[i] = apparentWind(TWS10, TWA10, Vws, Vr_10[i], dof)
121     awsi, awai = apparentWind(tws, TWA10, Vws, Vr_sec[:, i], dof)
122     aws[:, i] = awsi.reshape(1, -1)
123     awa[:, i] = awai.reshape(1, -1)
124 return aws, awa, AWS10, AWA10
125
126
127 def wingsail_coeff(incl_stall, awa, asp, targetAoA):
128     """ This function calculates the lift and drag coefficients of a wingsail as
129     a function of height and time.
130     It corrects for 3D effects by assuming an elliptical lift distribution. """
131     # Inputs:   incl_stall, integer (0 or 1), Include stall, false or true
132     #         awa, N x m array, Local apparent wind speed [m/s]
133     #         asp, scalar, Aspect ratio of sail [-]
134     #         targetAoA, scalar, Target angle of attack [rad]
135     # Outputs: Cl, N x m array, Sectional lift coefficient [-]
136     #         Cd, N x m array, Sectional drag coefficient [-]
137     #         AoA_corr, N x m array, Corrected angle of attack [rad]
138     #         stall_occur, boolean, Indicating whether stall occurs
139
140     # Trim the sail.
141     # If AWA alternates about 180 degrees, the negative angles must be accounted
142     # for as angles > 180
143     trim = np.mean(np.where(awa < -np.pi / 2, awa + 2 * np.pi, awa)) - targetAoA
144
145     AoA = awa - trim
146     # correct AoA if AWA is negative to ensure correct value of lift
147     AoA_corr = np.where((awa > -np.pi / 2) & (awa < 0), -AoA, AoA)
148     AoA_corr = np.where(awa < -np.pi / 2, -(2 * np.pi + AoA), AoA_corr)
149
150     alpha_stall = np.deg2rad(20) # stall angle of 2D foil [rad]
151
152     Cl_stall = 0.5 # 2D lift coefficient after stall
153     Cd_viscous = 0.01 # 2D viscous drag coefficient before stall

```

```

152 Cd_stall = 2 # 2D viscous drag coefficient after stall
153 if incl_stall == 0: # linear foil theory
154     Cl_2D = 2 * np.pi * AoA_corr
155     Cdv_2D = np.ones_like(Cl_2D) * Cd_viscous
156     stall_occur = 0
157 else: # incl_stall == 1:
158     Cl_2D = np.where(abs(AoA_corr) <= alpha_stall, 2 * np.pi * AoA_corr,
159 Cl_stall * (AoA_corr / abs(AoA_corr)))
160     Cdv_2D = np.where(abs(AoA_corr) <= alpha_stall, Cd_viscous, Cd_stall)
161     stall_occur = np.sum(np.where(abs(AoA_corr) > alpha_stall, 1, 0))
162     if stall_occur > 0:
163         stall_occur = 1
164
165 # Corrections for 3D effects
166 Cl = Cl_2D / (1 + 2 / asp)
167 Cdi = np.power(Cl, 2) / (np.pi * asp) # induced drag
168 Cd = Cdv_2D + Cdi # total drag
169 return Cl, Cd, AoA_corr, stall_occur
170
171 def flettner_coeff(d, aws, asp, target):
172     """ This function calculates the lift and drag coefficients of a Flettner
173     rotor as a function of height and time.
174     The empirical formula is based on Tillig (2020) valid for asp of 6 and and
175     with an end plate twice the diameter of
176     the rotor. """
177     # Inputs: d, scalar, Rotor diameter [m]
178     #          aws, N x m array, Local apparent wind speed [m/s]
179     #          asp, scalar, Aspect ratio of sail [-]
180     #          target, scalar, Target SR of rotor [-]
181     # Outputs: RPM, scalar, RPM of rotor, based on input target AoA
182     #           sr, N x m array, Local spin ratio
183     #           Cl, N x m array, Sectional lift coefficient [-]
184     #           Cd, N x m array, Sectional drag coefficient [-]
185     #           Cp, N x m array, Sectional power coefficient [-]
186
187     if asp != 6:
188         print('OBS. Flettner AR is not 6. Empirical formulae for force
189 coefficients might not be valid')
190
191     w = target * np.mean(aws) / (d / 2) # required angular speed [rad/s]
192     RPM = w / (2 * np.pi / 60) # RPM of Flettner rotor at current
193 run
194     sr = (w * d / 2) / aws # local spin ratio [-]
195     SR_corr = np.where(sr > 6, 6, sr)
196
197     # drag coefficient function: Tillig (AoA 0-6) + extrapolation (AoA > 6)
198     def dragcoeff(SR):
199         drag_coeff = -0.0017 * np.power(SR, 5) + 0.0464 * np.power(SR, 4) -
200 0.4424 * np.power(SR, 3) + \
201 1.7243 * np.power(SR, 2) - 1.641 * SR + 0.6375
202         return drag_coeff
203
204     points = np.linspace(5, 6, 3)
205     z = np.polyfit(points, dragcoeff(points), 1)
206     Cd_extrap = np.poly1d(z)
207
208     Cl = -0.0046 * np.power(abs(SR_corr), 5) + 0.1145 * np.power(abs(SR_corr),
209 4) - 0.9817 * np.power(abs(SR_corr), 3) \
210 + 3.1309 * np.power(abs(SR_corr), 2) - 0.1039 * abs(SR_corr)
211     Cd = np.where(sr < 6, dragcoeff(abs(sr)), Cd_extrap(sr))

```

```

206 Cp = 0.0001 * np.power(sr, 5) - 0.0004 * np.power(sr, 4) + 0.0143 * np.power
      (sr, 3) - 0.0168 * np.power(sr, 2) +\
207     0.0234 * sr
208
209 # Make Cl negative if rotor rotates in opposite direction such that negative
      lift is generated.
210 Cl = np.where(SR_corr < 0, -Cl, Cl)
211 return RPM, sr, Cl, Cd, Cp
212
213
214 def wingsail_forces(rhoa, c, Cl, Cd, aws, awa):
215     """ This function calculates the driving and heeling forces at each winsail
      section. The lift and drag forces are
216     transformed with respect to the local apparent wind angle """
217     # Inputs:  rhoa, scalar, Density of air [kg/m^3]
218     #           c, scalar, chord length [m]
219     #           Cl, N x m array, Sectional lift coefficient [-]\
220     #           Cd, N x m array, Sectional drag coefficient [-]
221     #           aws, N x m array, Local apparent wind speed [m/s]
222     #           awa, N x m array, Local apparent wind angle [rad]
223     # Outputs: dL, N x m array, Sectional lift force [N/m].
224     #           dD, N x m array, Sectional drag force [N/m]
225     #           dFD, N x m array, Sectional driving force [N/m]
226     #           dFH, N x m array, Sectional heeling force [N/m]
227     #           dFD_lift, dFD_drag, dFH_lift, dFH_drag: the lift and drag
      contributions [N/m] of the above arrays
228
229     # Note: these are 2D forces. Simpson's rule is used for FD and FH in main.py
230     dL = np.multiply(Cl, np.power(aws, 2)) * 0.5 * rhoa * c      # lift [N/m]
231     dD = np.multiply(Cd, np.power(aws, 2)) * 0.5 * rhoa * c      # drag [N/m]\
232
233     dFD_lift = np.zeros_like(dL)      # the contribution of lift to driving force
234     dFD_drag = np.zeros_like(dL)      # the contribution of drag
235     dFD = np.zeros_like(dL)          # driving force [N/m]
236
237     dFH_lift = np.zeros_like(dL)      # the contribution of lift to heeling force
238     dFH_drag = np.zeros_like(dL)      # the contribution of drag
239     dFH = np.zeros_like(dD)          # heeling force [N/m]
240     for i in range(len(dL)):
241         for j in range(len(dL[0])):
242             dFD_lift[i, j] = dL[i, j] * math.sin(abs(awa[i, j]))
243             dFD_drag[i, j] = - dD[i, j] * math.cos(abs(awa[i, j]))
244             dFD[i, j] = dFD_lift[i, j] + dFD_drag[i, j]
245             if awa[i, j] > 0: # awa = [0, pi]
246                 dFH_lift[i, j] = dL[i, j] * math.cos(awa[i, j])
247                 dFH_drag[i, j] = dD[i, j] * math.sin(awa[i, j])
248                 dFH[i, j] = dFH_lift[i, j] + dFH_drag[i, j]
249             else: # awa = [-pi, 0]
250                 dFH_lift[i, j] = - dL[i, j] * math.cos(abs(awa[i, j]))
251                 dFH_drag[i, j] = - dD[i, j] * math.sin(abs(awa[i, j]))
252                 dFH[i, j] = dFH_lift[i, j] + dFH_drag[i, j]
253     return dL, dD, dFD_lift, dFD_drag, dFD, dFH_lift, dFH_drag, dFH
254
255
256 def flettner_forces(rhoa, d, Cl, Cd, Cp, aws, awa):
257     """ This function calculates the sectional driving and heeling force of a
      Flettner rotor. It assumes that the rotor
258     spins in the counter-clock direction. In most cases, the awa is in the range
      [0, pi], giving a lift in the
259     positive X-direction """
260     # Inputs:  rhoa, scalar, Density of air [kg/m^3]

```

```

261 #         d, scalar, rotor diameter [m]
262 #         Cl, N x m array, Sectional lift coefficient [-]
263 #         Cd, N x m array, Sectional drag coefficient [-]
264 #         Cp, N x m array, Sectional power coefficient [-]
265 #         aws, N x m array, Local apparent wind speed [m/s]
266 #         awa, N x m array, Local apparent wind angle [rad]
267 # Outputs: dL, N x m array, Sectional lift force [N/m]
268 #         dD, N x m array, Sectional drag force [N/m]
269 #         dP, N x m array, Sectional power coefficient [J/m]
270 #         dFD, N x m array, Sectional driving force [N/m]
271 #         dFH, N x m array, Sectional heeling force [N/m]
272 #         dFD_lift, dFD_drag, dFH_lift, dFH_drag: the lift and drag
contributions [N/m] of the above arrays
273
274 # Note: these are 2D forces. Simpson's rule is used for FD and FH in main.py
275 dL = np.multiply(Cl, np.power(aws, 2)) * 0.5 * rhoa * d # lift [N/m]
276 dD = np.multiply(Cd, np.power(aws, 2)) * 0.5 * rhoa * d # drag [N/m]
277 dP = np.multiply(Cp, np.power(aws, 3)) * 0.5 * rhoa * d # power [W/m]
278
279 dFD_lift = np.multiply(dL, np.sin(awa)) # the lift's contribution to
driving force
280 dFD_drag = - np.multiply(dD, np.cos(awa)) # the drag's contribution to
driving force
281 dFD = dFD_lift + dFD_drag # driving force [N/m]
282
283 dFH_lift = np.multiply(dL, np.cos(awa))
284 dFH_drag = np.multiply(dD, np.sin(awa))
285 dFH = dFH_lift + dFH_drag # heeling force [N/m]
286 return dL, dD, dP, dFD_lift, dFD_drag, dFD, dFH_lift, dFH_drag, dFH
287
288
289 def shipModel(Vs, eta_a, w, beta_w):
290     """ Data on basic ship geometry, motion and sailing problem """
291     # Input: Vs, Scalar, Ship speed [kn]
292     #         eta_a, Scalar, Roll or pitch amplitude [rad]. Must correspond to
dof
293     #         beta_w, Scalar, Wave heading [rad]. Relative to global X-axis
294     #         w, Scalar, incident wave frequency [rad/s]
295     # Output f, Scalar, Ship freeboard
296     #         Vs_mps, Scalar, Ship velocity converted to [m/s]
297     #         beta, Scalar, Drift angle of ship [rad]
298     #         we, Scalar, Encounter frequency [rad/s]
299     #         d_eta, 1 x m array, Rigid body velocity [rad/s]
300     #         t, 1 x m array, Time [s]
301
302     g = 9.81 # gravitational acceleration [m/s^2]
303     f = 12.5 # ship freeboard [m] (Value from ShipX, SOBC
-1 Design waterline)
304     Vs_mps = knots2mps(Vs) # convert ship speed from knots to m/s [m/s]
305     beta = 5 * np.pi / 180 # drift angle [rad]
306     beta_w = beta_w * np.pi / 180 # convert wave heading to [rad]
307
308     we = w + w ** 2 * Vs_mps * np.sin(beta_w - beta) / g # encounter
frequency [rad/s]
309     Te = 2 * np.pi / we # encounter period [
s]
310     time_step = Te / 100
311     t = np.arange(0, Te + time_step * 0.5, time_step) # time [s]. Number
of time evaluations: m
312     d_eta = -eta_a * we * np.sin(we * t) # pitch or roll
velocity [rad/s] as function of time

```

```

313     return f, Vs_mps, beta, we, d_eta, t
314
315
316 def sailModel(waps):
317     """ Data on sail geometries """
318     # Input:    waps, integer, Wingsail (1) or Flettner rotor (2)
319     # Output:   H, scalar, Height of sail
320     #           c, scalar, Chord length (if waps == 1) or diameter (if waps ==
321     #           2)
322     #           asp, scalar, Sail aspect ratio [-]
323     #           Ap, scalar, Projected sail area [m^2]
324     if waps == 1:    # WINGSAIL. Dimensions, assuming rectangular shape
325         H = 35
326         c = 10
327         asp = H / c
328         Ap = H * c
329     else:           # FLETTNER ROTOR (waps == 2)
330         H = 30
331         c = 5
332         asp = H / c
333         Ap = H * c
334     return H, c, asp, Ap
335
336 def mps2knots(V_mps):
337     """ This function converts a velocity in m/s to knots """
338     V_kn = V_mps / (1852 / 3600)
339     return V_kn
340
341
342 def knots2mps(V_kn):
343     """ This function converts a velocity in knots to m/s """
344     V_mps = V_kn * (1852 / 3600)
345     return V_mps
346
347
348 def main(waps, target, TWA10, Vs, dof, eta_a, incl_stall, w, ABL):
349     """ This function is the main function of the aerodynamic damping model,
350     described in chapter 4 of the thesis """
351     # Inputs:    waps, integer (1 or 2), Wingsail (1) or Flettner rotor (2)
352     #           target, scalar, Target AoA [deg] or SR [-]
353     #           TWA10, scalar, True wind speed [deg] at reference height 10 m
354     #           Vs, scalar, Ship velocity [kn]
355     #           dof, integer (4 or 5), Uncoupled ship degree of freedom. Roll
356     #           (4) or pitch (5)
357     #           eta_a, scalar, Amplitude of relevant rigid body motion
358     #           incl_stall, boolean, Include or ignore sail stall.
359     #           w, scalar, Incident wave frequency [rad/s]
360     #           ABL, boolean, Account for the atmospheric boundary layer in tws
361     if True (1)
362     # OBS. The code is not written to handle wrong inputs. The above
363     alternatives must be adhered to.
364     # Outputs:   Aerodynamic damping coefficients.
365
366     rhoa = 1.21    # air density at 20 degC [kg/m3]
367
368     # - - - - SAILING PROBLEM - - - - -
369     beta_w = TWA10 # TWA10. Assumes wave heading equal to wind heading
370     # Get data on ship geometry and motion
371     f, Vs_mps, beta, we, d_eta, t = shipModel(Vs, eta_a, w, beta_w)
372

```

```

369 # - - - - SAIL MODEL - - - - -
370 H, c, asp, Ap = sailModel(waps)
371 if waps == 2:
372     d = c # rename chord to diameter
373
374 # - - - - DISCRETISATION - - - - -
375 N = 70 # number of wing sections z-direction [-]
376 sw = H / N # section width [m]
377 h = np.arange(0.5 * sw, H, sw).reshape(-1, 1) # height of sail sections [m]
378 h_mwl = h + f # Vertical position of wingsail sections above MWL [m].
379
380 # - - - - WIND MODEL - - - - -
381 TWS10 = 10 # reference TWS [m/s]
382 TWA10 = TWA10 * np.pi / 180 # reference TWA, [rad] in range (-pi, pi)
383 if ABL:
384     tws = windSpeedGrad(TWS10, h_mwl) # local true wind speed [m/s]
385 else:
386     tws = np.ones_like(h_mwl) * TWS10 # ignore ABL. TWA constant in height
387 Vws = -Vs_mps # wind velocity due to ship velocity
388 # Apparent wind from the wind velocity triangle:
389 aws, awa, AWS10, AWA10 = evalDOF(beta, d_eta, Vws, dof, h_mwl, TWS10, TWA10,
390     tws)
391
392 # - - - - FORCE MODEL - - - - -
393 if waps == 1:
394     targetAoA = np.deg2rad(target) # convert target AoA to radians [rad]
395     Cl, Cd, AoA, stall_occur = wingsail_coeff(incl_stall, awa, asp,
396     targetAoA)
397     dL, dD, dFD_lift, dFD_drag, dFD, dFH_lift, dFH_drag, dFH =
398     wingsail_forces(rhoa, c, Cl, Cd, aws, awa)
399 else:
400     RPM, sr, Cl, Cd, Cp = flettner_coeff(d, aws, asp, target)
401     dL, dD, dP, dFD_lift, dFD_drag, dFD, dFH_lift, dFH_drag, dFH =
402     flettner_forces(rhoa, d, Cl, Cd, Cp, aws, awa)
403
404 # Force components in local (x, y) direction:
405 dFy = -dFH * math.cos(beta) + dFD * math.sin(beta)
406 dFx = -dFH * math.sin(beta) + dFD * math.cos(beta)
407 Fx = np.zeros_like(t)
408 Fy = np.zeros_like(t)
409 dFy_lift = -dFH_lift * math.cos(beta) + dFD_lift * math.sin(beta)
410 dFx_lift = -dFH_lift * math.sin(beta) + dFD_lift * math.cos(beta)
411 Fx_lift = np.zeros_like(t)
412 Fy_lift = np.zeros_like(t)
413
414 # Lift and drag contributions to aerodynamic roll and pitch moment
415 dF4_lift = np.multiply(-dFH_lift, h_mwl) * math.cos(beta) + np.multiply(-
416     dFD_lift, h_mwl) * math.sin(beta)
417 dF5_lift = np.multiply(-dFH_lift, h_mwl) * math.sin(beta) + np.multiply(
418     dFD_lift, h_mwl) * math.cos(beta)
419 dF4_drag = np.multiply(-dFH_drag, h_mwl) * math.cos(beta) + np.multiply(-
420     dFD_drag, h_mwl) * math.sin(beta)
421 dF5_drag = np.multiply(-dFH_drag, h_mwl) * math.sin(beta) + np.multiply(
422     dFD_drag, h_mwl) * math.cos(beta)
423 F4_lift = np.zeros_like(t)
424 F4_drag = np.zeros_like(t)
425 F5_lift = np.zeros_like(t)
426 F5_drag = np.zeros_like(t)
427
428 # Aerodynamic roll and pitch moment, sectional [N/m*m]

```

```

421     dF4 = np.multiply(-dFH, h_mwl) * math.cos(beta) + np.multiply(-dFD, h_mwl)*
        math.sin(beta)
422     dF5 = np.multiply(-dFH, h_mwl) * math.sin(beta) + np.multiply(dFD, h_mwl)*
        math.cos(beta)
423
424     F4 = np.zeros_like(t)
425     F5 = np.zeros_like(t)
426     FD = np.zeros_like(t)
427     FH = np.zeros_like(t)
428     P = np.zeros_like(t)
429     # Use Simpson's rule to integrate over the height. Forces [N] and moments [
        Nm].
430     for i in range(len(t)):
431         if waps == 2:
432             P[i] =.simps(dP[:, i].reshape(1, -1), h.reshape(1, -1))
433             FD[i] =.simps(dFD[:, i].reshape(1, -1), h.reshape(1, -1))
434             FH[i] =.simps(dFH[:, i].reshape(1, -1), h.reshape(1, -1))
435             Fx[i] =.simps(dFx[:, i].reshape(1, -1), h.reshape(1, -1))
436             Fy[i] =.simps(dFy[:, i].reshape(1, -1), h.reshape(1, -1))
437             Fx_lift[i] =.simps(dFx_lift[:, i].reshape(1, -1), h.reshape(1, -1))
438             Fy_lift[i] =.simps(dFy_lift[:, i].reshape(1, -1), h.reshape(1, -1))
439             F4_lift[i] =.simps(dF4_lift[:, i].reshape(1, -1), h.reshape(1, -1))
440             F4_drag[i] =.simps(dF4_drag[:, i].reshape(1, -1), h.reshape(1, -1))
441             F5_lift[i] =.simps(dF5_lift[:, i].reshape(1, -1), h.reshape(1, -1))
442             F5_drag[i] =.simps(dF5_drag[:, i].reshape(1, -1), h.reshape(1, -1))
443             F4[i] =.simps(dF4[:, i].reshape(1, -1), h.reshape(1, -1)) # Total roll
        moment [Nm]
444             F5[i] =.simps(dF5[:, i].reshape(1, -1), h.reshape(1, -1)) # Total pitch
        moment [Nm]
445
446     # - - - - LINEAR MODEL; CURVE FIT - - - - -
447     res4 = fit_sin(t, F4)
448     res5 = fit_sin(t, F5)
449
450     # Aerodynamic roll and pitch damping coefficients due to forced motion k.
451     B4k = res4['amp']/(res4['omega']*eta_a)
452     B5k = res5['amp']/(res5['omega']*eta_a)
453
454     return B4k, B5k

```


B ShipX reports of SOBC-1

B.1 Hydrostatics report

HYDROSTATICS	ENCL.	1)
	REPORT	
	DATE	2021-05-29
	REF	

SHIP:
 Loading condition:
 Draught AP/FP:

SOBC-1
 Design WL
 11.000 / 11.000 [m]

	Symbol	Unit	
Length overall	L _{OA}	[m]	199.299
Length betw. perp.	L _{PP}	[m]	190.000
Breadth moulded	B	[m]	32.222
Depth to 1 st deck	D	[m]	23.502
Draught at L _{PP} /2	T	[m]	11.000
Draught at FP	T _{FP}	[m]	11.000
Draught at AP	T _{AP}	[m]	11.000
Trim (pos. aft)	t	[m]	0.000
Rake of keel		[m]	0.000
Rise of floor		[m]	0.000
Bilge radius		[m]	2.000
Sea water density	ρ _s	[kg/m ³]	1025.00
Shell plating thickness		[mm]	2
Shell plating in % of displ.		[%]	0.40
Length on waterline	L _{WL}	[m]	196.942
Breadth waterline	B _{WL}	[m]	32.201
Volume displacement	∇	[m ³]	48927.6
Displacement	Δ	[t]	50351.4
Prismatic coefficient*	C _P	[-]	0.7304
Block coefficient*	C _B	[-]	0.7270
Midship section coefficient	C _M	[-]	0.9954
Longitudinal C.B. from L _{PP} /2	LCB	[m]	4.388
Longitudinal C.B. from L _{PP} /2*	LCB	[% L _{PP}]	2.310
Longitudinal C.B. from AP	LCB	[m]	99.388
Vertical C.B.	VCB	[m]	5.843
Wetted surface	S	[m ²]	8485.24
Wetted surface of transom stern	A _T	[m ²]	2.91
Waterplane area	A _W	[m ²]	5250.39
Waterplane area coefficient	C _W (L _{WL})	[-]	0.828
Longitudinal C.F. from L _{PP} /2	LCF	[m]	-5.942
Longitudinal C.F. from AP	LCF	[m]	89.058
Immersion	DP ₁	[t/cm]	53.817
Trim moment	MT ₁	[t · m/cm]	699.201
Transverse metacenter above keel	KM _T	[m]	13.691
Longitudinal metacenter above keel	KM _L	[m]	264.897

Remarks: *Refers to L_{PP}
 Hydrostatic corrections not included

ShipX (RepGen version 2.0.22) 29-May-2021 11:46:34 - Licensed to: NTNU (NTNU)

B.2 Ship resistance coefficients report

SHIP RESISTANCE COEFFICIENTS	ENCL.	1)
	REPORT	
	DATE	2021-05-29
	REF	

SHIP:
Loading condition:
Draught AP/FP:

SOBC-1
DWL - Design waterline
11.000 / 11.000 [m]

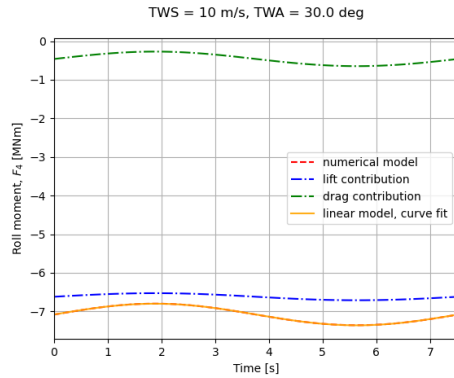
	Symbol	Unit	
Length between perpendiculars	L_{PP}	[m]	190.000
Length on waterline	L_{WL}	[m]	196.942
Breadth moulded	B	[m]	32.201
Mean draught	T	[m]	11.000
Trim (pos. aft)	t	[m]	0.000
Wetted surface of naked hull	S	[m ²]	8485.24
Wetted surface of transom stern	A_T	[m ²]	2.91
Front projected area above WL		[m ²]	800.0
Volume displacement	∇	[m ³]	48927.6
Block coefficient (Lwl)	C_{BLW}	[-]	0.701
<hr/>			
1+k	=	1.0949	Correlation coef $\cdot 10^3$ = -0.2280
$C_{AAS} \cdot 10^3$	=	0.0943	Seawater temp. [°C] = 15.0

METHOD: Hollenbach 98 (average lines)

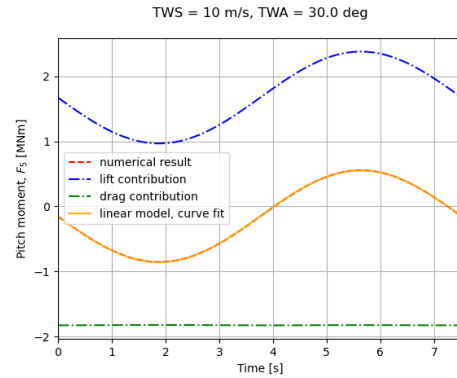
V_S [knots]	V_S [m/s]	F_R [-]	R_{NS} $\cdot 10^{-9}$	C_R $\cdot 10^3$	C_{FS} $\cdot 10^3$	C_{VS} $\cdot 10^3$	C_{BDS} $\cdot 10^3$	C_{APPs} $\cdot 10^3$	C_{TS} $\cdot 10^3$
7.50	3.858	0.088	0.640	0.560	1.619	1.819	0.005	0.043	2.293
10.00	5.144	0.117	0.853	0.390	1.561	1.822	0.005	0.041	2.125
12.50	6.431	0.146	1.066	0.339	1.519	1.823	0.005	0.040	2.074
15.00	7.717	0.176	1.279	0.410	1.485	1.824	0.005	0.039	2.144
17.50	9.003	0.205	1.492	0.603	1.457	1.823	0.005	0.039	2.336

ShipX Ship Speed and Powering Plug-In 13-May-2021 16:07:19 - Licensed to: NTNU (NTNU)

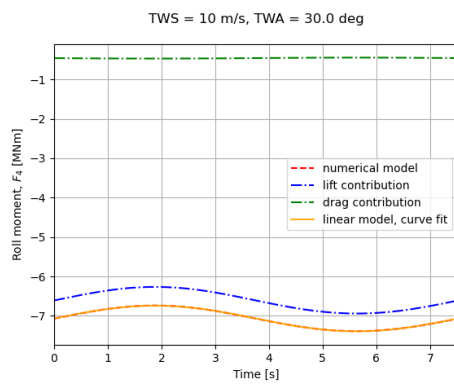
C Flettner rotor induced roll and pitch moments



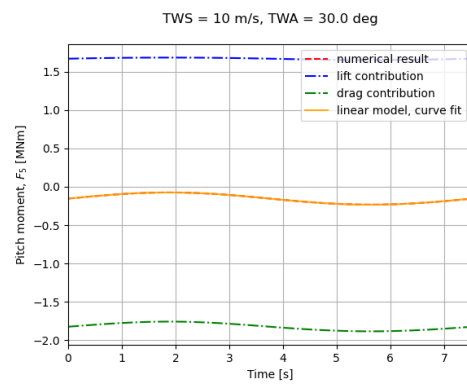
(a) Case 1: Roll induced roll moment



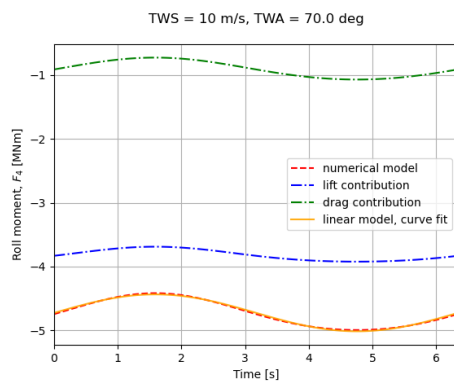
(b) Case 1: Roll induced pitch moment



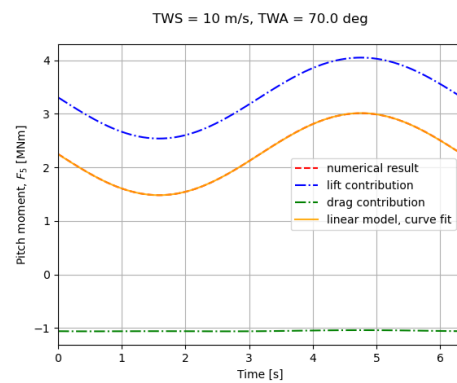
(c) Case 1: Pitch induced roll moment



(d) Case 1: Pitch induced pitch moment

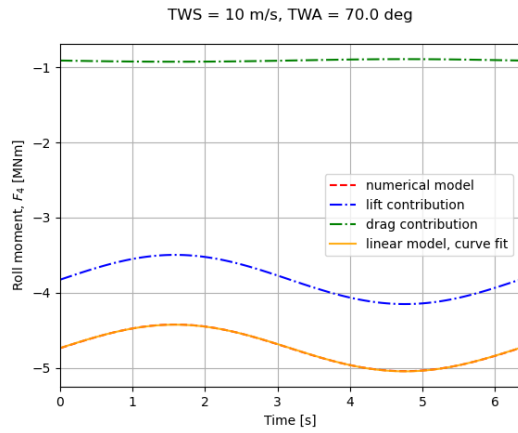


(e) Case 2: Roll induced roll moment

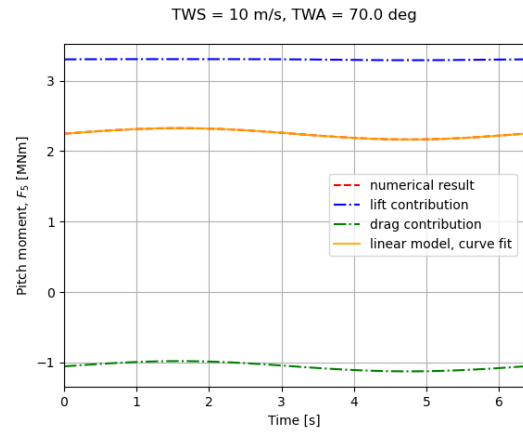


(f) Case 2: Roll induced pitch moment

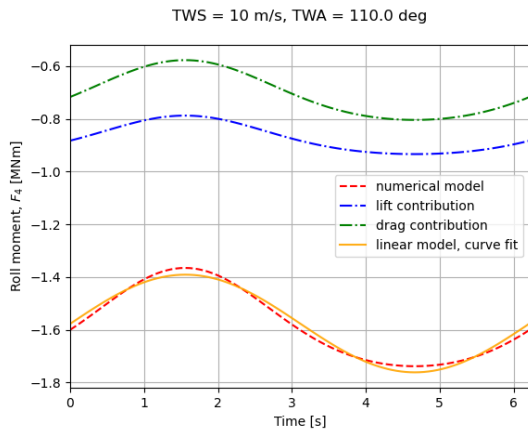
Figure C.1: Flettner rotor damping mechanism evaluation: induced aerodynamic moments



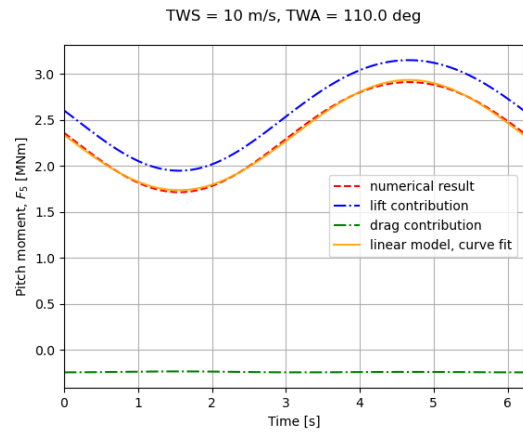
(g) Case 2: Pitch induced roll moment



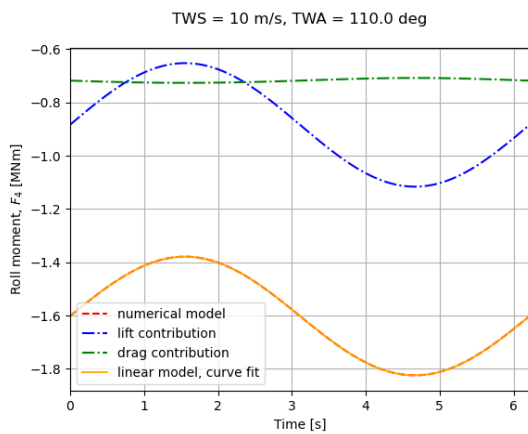
(h) Case 2: Pitch induced pitch moment



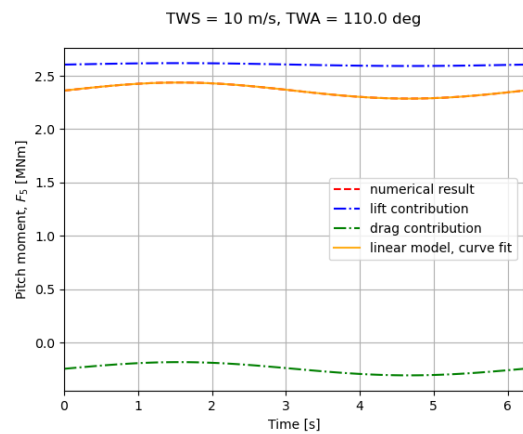
(i) Case 3: Roll induced roll moment



(j) Case 3: Roll induced pitch moment

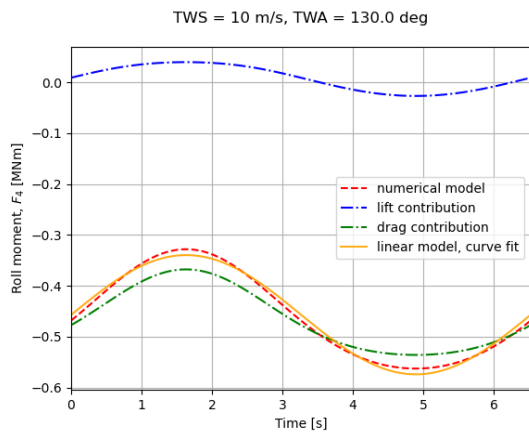


(k) Case 3: Pitch induced roll moment

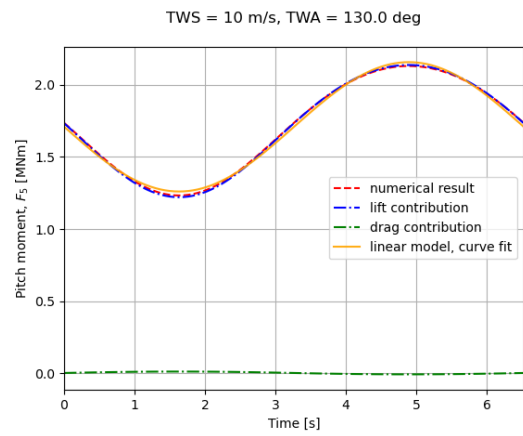


(l) Case 3: Pitch induced pitch moment

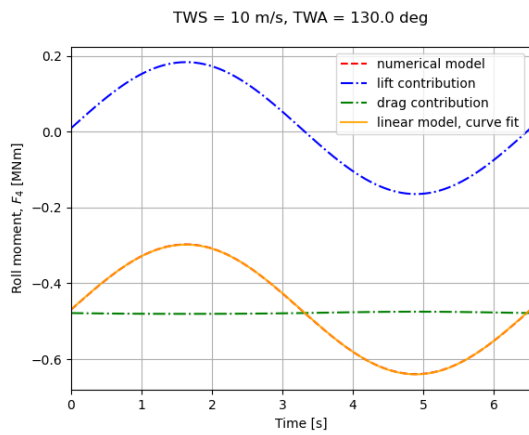
Figure C.1: Continued.



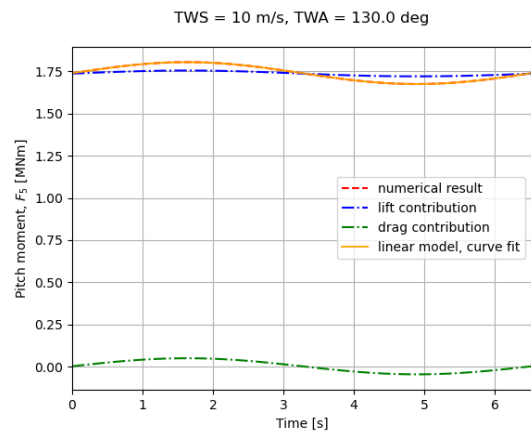
(m) Case 4: Roll induced roll moment



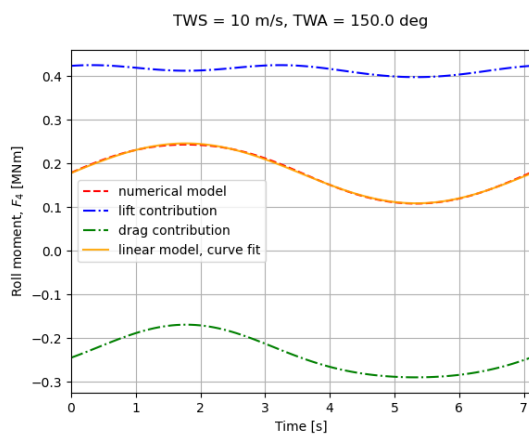
(n) Case 4: Roll induced pitch moment



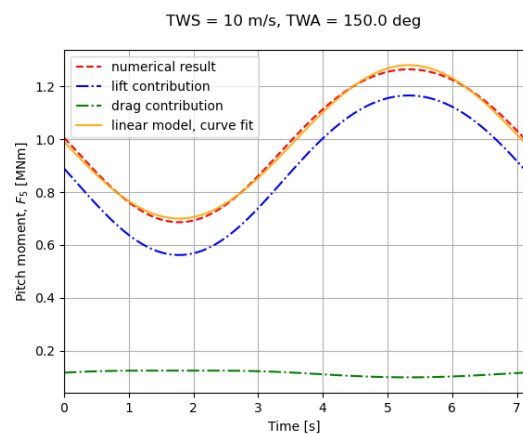
(o) Case 4: Pitch induced roll moment



(p) Case 4: Pitch induced pitch moment

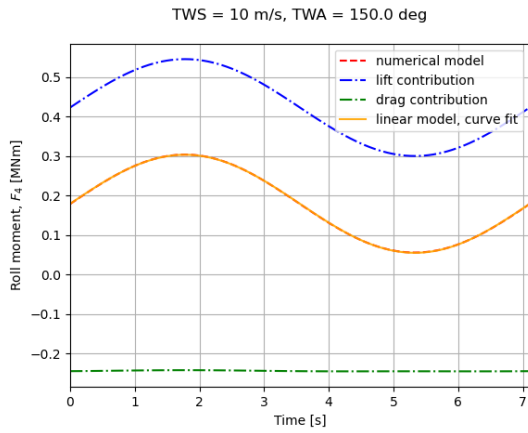


(q) Case 5: Roll induced roll moment

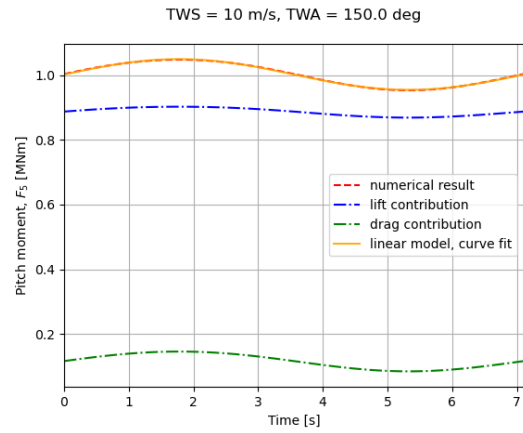


(r) Case 5: Roll induced pitch moment

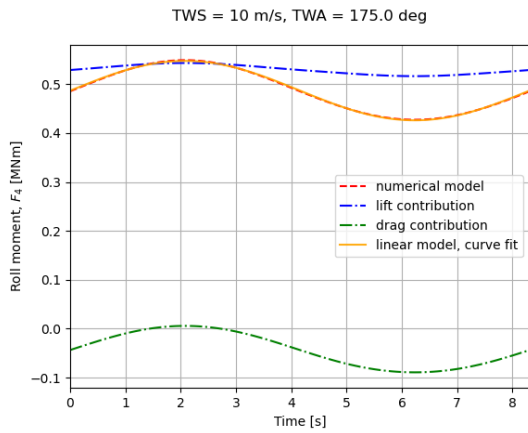
Figure C.1: Continued.



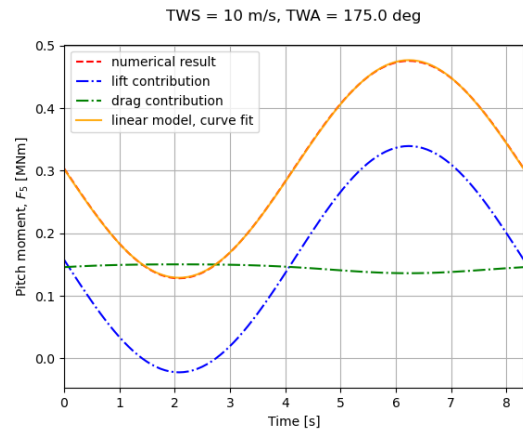
(s) Case 5: Pitch induced roll moment



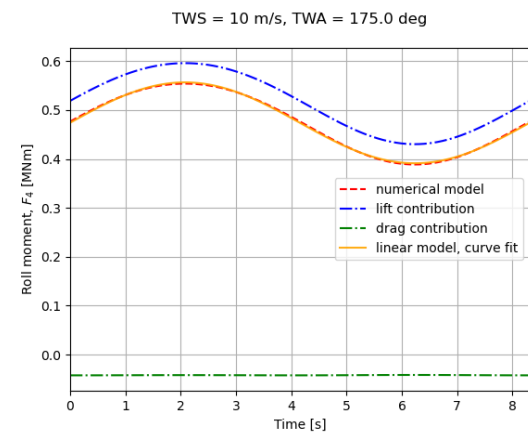
(t) Case 5: Pitch induced pitch moment



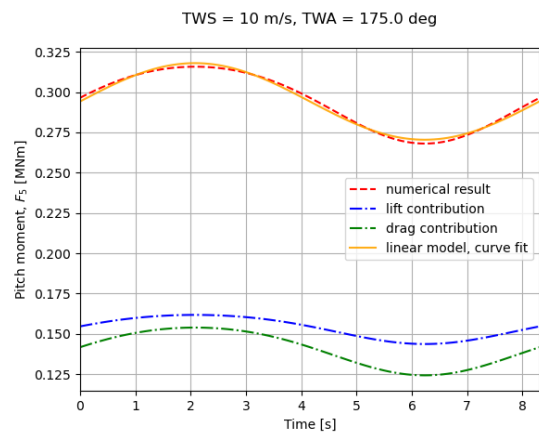
(u) Case 6: Roll induced roll moment



(v) Case 6: Roll induced pitch moment



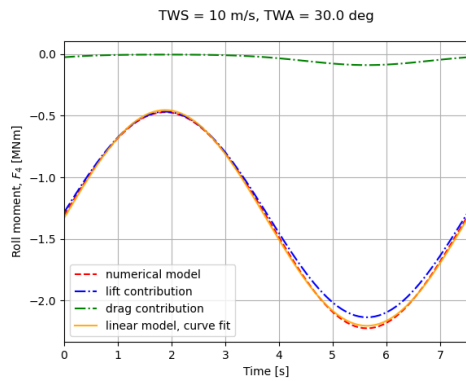
(w) Case 6: Pitch induced roll moment



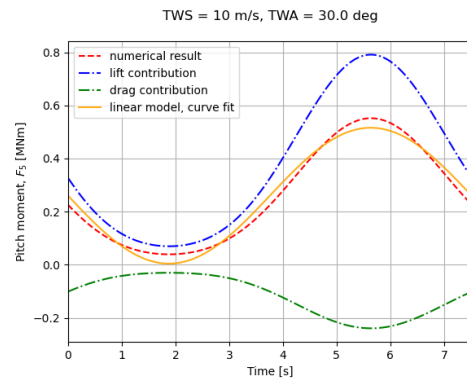
(x) Case 6: Pitch induced pitch moment

Figure C.1: Continued.

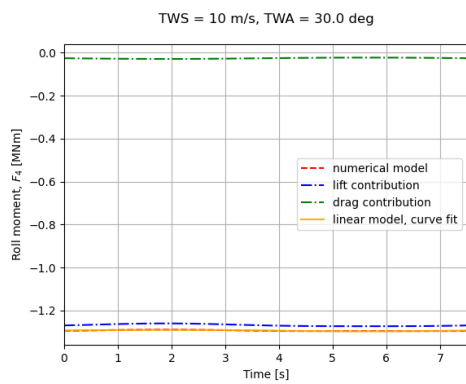
D Wingsail induced roll and pitch moments



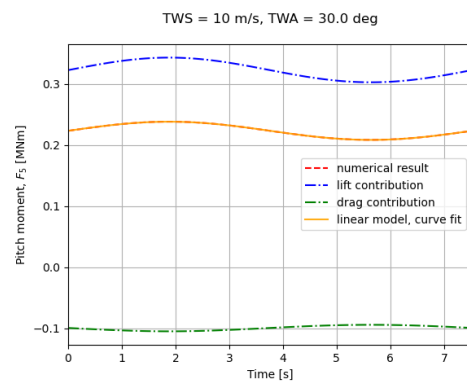
(a) Case 1: Roll induced roll moment



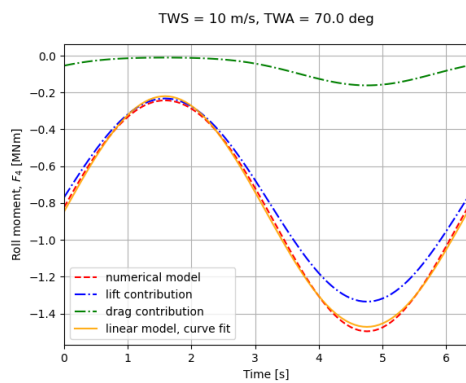
(b) Case 1: Roll induced pitch moment



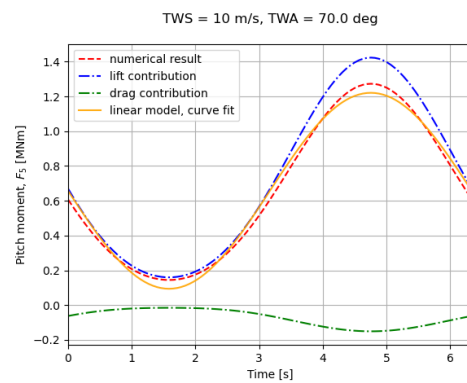
(c) Case 1: Pitch induced roll moment



(d) Case 1: Pitch induced pitch moment

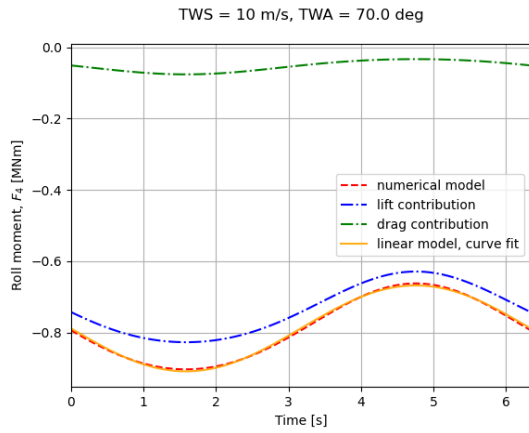


(e) Case 2: Roll induced roll moment

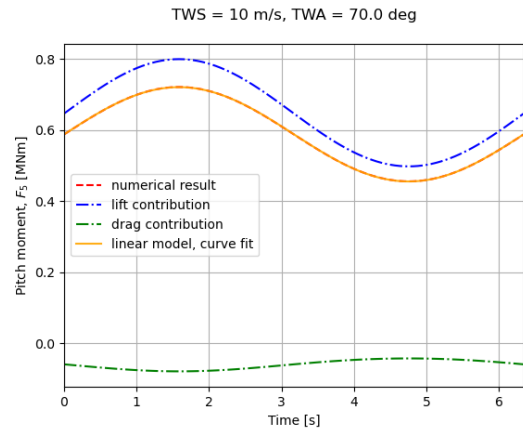


(f) Case 2: Roll induced pitch moment

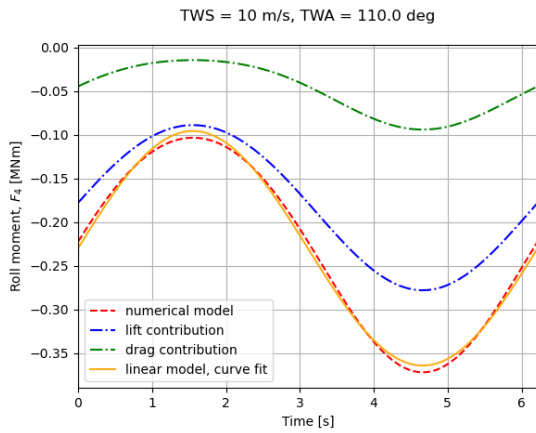
Figure D.1: Wingsail damping mechanism evaluation: induced aerodynamic moments



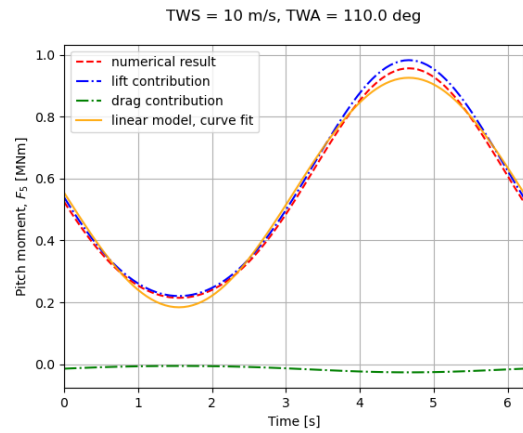
(g) Case 2: Pitch induced roll moment



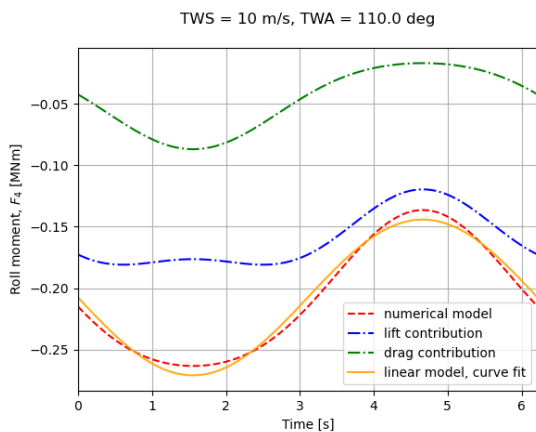
(h) Case 2: Pitch induced pitch moment



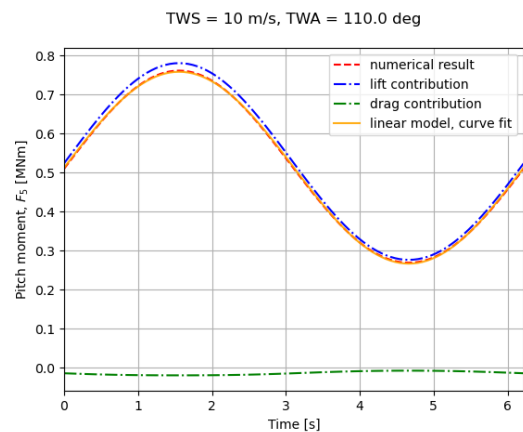
(i) Case 3: Roll induced roll moment



(j) Case 3: Roll induced pitch moment

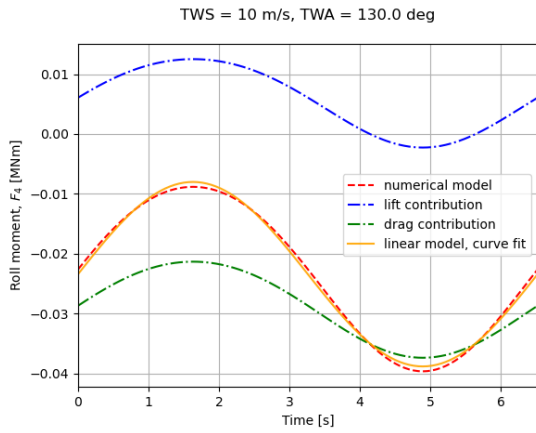


(k) Case 3: Pitch induced roll moment

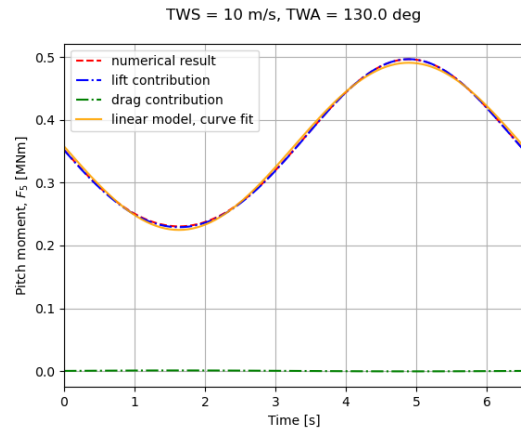


(l) Case 3: Pitch induced pitch moment

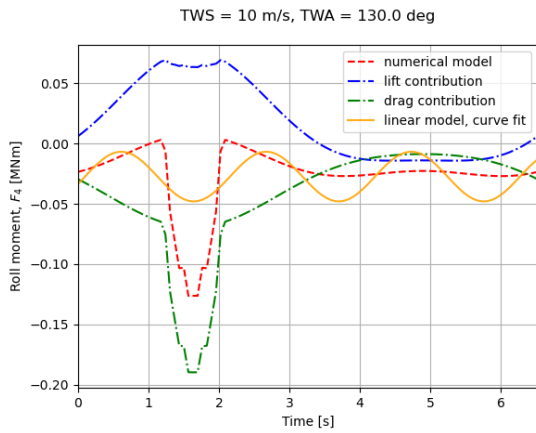
Figure D.1: Continued.



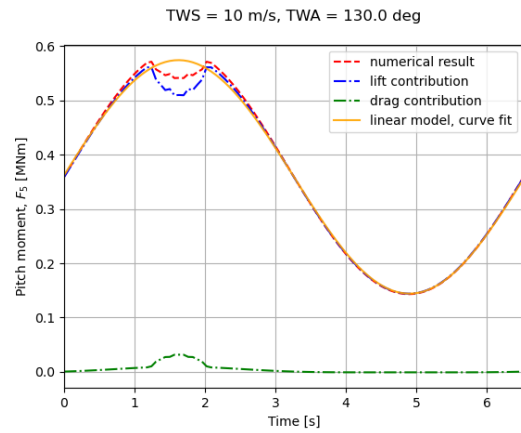
(m) Case 4: Roll induced roll moment



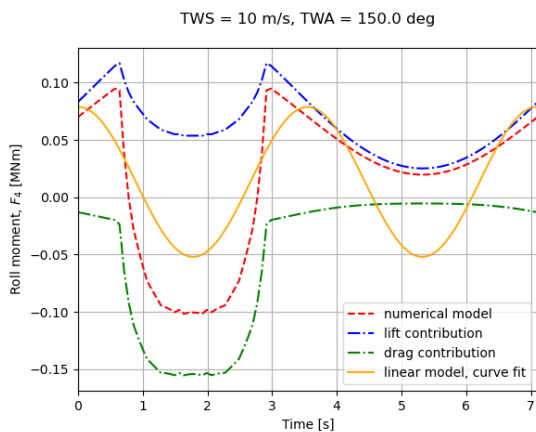
(n) Case 4: Roll induced pitch moment



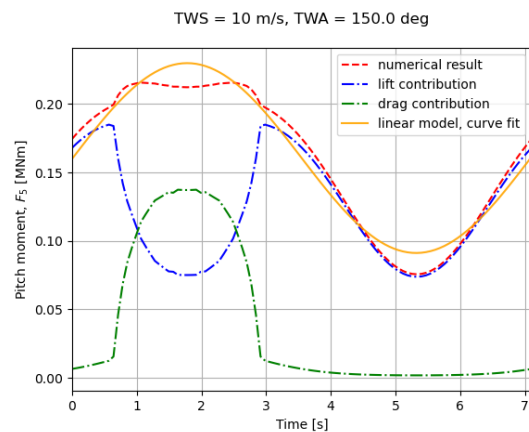
(o) Case 4: Pitch induced roll moment



(p) Case 4: Pitch induced pitch moment

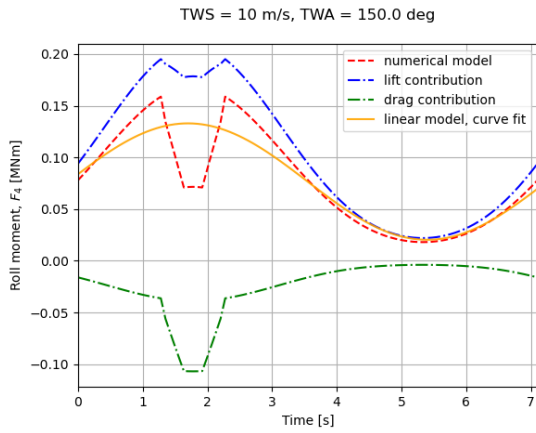


(q) Case 5: Roll induced roll moment

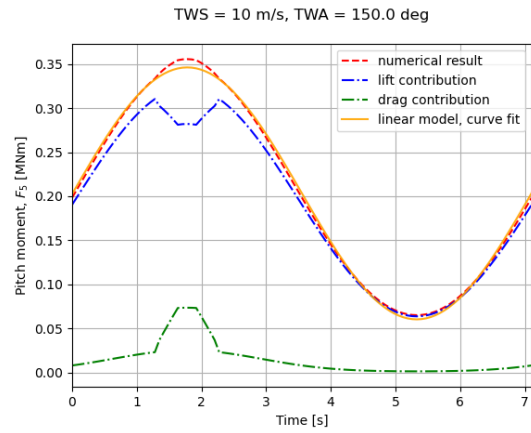


(r) Case 5: Roll induced pitch moment

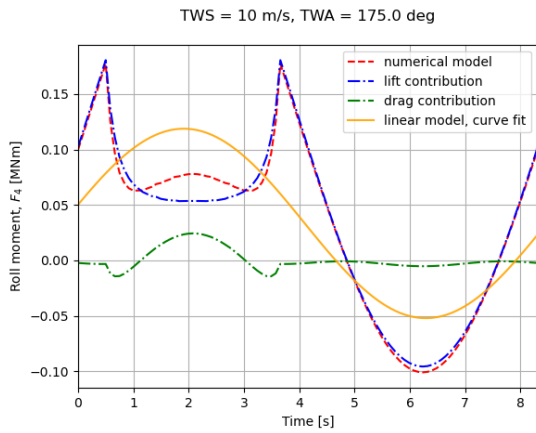
Figure D.1: Continued.



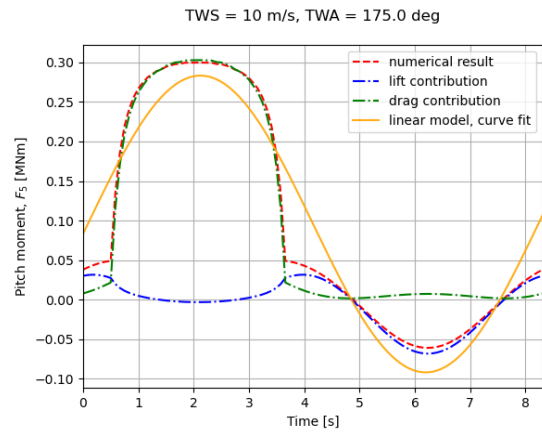
(s) Case 5: Pitch induced roll moment



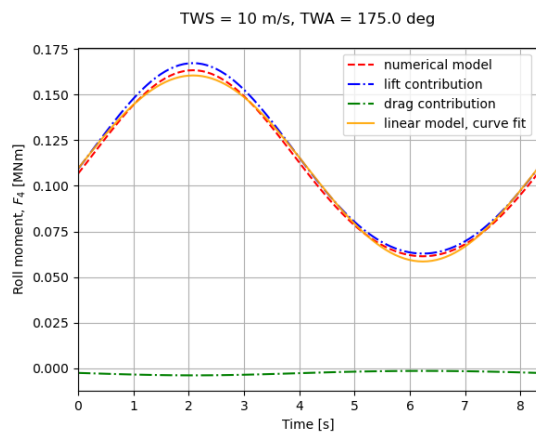
(t) Case 5: Pitch induced pitch moment



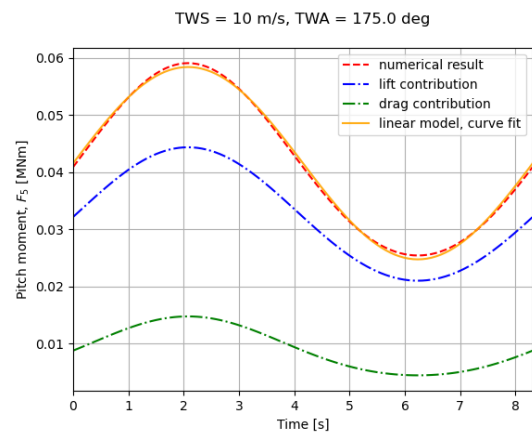
(u) Case 6: Roll induced roll moment



(v) Case 6: Roll induced pitch moment



(w) Case 6: Pitch induced roll moment



(x) Case 6: Pitch induced pitch moment

Figure D.1: Continued.

